University of Milano-Bicocca

Department of Material Science

Investigation of Alkaline Ion Rocking Chair Batteries

Doctoral dissertation in Materials Science (XVII cycle) of

Reza Fathi

Supervisor : Prof. Riccardo Ruffo

Dean of the doctorate : Prof. Gian Paolo Brivio

March 19, 2015 – Milan

I dedicate this thesis to my mother who has always encouraged and supported me during my studies.

Acknowledgments

I would like to thank my advisor Dr.Riccardo Ruffo for guidance and very interesting discussions we have had during my doctorate study. I am very grateful for doing my PhD under his supervision. Thanks also go to Dr.Claudio Maria Mari and Matteo Salamone for their assistance during my time in Italy.

I also would like to thank Dr.Jeff Dahn for hosting me in his Lab at Dalhousie University for more than one year and giving me access to state of the art research facilities. I am very grateful for this opportunity.

I am thankful to my family and friends who have been always beside me.

Contents

CHAPTER 1

General introduction : Li-ion batteries

1.1 History of Li-ion batteries

Lithium is most electropositive (-3.04 v.s. standard hydrogen electrode) and also lightest metal (M_{Li} = 6.94 g/mol). This fact makes it very interesting for designing electrochemical storage system with high energy density. In early 1970's Whittingham from EXXON [1], proposed Li/TiS_2 battery which showed a high energy density around 480 Wh/kg. This result was really promising since it was comparable to energy density of Na/S and high temperature LiAl/FeS, since they showed energy density of 330 and 460 Wh/kg. Later on it turned out that this system is not viable because of dendritic growth of Li metal after plating on the surface of anode. The issues related to the safety of lithium metal batteries forced researchers to pursue several other approached in modifying positive and negative electrodes. Researchers from Bell Labs achieved significant advances in using the oxides as they showed high capacity and voltage. In the meantime the importance of carbonaceous materials has been understood and researchers proposed graphite as a intercalating anode with relatively high capacity and low voltage with respect to Li/Li^+ which can deliver a high energy density. Finally in 1991 the SONY Corporation commercialized first lithium ion battery comprised of LiCoO2 and Carbon as cathode and anode [2]. Since lithium exists in non-metallic state in these batteries, even after charge /discharge cycles, they showed high safety when unwanted crushing or penetration happening in them. The energy density for those batteries was around 110 Wh/kg which was really promising for portable devices, having in mind their high safety.

1.2 The lithium ion battery

Simply defined, a battery is a electrochemical power source that convert chemical energy to electrical energy. The reaction produces current at certain time and voltage. Primary batteries or cells are not rechargeable and electrochemical reaction associate with these cells are irreversible. These batteries can be used only once, which means after the discharge process the battery become unusable. In the case of rechargeable (secondary batteries) the electrochemical reaction is reversible and the battery can be used several times, which makes them more interesting than primary cells. Examples of secondary batteries are lead-acid batteries, nickel-cadmium batteries, and lithium ion batteries. Lithium ion battery comprises of two lithium insertion electrodes with electrolyte in between that allows lithium ions to transfer between the electrodes. Two electrodes are separated with a permeable membrane which allows ion transportation between the

electrolyte while keeping two electrodes apart to prevent electrical short circuit. Of course an external circuit is needed in order to balance the electrochemical reaction via transporting electrons from one electrode to another. Figure 1.1 shows the different component of lithium ion battery [3].

The negative electrode of the lithium ion battery is usually graphite which can reversibly intercalate one lithium atom per six carbon as :

$$Li_xC_6 <=> xLi^+ + xe + 6C \quad (1.1)$$

Usually, 1 one lithium ion is intercalated for each aromatic ring, this correspond to 372 mAh/g of theoretical capacity which is almost 10% of the theoretical capacity when Li metal is used as anode (3800 mAh/g). Losing this much capacity when replacing lithium metal with graphite one can gain much more stability and higher life time.

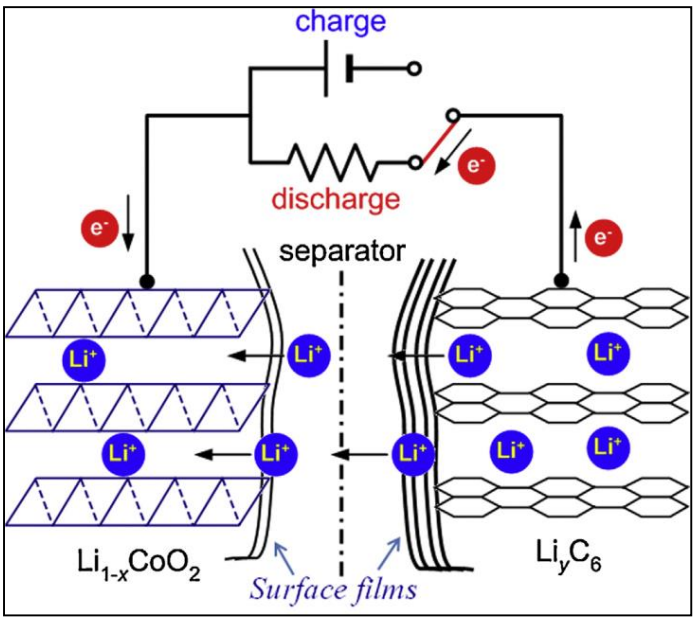

Figure 1.1. Schematic illustration of different components of a lithium ion battery [3].

The positive electrode is usually a transition metal oxide which Li ions can reversibly intercalate in the structure. The cathode is actually the sink for the lithium ions when electrodes are externally connected via a charge transfer circuit. Among the positive electrodes, $LiCoO_2$ (LCO) is the first commercial and most common cathode technology that manufactures use in their lithium ion batteries with a layered structure and practical capacity of 150 mAh/g. This structure and also other kinds of positive electrodes will be discussed later in this thesis. The electrochemical reaction for LCO is:

$Li_{1-x}CoO_2+xLi^+ + xe <=> LiCoO_2$ (1.2)

The electrodes active mass is combined with an additional conductive additive (usually carbon black which is highly conductive) and a polymeric binder that maintain the whole composite together and also provide the adhesion between the loaded material and the current collector. Current collector for the anode side is usually copper, and for the cathode is aluminum which do not react with lithium at low and high potential versus Li/Li^+, respectively.

The most typical electrolyte solutions for Li-ion batteries consist of $LiPF_6$ as the most suitable salt dissolved in alkyl carbonates including ethylene carbonate (EC) and another solvent like ethyl methyl carbonate (EMC). The electrolyte is unstable in the intercalation potentials of Li a very low potential, and the reduction of many parts of electrolyte on the surface of graphite form an insoluble film called solid electrolyte inter-phase (SEI) layer (mentioned as surface film in Figure 1). Stability of SEI is crucial for the longer life time of lithium ion battery.

1.3 Motivation and challenges

Lithium ion batteries have been widely used to power many portable electronic devices like cell phones. In fact, lithium ion batteries are currently being developed to power an increasingly diverse range of application.

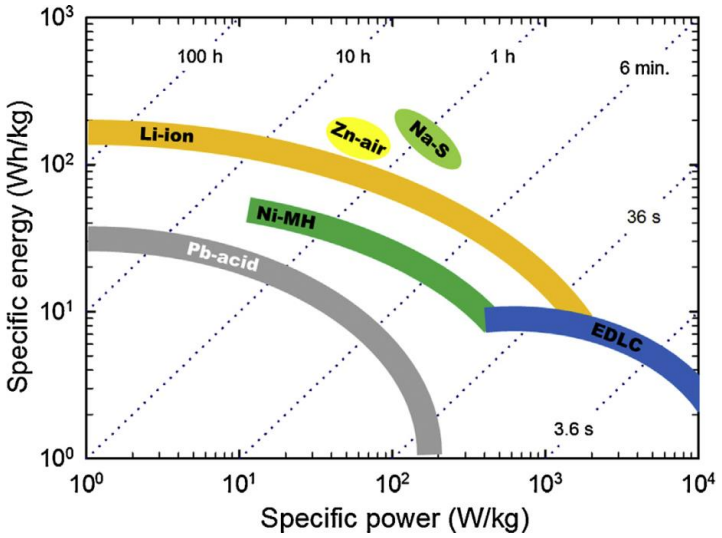

Figure 1.2. Energy versus power density for different power sources (Ragone chart) [3].

As shown in Ragone chart, Figure 1.2, providing high energy and power density, Li-ion batteries are regarded as the battery of choice for future and emerging technologies like green cars and smart grids. Since most of vehicles around the world are powered by combustion engines, there is a real concern in terms of petroleum shortage/cost, and environmental problems, and the fossil fuel needs to be replaced by a green technology. Lithium-ion batteries are considered as the best technology to replace the old petroleum related technologies in vehicles and several companies have already launched production of electric vehicles using lithium ion batteries. In fact, lithium-ion battery is the only viable technology for ground transportation unless major improvement happens in the other power source technologies like fuel cells. However, we still have long way to go in order to increase the energy density and decreasing the cost of lithium ion batteries. High specific energy can be achieved by utilizing electrode materials that have a higher specific capacity than current commercial electrode materials, and materials should be in low price and also environmentally friendly. As shown in figure 3, one of promising anode materials is silicon which has huge theoretical capacity and it is also very cheap. The other component that has huge impact on performance of Li-ion batteries is the electrolyte. Because electrolyte interacts closely with both anode and cathode electrodes, it is very important to improve its stability at a wider range of voltage in order to achieve higher energy density.

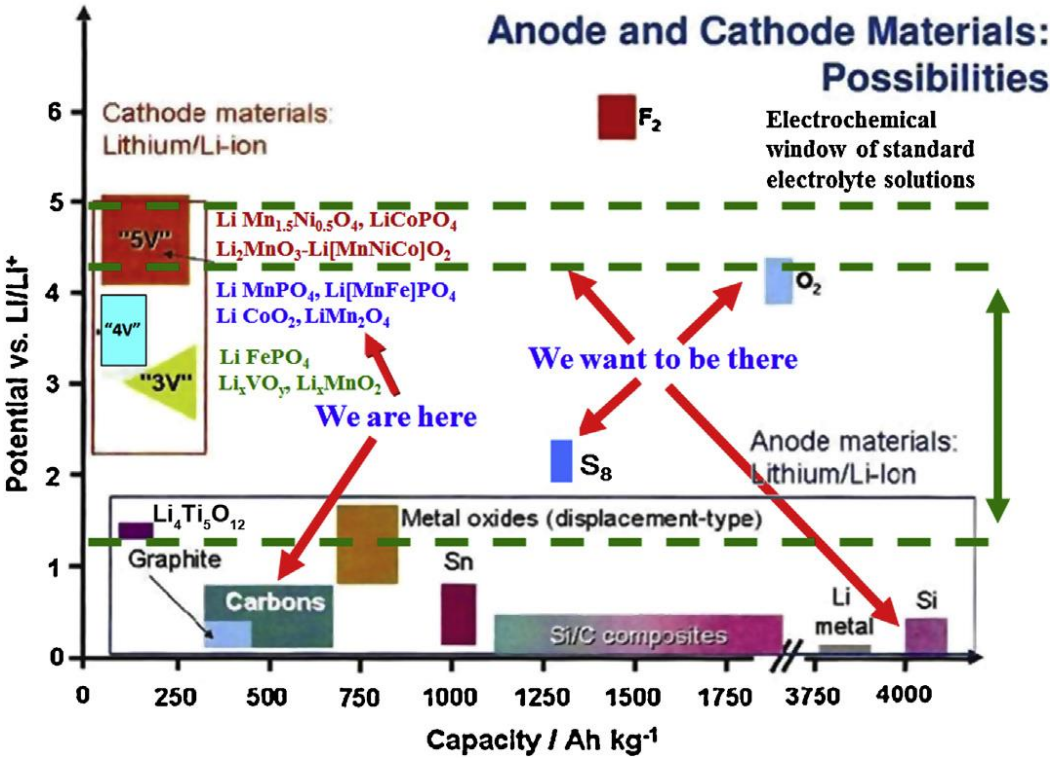

Figure 1.3. A schematic representation of Li-ion battery research roadmap [3].

Figure 1.3 shows road map for researcher in Li-ion batteries. The electrochemical window of standard electrolyte shows that in order to high voltage cathode materials to be practical we need electrolyte solutions that are stable at higher voltages. This could be achieved by presenting new types of electrolytes or electrolyte additives.

1.4 Negative electrode materials in Li-ion batteries

The negative electrode is the source of Li-ions during the discharge process in Li-ion batteries, and basically can be any type of material that could host Li-ions by electrochemical reaction at a very low voltage versus Li/Li^+. The mechanism of electrochemical reaction is different in different anode materials, Therefore they store different amount of energy per unit mass [capacity (mAh/g)] at different voltages.

1.4.1 Intercalation – The case of graphite and Li4Ti5O12

Graphite nowadays is the choice of material for the negative electrode in Li-ion batteries. Graphite can intercalate up to one Li atom per six carbon atom at room temperature. During this electrochemical reaction Li atoms insert between graphene layers without changing the crystalline structure of graphite. Figure 1.4 shows insertion model of Li atom between the graphite sheets.

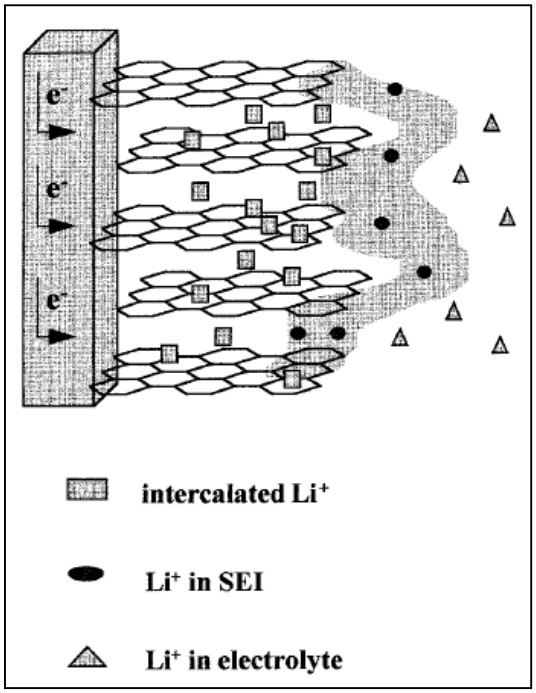

Figure 1.4. Lithium intercalation model in graphite structure including SEI layer [4].

The practical capacity of lithiated graphite (LiC_6) is around 330 mAh/g. Such reversible capacity is reached after the first cycles of the battery, when loss of active lithium takes place as result of its irreversible consumption (SEI formation process) mainly on the negative electrode giving rise to an irreversible capacity (Q_{irr}). The lost of lithium cannot be anymore restored during the following cycles, however the formed film is stable and prevents further electrolyte reductions during the following cycles. As a matter of fact, during the first battery charge, the active Li-ions is released from the positive electrode, crosses the electrolyte and is reduced on the surface of the carbon negative electrode. Freshly deposited lithium will react with the electrolyte and the electrode binder and tends to form a passivating layer especially when ethylene carbonate (EC) is used as one of the electrolyte solvents. The passivating layer, as mentioned before, generally addressed to as the solid electrolyte interface (SEI).

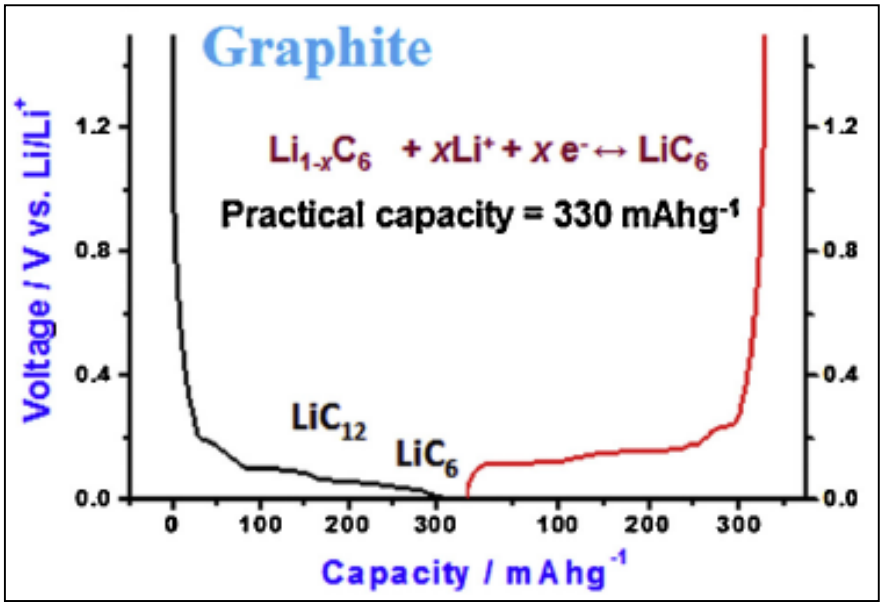

Figure 1.5. Voltage profile of electrochemical reaction of Li with graphite. Black plot shows insertion and red plot shows the extraction of Li [3].

Figure 1.5 shows the voltage profile of electrochemical reaction of lithium with graphite. Some safety concerns have been risen during the early years of development and commercialization of this battery regarding the use of graphite, because of its very low working voltage, close to that of metallic lithium, which would lead to lithium plating during the battery charge, specially at lower temperatures (or high currents) when the diffusion coefficient of Li atoms into the graphite is much more lower. This might be one of the reasons why hard or nongraphitized soft carbons were first used by SONY and other battery developers, since these carbons will store and release lithium at higher voltages. However, graphite (synthetic or natural) shows larger specific and volumetric practical capacities together with a high cycle life (over 1000 cycles at 100% DOD). In addition, the kinetics of lithium exchange with the electrolyte (charge transfer) and diffusion within the carbon layered structure are faster than in most other carbonaceous materials, allowing the battery to be 100% charged in a short time as 1 hour. The safety issue in connection with Li intercalation into the graphite was also addressed to by a more appropriate selection of the electrode binder, which in the case of PVDF is known to enter a surface reaction with the active lithium stored on the surface or into graphite [5].

$Li_4Ti_5O_{12}$ (LTO) is the another anode candidate with intercalating reaction mechanism. LTO has good reversibility and has no structural change in the charge discharge process.

It offers a stable operating voltage of approximately 1.5 V vs. lithium, which if couple with high voltage cathode would deliver an appropriate cell voltage for different applications. Figure 1.6, shows the voltage profile of LTO along with its rate capability.

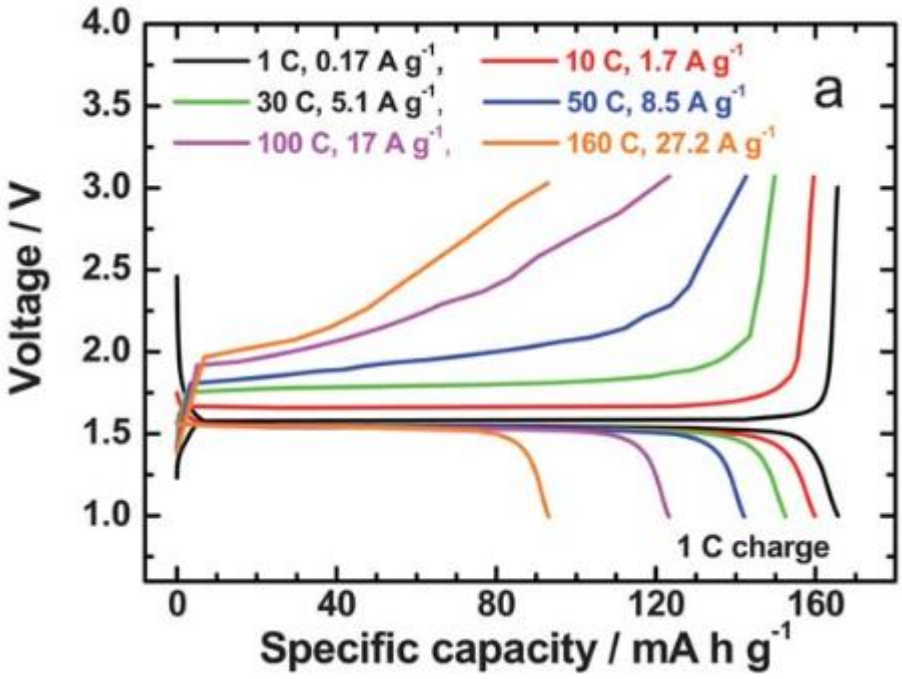

Figure 1.6. Voltage profile of LTO, shown at different rates indicated in the figure [6].

One should keep in mind that LTO is electronically insulator and needs to be mixed with appropriate amount of conductive materials like carbon black in order to allow charge transfer and balance the following reaction :

$$_{X}Li + xe + Li_4Ti_5O_{12} = Li_{x+4}Ti_5O_{12} \quad (1.3)$$

The main advantage of LTO is that its working potential range lies in the electrolyte stability windows and it does not require the formation of a stable SEI layer with the consumption of irreversible capacity. Moreover, it can be used at higher current rate respect traditional graphite systems meeting very high power requirements.

1.4.2 Alloying – The case of silicon

Demands for higher volumetric (Wh/l) and gravimetric (Wh/Kg) energy density in Li-ion batteries, forced researchers to look for electrode materials other than graphite/$LiCoO_2$ as anode/cathode in lithium ion cells. Small improvements have been achieved in cathode materials, but not as much as it could meet the industrial requirements in terms of

increasing the cell capacity (positive electrode materials will be discussed in detail later in this thesis). Since finding new cathode materials with significantly higher capacity has been a real issue, higher performance of lithium ion cell requires anode materials with higher specific capacity than those of graphite and other forms of carbon. Of course this higher capacity corresponding to reaction with lithium has to be at relatively low voltage with respect to metallic lithium in order to achieve a full lithium ion cell with large energy density. It has been shown that lithium can react with number of metals at room temperature, including Sn, Pb, Zn, Cd, Ag, Pt, and Au. Figure 1.7, shows the specific capacity of these elements. According to figure 1.7, Si seems to be promising because of its huge capacity with respect to the other metals.

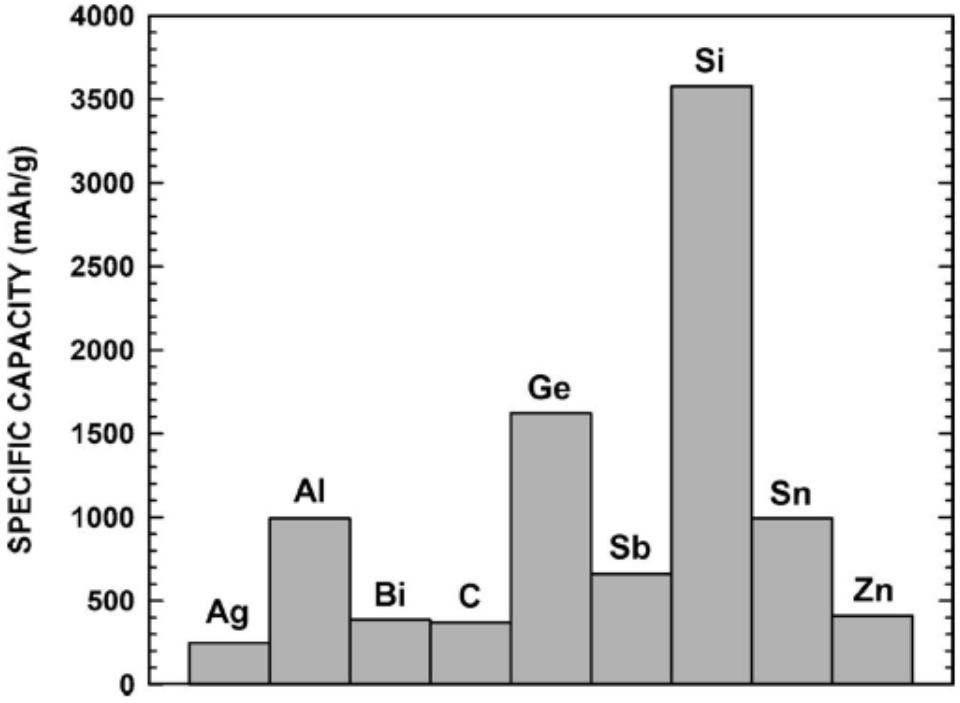

Figure 1.7. The specific capacity of numbers of element electrochemically active with Li [7].

In addition, being the second most abundant element in the earth crust, silicon is a very good candidate as anode in lithium ion cells. Study of Li-Si binary system shows that Si can accommodate 4.4 lithium atoms leading to formation of $Li_{22}Si_5$ alloy. It was reported that alloying process of silicon anodes results formation of $Li_{12}Si_7$, $Li1_4Si_6$, $Li1_3Si_4$, and $Li_{22}Si_5$. However, As figure 1.8 shows, a bulk silicon showed a charge capacity of above

3250 mAh/g and discharge capacity of less than1200 mAh/g, corresponding the columbic efficiency of only ~ 35% .

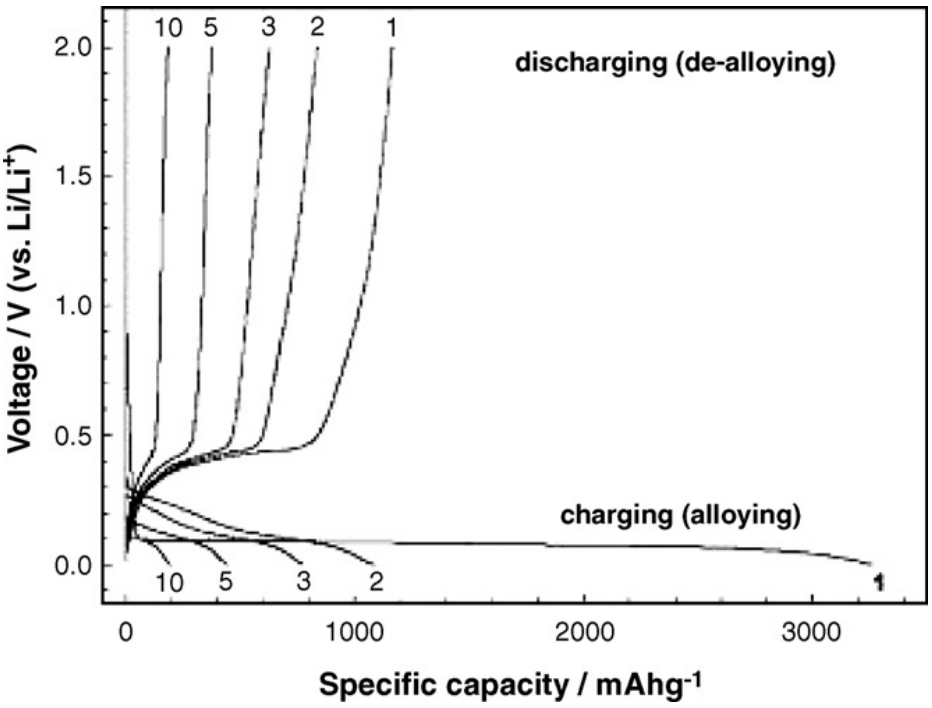

Figure 1.8. Galvanostatic charge-discharge voltage profile of silicon anode [8].

In fact, this is the result of huge expansion of silicon electrode during lithium insertion. Silicon expands volumetrically by up to 400% on full lithiation, and it can contract significantly on lithium extraction (delithiation). The huge expansion of silicon creates two critical challenges: minimizing the degradation of the mechanical integrity of the silicon electrodes and maintaining the stability of the SEI, which lead to very low columbic efficiency.

Stress induced by large changes in the volume of silicon anodes causes cracking and pulverization, and this is considered to be the main reason for their rapid capacity loss. Some studies suggested that the tendency for fracture and decrepitation could be reduced or avoided by reducing the material size to the nanometric range. Indeed, the strain in such silicon nanostructures can be relaxed easily, without mechanical fracture, because of their small size and the available surrounding free space. Figure 1.9 shows the improvement in the capacity retention of silicon anode achieved by nanotechnology (hollow nano-spheres of silicon) .

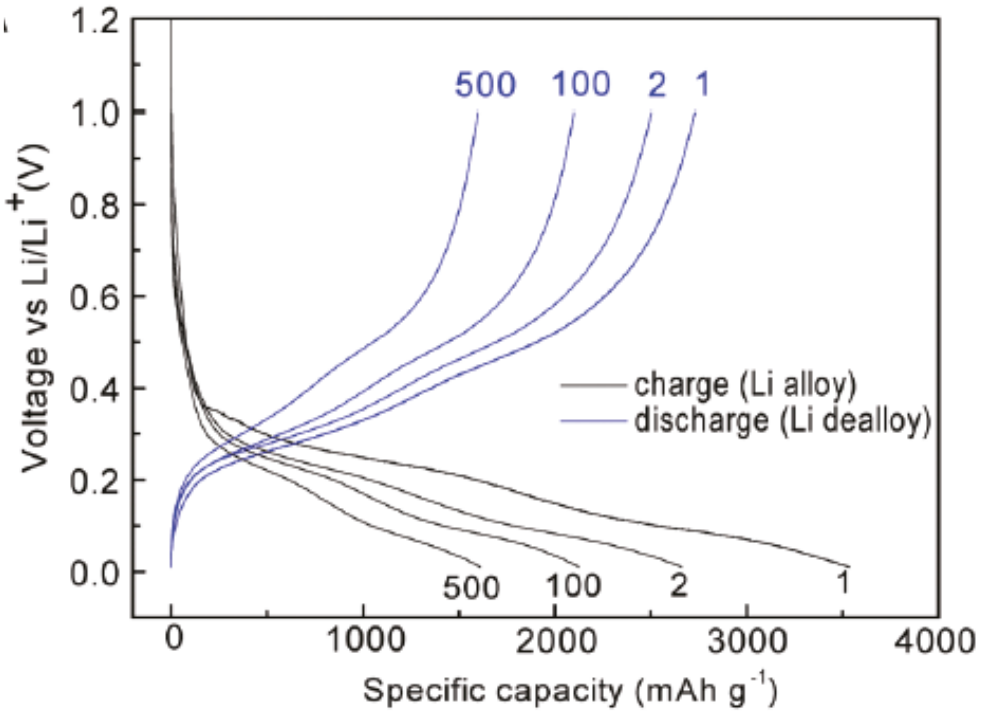

Figure 1.9. Electrochemical performance of Si hollow nanosphere versus Li/Li^+ for the different cycle numbers [9].

Figure 1.10 shows the SEM image of fabricated hollow nano-sphere silicon with a diameter of about 400 nm. It appears that this structure can tolerate huge volume expansion of silicon particle during lithiation. However, producing such structure is expensive and might not meet the industrial needs.

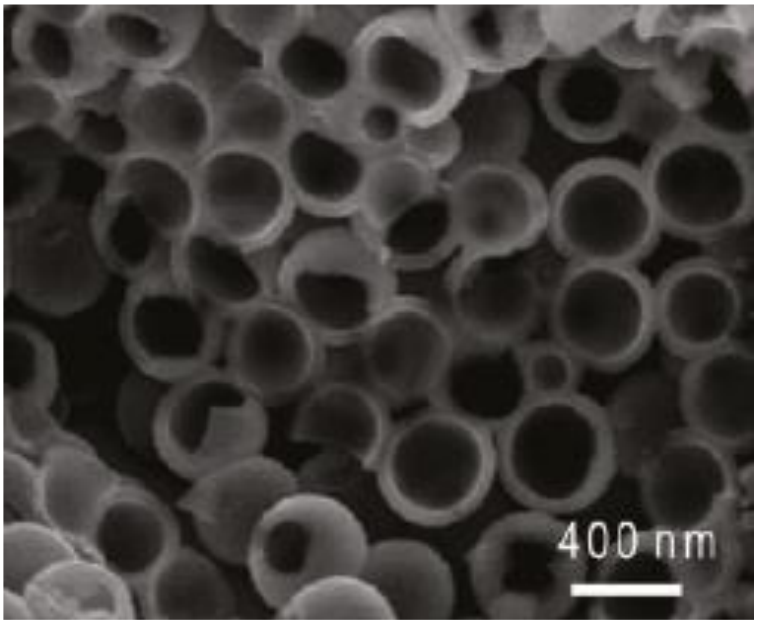

Figure 1.10. SEM image of nano-sphere silicon anode [9].

However, SEI stability at the interface between the silicon particles and electrolyte is still problematic in achieving a long life battery. Electrolyte decomposition occurs due to the low potential of anode and creates the passive layer of SEI. The SEI layer created during lithiation on the surface of expanded silicon particles, can be broken when particles shrink during delithiation. This exposes new and fresh silicon surface to the electrolyte and SEI forms again. The damage to the SEI layer causes degradation of lithium ion battery since active lithium ions have to be consumed in SEI layer formation, repairing or growth. This process has been shown in figure 1.11 schematically.

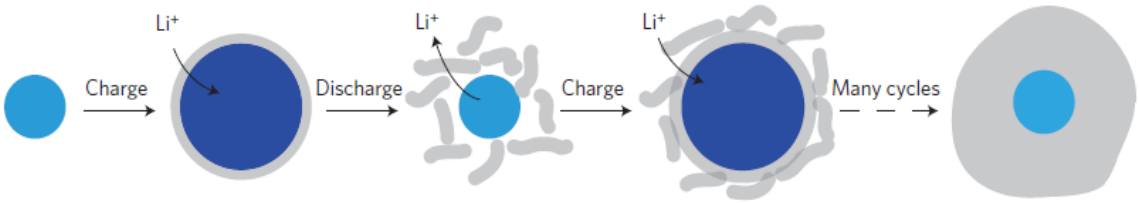

Figure 1.11. Schematic illustration of SEI formation on the silicon surface [10].

The other important issue related to the nanostructure materials is the expensive preparation methods of these structures. Ball milling seems to be one of the methods that overcomes this issue and offers materials with a relatively cheap manufacture.

1.4.3 Other carbonaceous materials

Lithium can be inserted reversibly in most carbonaceous materials. There are many carbon types including natural and synthetic graphite, carbon blacks, hard carbons, carbon fiber, coke, and other carbonaceous materials produced by pyrolysis of organic precursor in inert gas. But not all of them reversibly react with lithium in an appropriate voltage, and it is important to understand which one can accommodate the largest amount of lithium per unit mass in order to achieve high energy density. Generally speaking, carbon systems reacting with lithium in reversible way can be divided in three groups as Dahn et al suggested: 1- Graphitic carbons 2- Hydrogen containing carbon 3- Hard carbons. Later in this thesis another type of carbon will be presented, which has been explored by the author and does not fit any of these groups. This type of carbon shows a promising electrochemical behavior and will be discussed separately. Graphite has huge impact on lithium ion battery technology and has been discussed before in this thesis, therefore two other type of carbonaceous materials will be presented hereafter.

Hydrogen containing carbons

Even though they show huge reversible capacity of 900 mAh/g, these materials show big hysteresis in their voltage plateau and therefore are not practically useful for lithium ion batteries. Most of carbon materials pyrolized at temperature near to 700 °C show this behavior in their reaction with lithium. These materials contain substantial amount of hydrogen with a hydrogen/carbon ratio as high as 0.2. So hydrogen seems to play a crucial role in determining the electrochemical properties. In fact, as shown in Figure 1.12, materials with lesser amount of hydrogen show much more less reversible capacity compared to those contain higher amount of hydrogen.

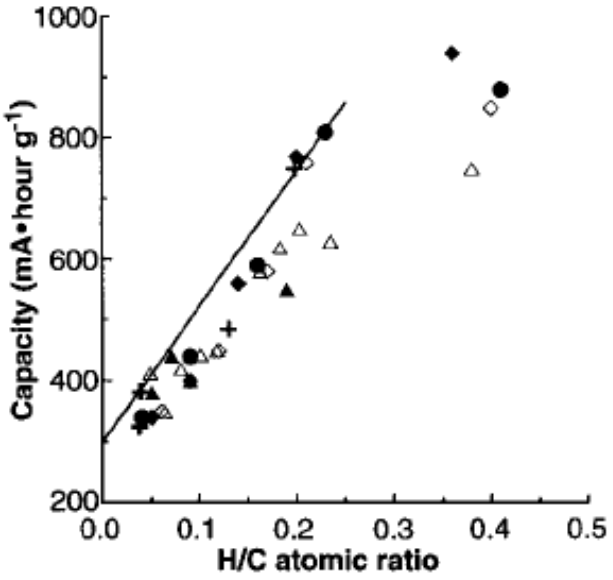

Figure 1.12. Reversible capacity of carbonaceous materials as function of hydrogen content [11].

In addition, hydrogen containing materials show a poor cyclability and the their capacity drops after 10-15 cycles or so. It appears that charge transfer between H and Li is happening in these materials therefore lithium atoms can bond with hydrogen atoms. This would change the C-H bond, and it causes change in relative atomic position of C and H. This is the main reason of hysteresis in their voltage plateau, as bond changing appears to impact voltage profile in such way. Figure 1.13 shows voltage profile of Graphite, hard carbon and hydrogen containing carbon at different stages to clarify the difference between their electrochemical behavior.

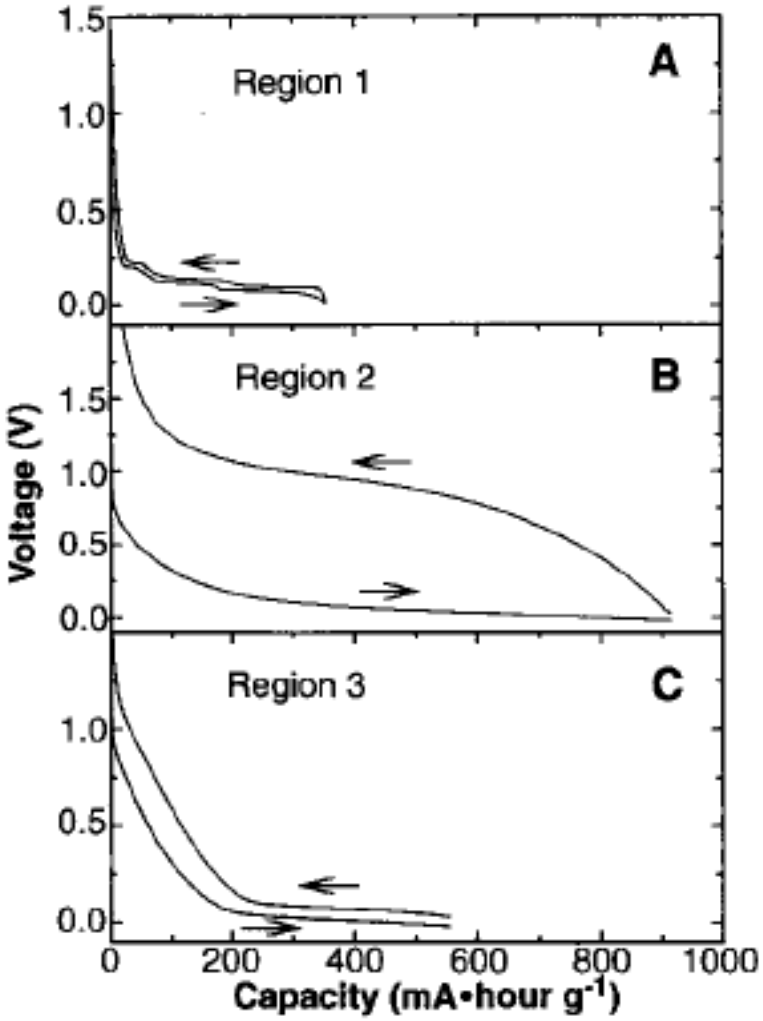

Figure 1.13. Voltage profile of a) graphite b) petroleum pitch heated to 550 ºC and c) Hard carbon [11].

Hard Carbons

Hard carbons show two plateau in their voltage profile as shown in Figure 1.13.c the low voltage plateau shows represents the intercalation of lithium atoms inside the nano and micro pores of this material. This mechanism of intercalation requires a weak lithium/carbon bond, and therefore a low voltage plateau (strong lithium/lithium interaction). This is consistent with low voltage plateau showed in Figure 1.7.c, which is several tens of millivolts above voltage of lithium itself. This also requires a small hysteresis in the voltage plateau (charge and discharge) since lithium atoms are weakly bonded and it would de-intercalate easier, as it is confirmed nicely in figure 1.13.c .

The higher voltage plateau appear to be related to adsorption of lithium on the surface of small portion of grapheme sheets in the structure. Figure 1.14 shows the house of card model for hard carbon proposed by Dahn et al.

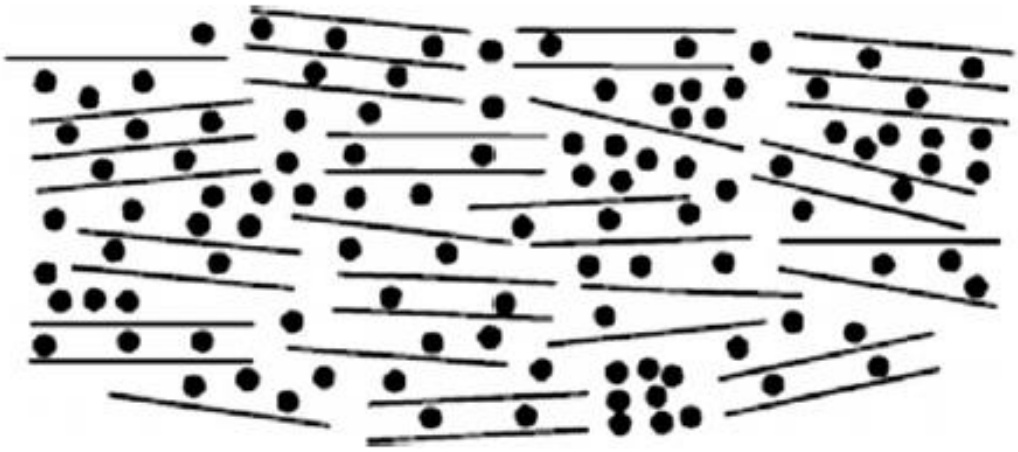

Figure 1.14. Scematic illustration of house of cards model for Li insertion in hard carbon [12].

In graphite, there is one layer of intercalated lithium for each carbon sheet, but any single carbon sheets in the "house of cards" structure of hard carbon can absorb two layers of Li on each side of the sheet, leading to a theoretical capacity of 760 mAh/g or Li_2C_6. This could vary depend on amount of impurity in the hard carbon. In fact as shows before in the hydrogen containing carbons, surface functional groups play crucial role in the electrochemical behavior of carbons. This can be clearly seen in figure 1.15, which shows the electrochemical properties of untouched hard carbon compared to materials ball milled in different atmospheres: both reversible and irreversible capacity increase with ball milling. The higher irreversible capacity is due to the higher surface area of ball milled hard carbon compared to untouched one, when more lithium atoms are consumed to form SEI on interface of electrode/electrolyte.

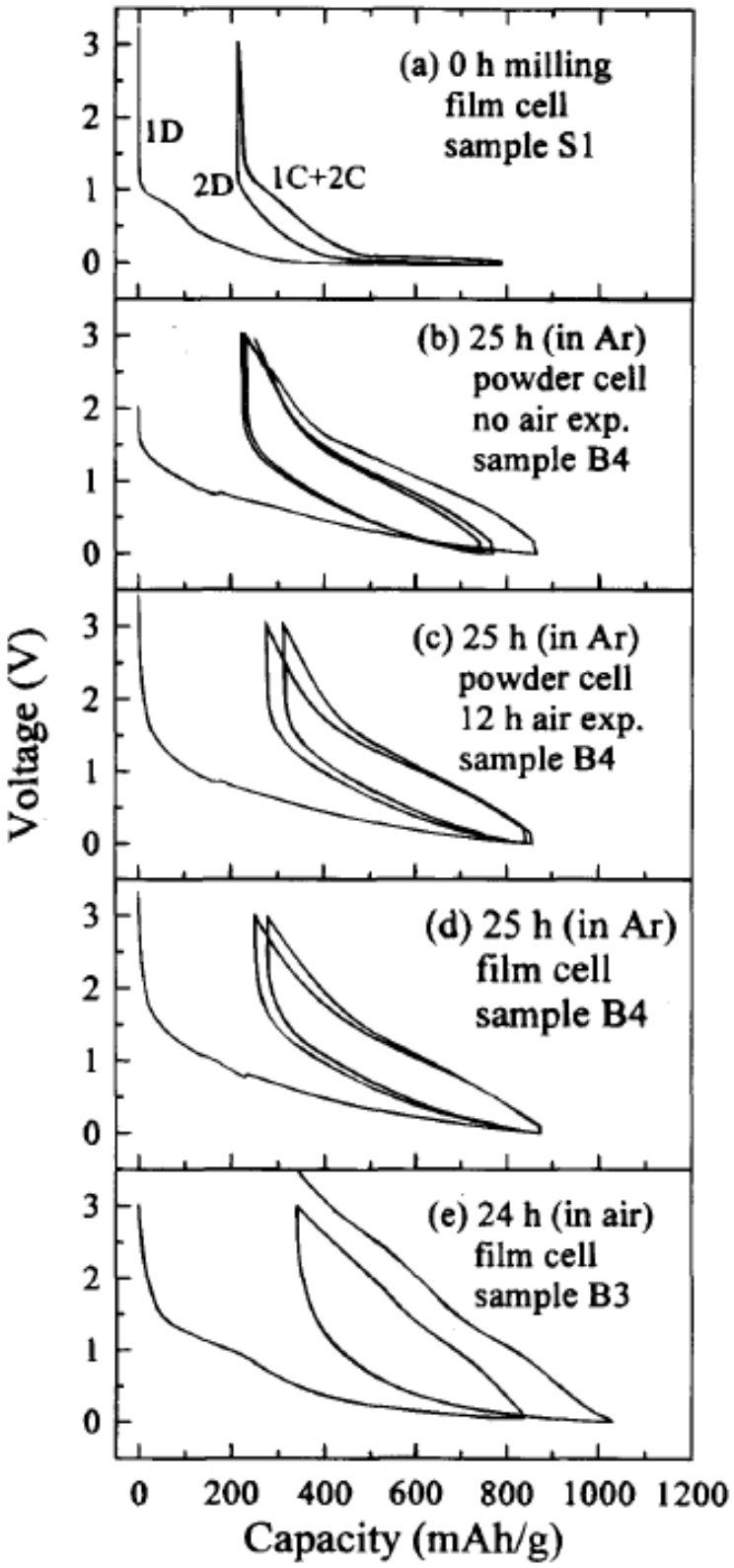

Figure 1.15. Electrochemical voltage profile of ball milled hard carbon. Ball mill variables are indicated in the figure [13].

Figure 1.15 clearly shows also the effect of surface functional groups. Generally speaking, these functional groups, which in this case absorb to the material during ball milling in the air or exposing to the air afterward, can cause hysteresis in the voltage capacity profile. This is reasonable because for instance oxygen is better electron acceptor than carbon so it is more difficult to remove a Li atom bonds to oxygen than carbon and this leads to hysteresis in their profiles. In the worst case scenario, figure 1.15.e , hard carbons were ball milled in the air atmosphere which accelerate adsorption of these functional groups on the surface of material, leading to larger capacity and hysteresis in their voltage profile.

1.5 Positive electrode materials in Lithium ion batteries

SONY commercialized Li-ion battery, in 1991, using $LiCoO_2$ (LCO) as positive electrode, which has layered structure. Li-ions can intercalate between the layers of LCO as showed in Figure 1.16.a.

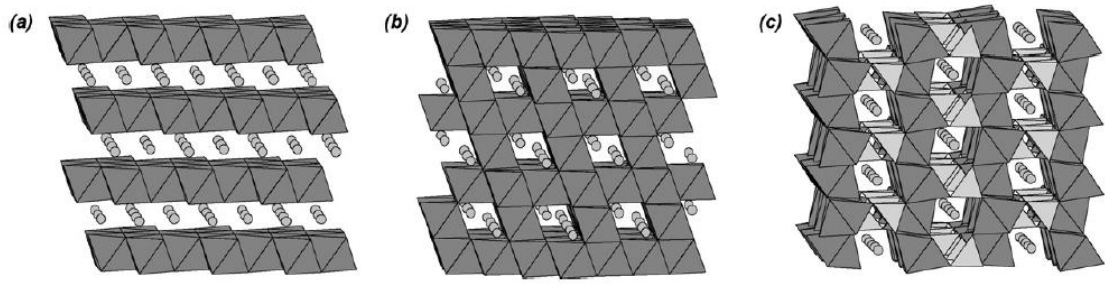

Figure 1.16. Schematic illustration of a) layered structure b) spinel structure and c) olivine structure [14].

The other insertion materials proposed as cathode in Li-ion batteries have framework structures shown in figure 1.16. Figure 1.16.b shows the spinel structure represented by $LiMn_2O_4$ (LMO) in which transition metal and lithium ions are located in octahedral sites in a close-packed oxygen array. Later on, in 1997, researchers proposed new class of insertion materials ($LiFePO_4$) with olivine structure shown in figure 1.16.c. However it shows a low operating voltage with respect to other positive materials which eventually

leads to a less energy density when coupled with graphite in a Li-ion cell. These structures will be discussed in detail.

1.5.1 Layered structure

Layered oxides with LMO_2 (M = CO, Mn, Ni) formula have been mostly used cathode materials in Li-ion batteries. LCO was studied earlier than other members of these family by Goodenough in 1976 and it is the most used active cathode material for commercial Li-ion batteries. Figure 1.17 shows the voltage profile of LCO when measured in a lithium ion half cell (half cell refers to a lithium ion cell with metallic lithium as anode).

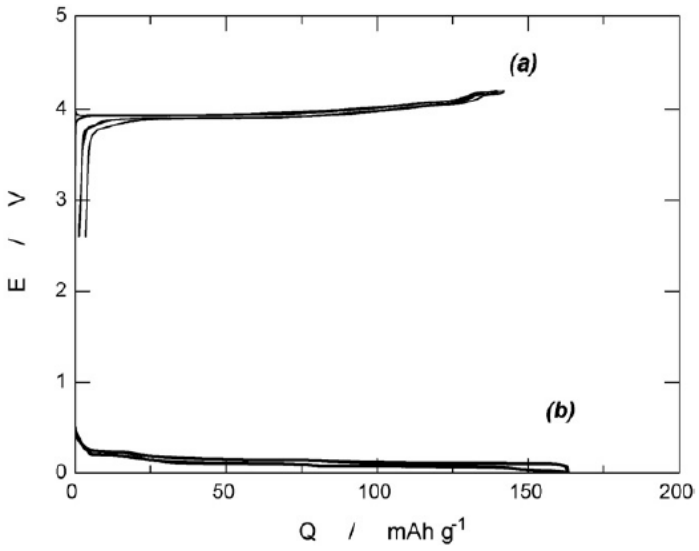

Figure 1.17. Charge and discharge voltage profile of a) LCO versus Li, and b) Graphite versus Li. Combination of these two gives a Li-ion battery. Specific capacity of graphite is given in 1/2 reduction [14].

As figure 1.17 shows, LCO has flat operating voltage at 3.9 V versus Li/Li^+. The crystallographic structures of LCO depend on synthesis temperature. At low temperatures (around 350 °C), a cubic spinel structure is formed that converts to a layered hexagonal at around 750 °C. Generally speaking, materials with layered lattice show better electrochemical performance compared to those with a cubic spinel lattice. The LCO phase is also called the O3 phase in the specific literature. The O3 phase represents the alkali metal ion, which is Li, residing in the octahedral interstitial sites with an

ABC…ABC… stacking arrangement of the layers. In the fully lithiated state, LCO remains in a layered structure having hexagonal unit cells. With removal of Li from the layered crystal lattice (during charging), nonstoichiometric $Li_{1-x}CoO_2$ compounds are formed and the oxidation of Co^{2+} to Co^{3+} takes place. Depending on lithium content in the structure, the crystallographic structure also changes. Most importantly, after 50 % of the lithium has been extracted from pristine LCO, the structural transformation from hexagonal to monoclinic phase is observed. This structural instability reduces the reversible electrochemical capacity (maximum achievable is 140 mAh/g) of LCO as compared to the theoretical value (280 mAh/g) and limits the amount of Li removed from the hexagonal lattice to 0.5. Due to this low practical capacity, toxicity and the relatively high cost of cobalt in LCO, a layered $LiNiO_2$ (LNO), which has basically the same structure of LCO, was proposed and experimented as a possible replacement. Figure 1.18 shows the electrochemical properties of LNO when measured in lithium ion half cell.

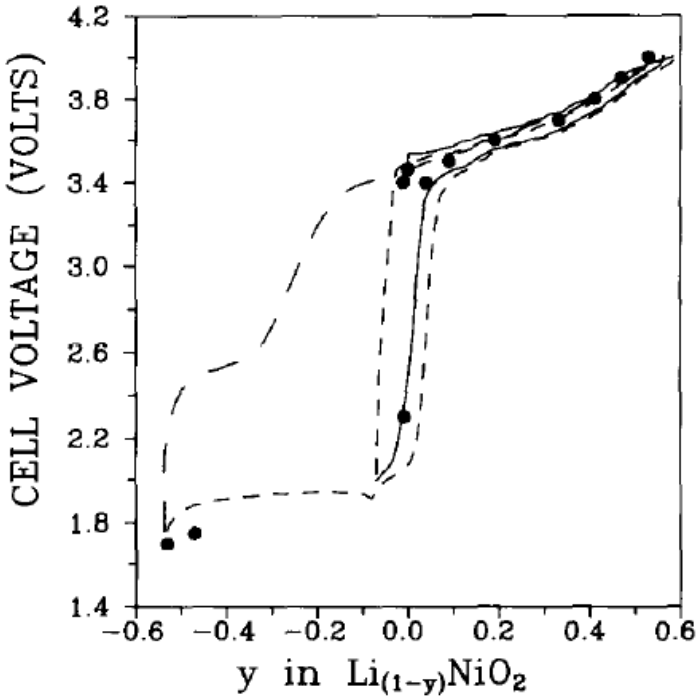

Figure 1.18. Electrochemical voltage profile of $LiNiO_2$ versus Li first cycle to lower cut-off voltage of 2 and second cycle to 1.7 V versus Li [15].

Although LNO is cheaper compared to LCO and has higher rechargeable capacity, it is difficult to reproduce LNO batches with the ideal layered structure in the laboratory.

During synthesis, the Li/Ni disorder (when Li diffuses to the transition metal layer) lowers the electrochemical activity. Furthermore, its poor thermal stability in the charged state prohibits its practical use.

Another example of layered structure is $LiNi_{0.5}Mn_{0.5}O_2$ (NMO) which is a solid solution of LNO and $LiMnO_2$ (LMO) with ratio of 1:1 . Figure 1.19 shows the voltage profile of NMO measured in lithium ion half cell. Charge/discharge voltage of NMO appear to be around 3.6 to 4.3 V which is considerably higher than LNO and LCO with higher capacity. In NMO structure, Ni is in 2^+ states and an electrochemically active ion, whereas Mn is in 4^+ states and retains its oxidation state during charge/discharge cycles. It is believed that Mn^{4+} gives the compound its structural stability during the electrochemical process. Thermal stability measurements of NMO shows that the structure is stable even at temperatures as high as 300 ^oC while above structural degradation occurs. However the presence of Ni in lithium layers blocks the lithium diffusion path and lower the performance of material during extraction of lithium from the structure.

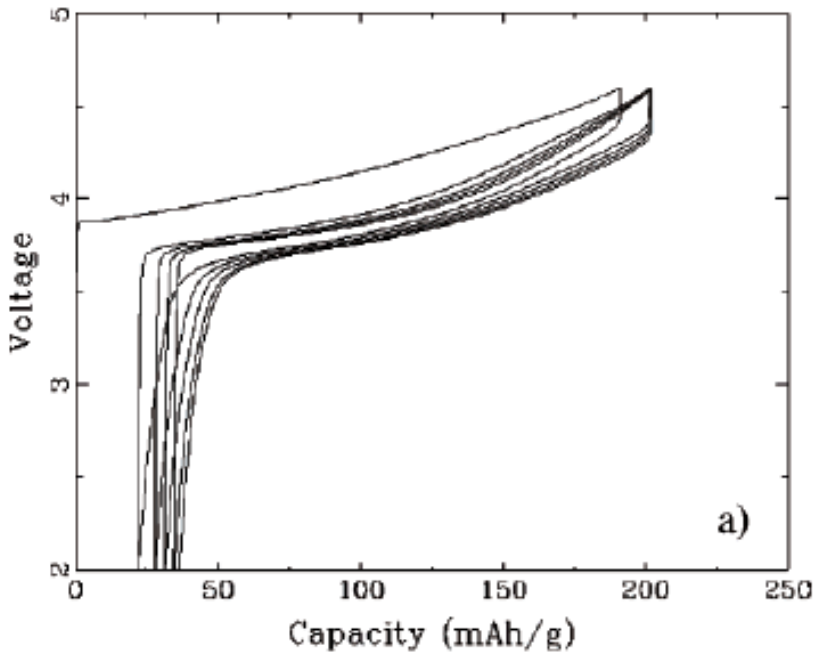

Figure 1.19. Electrochemical voltage profile of NMO between 2 and 4.6 V v.s. Li [16].

Since NMO compounds had the issue of Li-Ni disordering in their structure, attempts have been made to fabricate new oxide materials as cathode in Li-ion batteries. A promising alternative, containing three transition metal ions (ternary systems): Co, Mn,

and Ni with a composition $LiCo_xNi_xMn_{1-x-y}O_2$ was reported. The composition with equal amounts of transition metal ions, $LiCo_{1/3}Ni_{1/3}Mn_{1/3}O_2$ (NMC), showed the best electrochemical performance with high operating voltages (~4.7 V) [17]. This structure showed very promising electrochemical performance, delivering more than 200 mAh/g capacity when couple with lithium metal in the half cell, and cycle between 3 and 4.6 volt. Figure 1.20 shows the voltage profile of NMC.

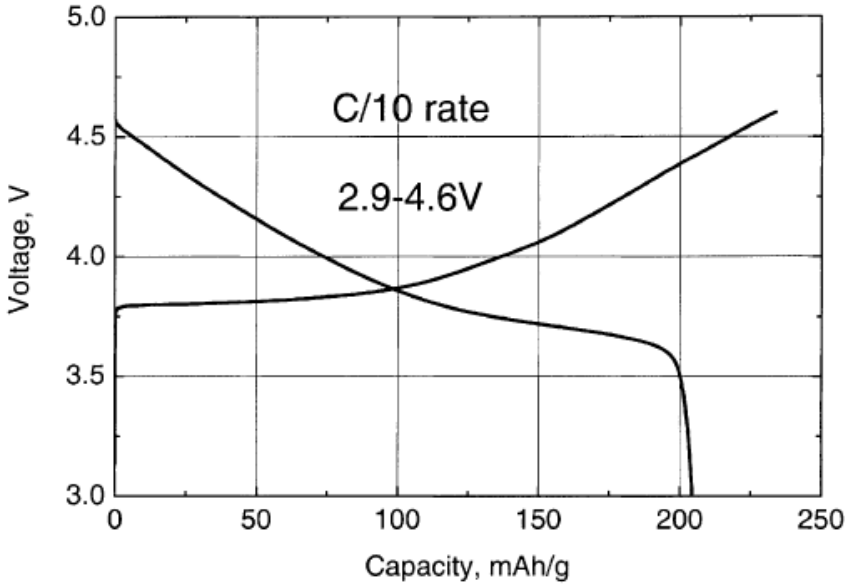

Figure 1.20. Electrochemical voltage profile of NMC cycled between 2.9 and 4.6 V v.s. Li [17].

It also showed excellent cyclability (Figure 1.21. a&b) even at high rate of 5C without any crystal change in the structure.

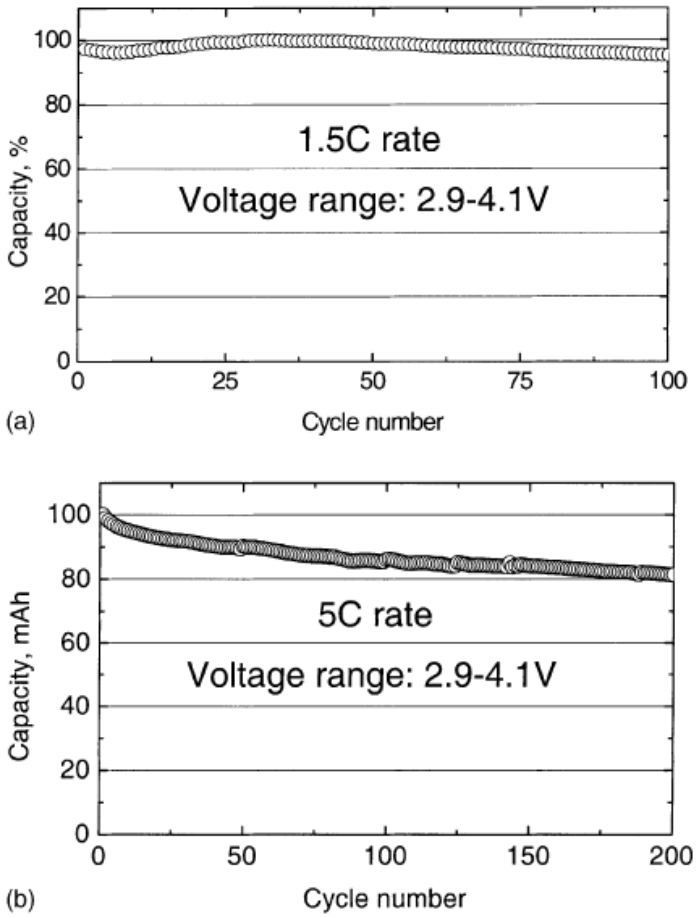

Figure 1.21. Discharge capacity versus cycle number for NMC cycled between 2.9 and 4.1 V [17].

This make NMC very promising cathode material for high power and high density applications. Co seems to prevent the Li-Ni disordering in the structure. However, in this structure also presence of lithium in transition metal layer cannot be avoided, and also when aged at elevated temperature (around 70 ^{o}C) layered structure changes to spinel-like structure.

1.5.2 Spinel structure

As mentioned before, ($LiMn_2O_4$) LMO is the most famous example of oxides with spinel structure. This compound is low cost, environmentally friendly, and safer compared to other cathode materials. The framework of MnO_2 in this structure provides three dimensional (3D) diffusion pathway for Li ions which allows excellent rate capability for Li intercalation/deintercalation. In this structure, Mn ions occupy one quarter of

octahedral sites in the Li layer, therefore one quarter of octahedral sites remain vacant. Unfortunately, this compound suffers from capacity fading over cycling at elevated temperature. The main reasons for capacity fading of this material is the Mn dissolution in the electrolyte by corrosion. In addition, it has been seen that the structure changes from spinel to tetragonal which also leads to capacity fade. Therefore, despite being low cost, the practical capacity and energy density of this compound are less than other cathode materials and limits their applications to high energy, low power system. The electrochemical properties of this compound can be clearly seen in Figure 1.22, compared to other cathode oxides.

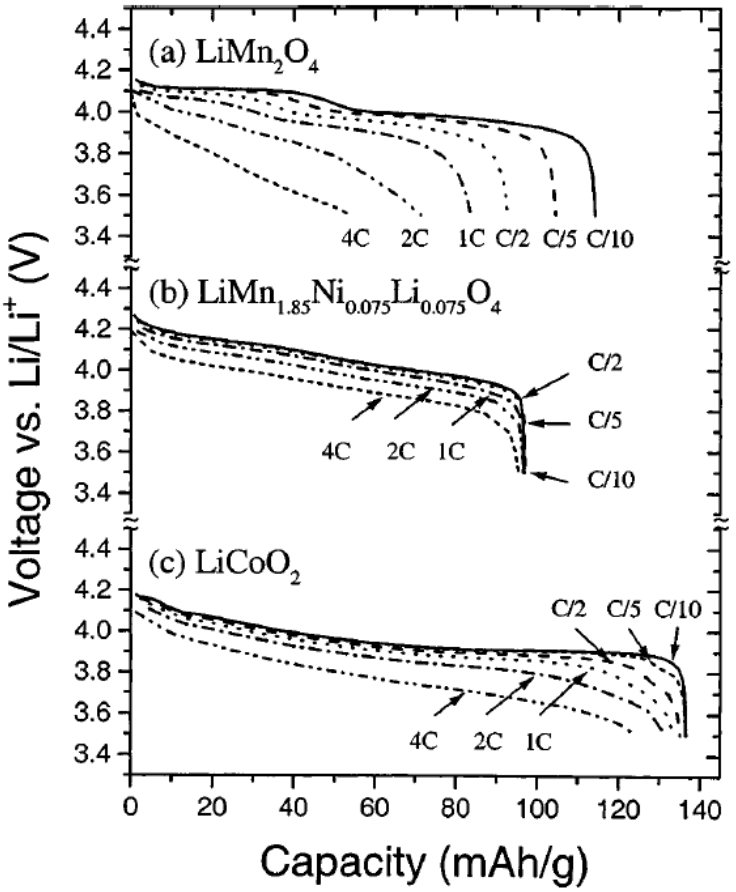

Figure 1.22. comparision of electrochemical voltage profile of a) LMO , b) NMO and c) LCO at different rates as mentioned in the figure [18].

Various materials have been used to dope in this structure in order to suppress Mn dissolution in this compound. Ni doped NMO with composition of $LiNi_{0.5}Mn_{1.5}O_4$ shows the best electrochemical performance compared to NMO doped with other metals. It shows a high operating voltage with high rate capability. Figure 1.23 shows voltage profile of some of these compounds. The capacity retention for, and operating voltage for these compounds is in the following order : Ni > Cr > Fe > Co .

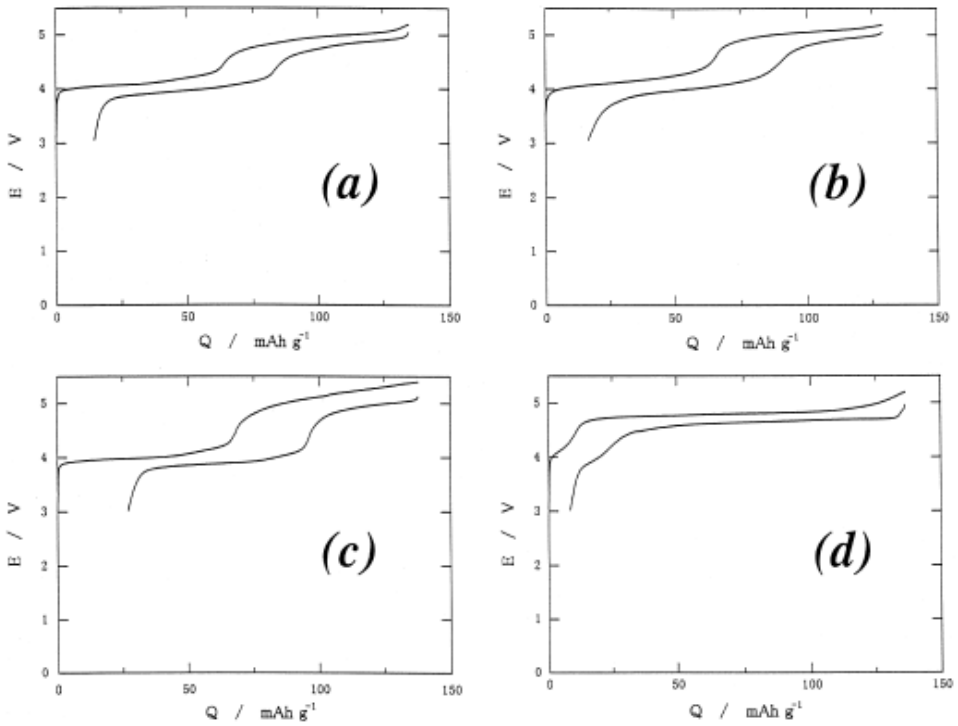

Figure 1.23. Charge and discharge voltage profile of NMO doped with a) Cr, b) Fe, c) Co, and d) Ni [19].

In NMO Ni is in +2 state and Mn in +4 state. During charge/discharge cycle, the redox couple Ni^{2+}/Ni^{4+} and Mn^{3+}/Mn^{4+} broadens the operating voltage window to 4.7 V and increase the energy density compared to LMO. However, the generation of pure NMO phase is very difficult since small amount of Ni oxide is easily produced as impurity. Despite better cyclability of NMO, during cycling, electrolyte decomposition happens at the surface of electrode due to the high potential of the Ni^{2+}/Ni^{4+} redox couple. This electrolyte decomposition leads to a thick SEI layer on the surface of cathode, and leads

to impedance rising . Electrode coating could prevent both electrolyte oxidation and Mn dissolution in this compound.

1.5.3 Olivine structure

$LiFePO_4$ (LFP) is a typical cathode material with olivine structure. This structure was proposed by Goodenough group in 1997 for the first time [20]. LFP has been considered as a very promising cathode material due to its low cost, abundant availability of iron, low toxicity, high specific capacity, low capacity fade and high safety. LFP shows a flat discharge voltage plateau at 3.4 V, and a theoretical capacity of 170 mAh/g which is almost achievable practically. Figure 1.24 shows voltage profile of LFP when coupled with lithium metal in a half cell.

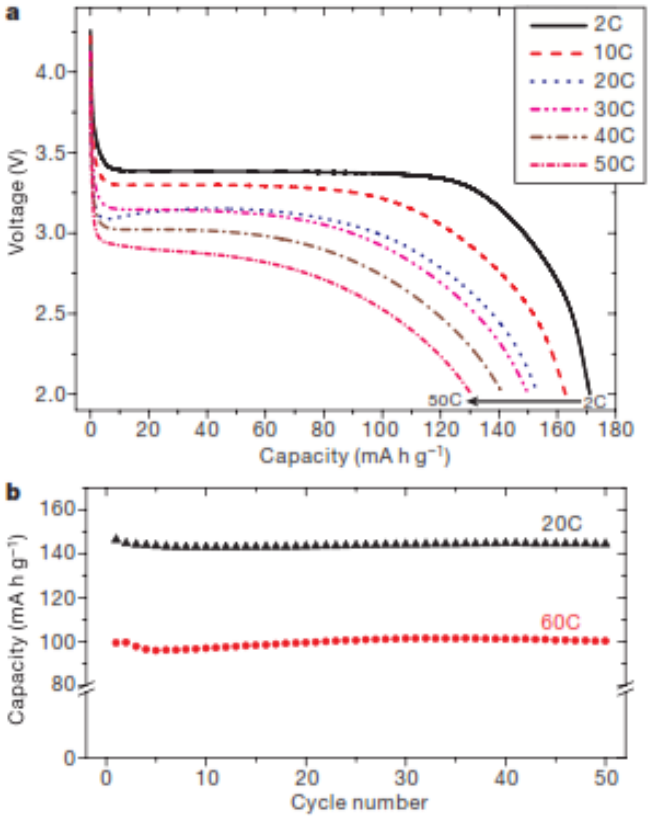

Figure 1.24. a) Electrochemical voltage profile of LFP versus Li at different rates and b) Discharge capacity versus cycle number at two different temperature as mentioned in the figure [21].

However, LFP suffers from low conductivity and many attempts have been made to improve it. One strategy is decreasing the particle size in order to decrease the diffusion length of both Li ions and electrons which leads to higher rate capability of the material.

Higher conductivity of the electrode could be achieved also by coating a conductive layer on the surface of LFP or/and doping with other elements. Carbon coating appears to be very useful in increasing the conductivity and nano-structured LFP with higher surface area also can nicely improve the rate capability. However, producing LFP using the conventional solid state reaction could end up with large particles and low surface area due to the particle growth and agglomeration, during calcinations at high temperature. Hydrothermal and sol gel seem to be good techniques in achieving LFP nano-particles which could deliver up to 157 and 123 mAh/g at the rate of 1C and 10C respectively. It should be mentioned that high surface area could be a disadvantage when higher surface of material accelerate parasitic reaction occurring on the interface of electrode/electrolyte. These parasitic reactions can consume active lithium in the battery and increase the capacity fade over time and cycling. Therefore a mix of these techniques, is very useful to increase the electrical conductivity of LFP and improve its electrochemical performance.

1.6 Na-ion batteries – a promising alternative to Li-ion batteries.

1.6.1 Why Na-ion battery?

Lithium ion battery technology is a mature technology with high efficiency, but there are some issues regarding safety and cost of these batteries. On the other hand, lithium raw material has been vigorously demanded for use in Li-ion batteries and it turned lithium to a costly material. Figure 1.25 shows the demand for lithium in different technologies during first decade of this century.

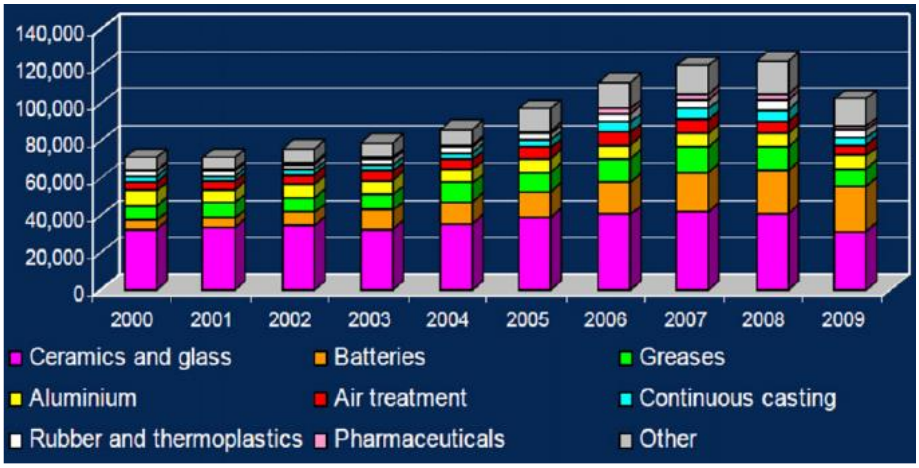

Figure 1.25. Lithium carbonate demand by applications [22].

About ¼ of all lithium containing precursors are consumed in Li-ion battery manufacturers. This caused a rapid rise in price of Li_2CO_3 (figure 1.26) just one decade after commercializing the Li-ion batteries.

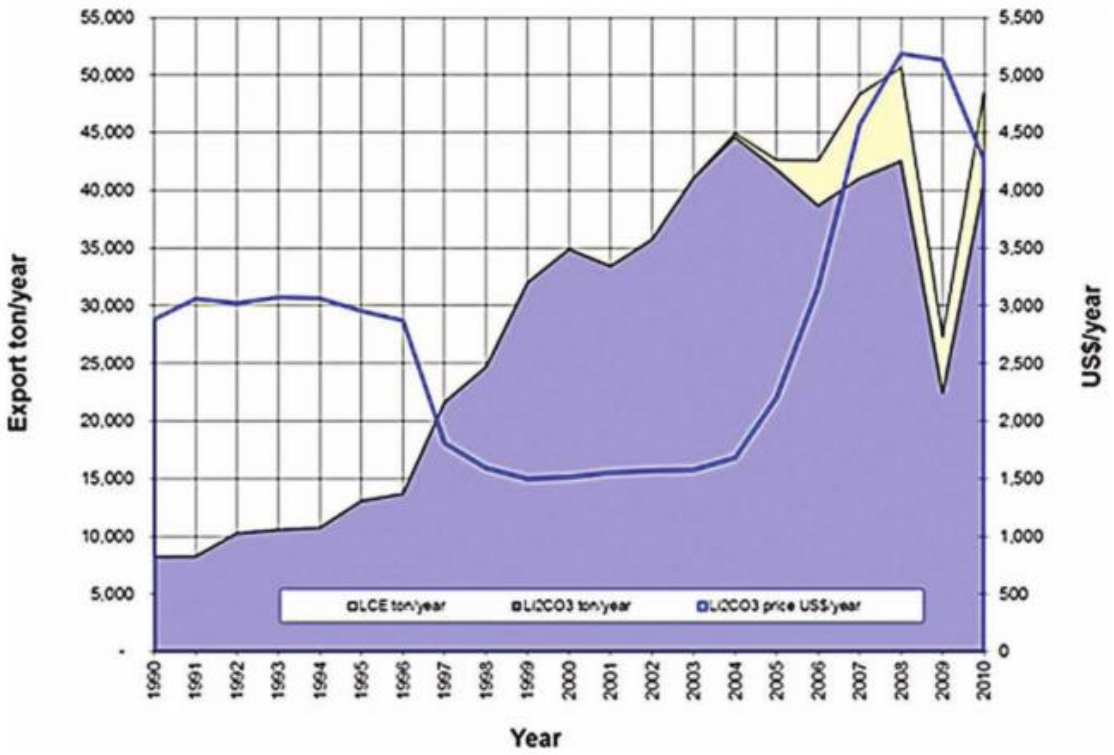

Figure 1.26. Fluctuation of price and production of lithium carbonate over time [23].

The other important issue related to the lithium raw material is that it is not uniformly spread within the earth crust and makes it a strategic material. As figure 1.27 shows more than 43% of lithium resources are located in south America, and as Tarascon mentioned in reference 24, South America could become “new Middle-East” soon.

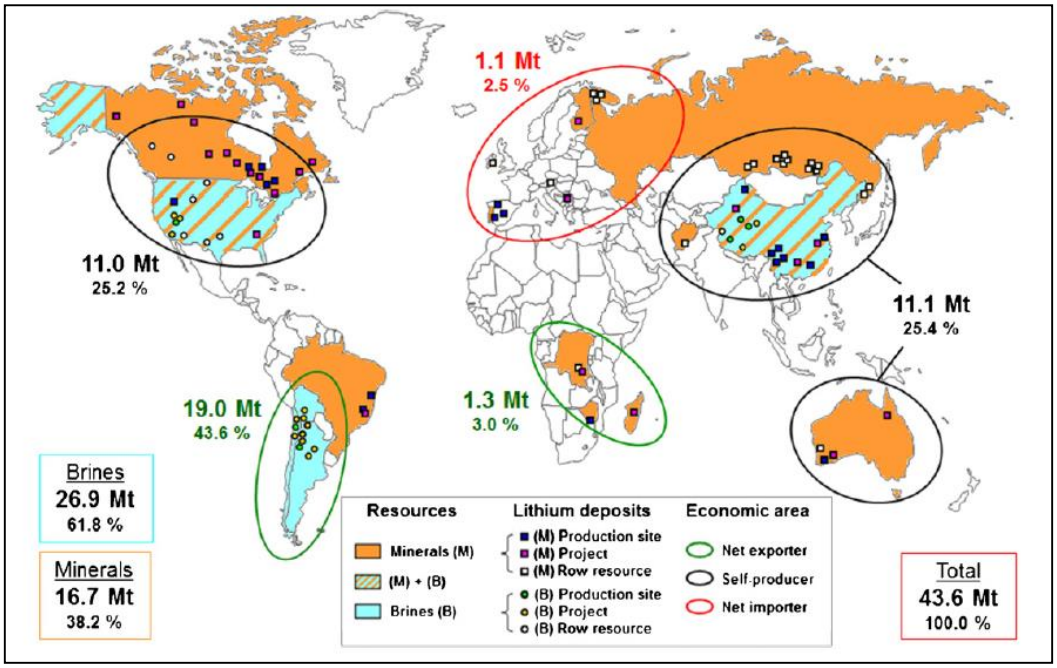

Figure 1.27. Map of lithium resource availability on the earth crust [23].

Based on wide availability and low cost of sodium, sodium ion battery have the potential to meet the large scale energy storage needs. The abundant resources and much lower cost of sodium carbonate compared to that of lithium carbonate (~$150/ton for sodium and $5000/ton for lithium) makes Na-ion batteries very promising alternative for Li-ion batteries. However, there are some disadvantages in Na-ion battery. Sodium with atomic number of 11 has larger atomic radius compared to lithium, which need a host intercalating material with larger free spaces that allow Na-ion to insert and extract reversibly. The standard potential of Na/Na^+ is 0.34V higher than that of Li/Li^+ which make Na-ion battery energy density less than that of lithium ion battery, when their own metal is used as anode. In addition, lower melting temperature of sodium compared to lithium (97.7 ^oC , 180.5 ^oC respectively) arises some safety concerns, and limits their potential application.

1.6.2 Negative electrode

It is generally known that sodium does not intercalate into graphite and it is electrochemically inactive in a sodium salt electrolyte. The chemical potential of sites between graphene layers are less than the chemical potential of sodium, and it is more thermodynamically favorable for the sodium to electroplate on the surface of material. However, it seems that other disorder carbonaceous material can intercalate sodium.

Dahn reported electrochemical insertion of sodium in hard carbon in 2000 with a insertion mechanism very similar to that of lithium insertion. Figure 1.28 shows the voltage plateau of Li and Na insertion into the hard carbon.

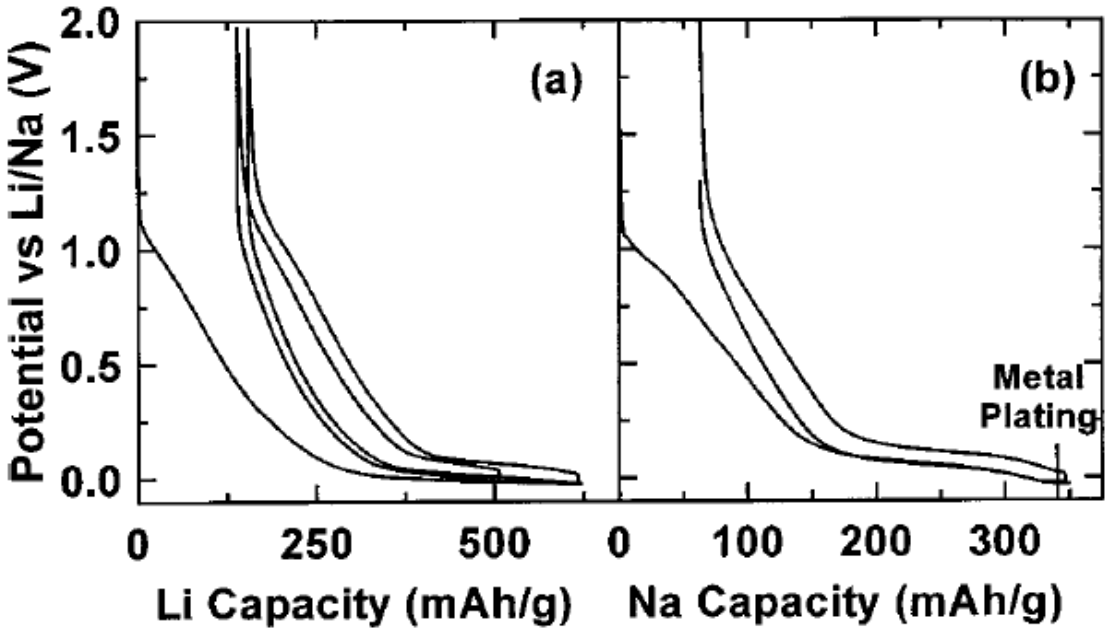

Figure 1.28. Electrochemical profile of Hard carbon versus a) lithium and b) sodium [25].

Two plateau that have been seen and discussed in section 1.4.3 of this thesis for lithium insertion in hard carbon are clearly seen in voltage profile of Na insertion in hard carbon suggesting similar intercalation mechanism.

1.6.3 Positive electrode

Layered structure $Na_xMn_{1-y}Fe_yO_2$ was reported as a material of choice for positive electrode of Na-ion batteries [26]. Fe and Mn in this structure are low cost and abundant in the earth crust and meet the industrial requirements. They showed that this compound can intercalate sodium up to 140mAh/g between 1.5 V and 3.8V versus Na/Na^+.

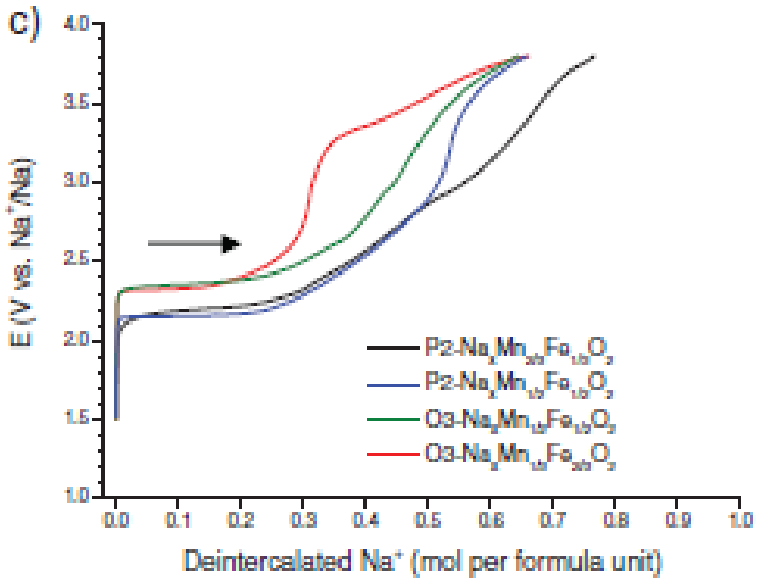

Figure 1.29. Electrochemical voltage profiles of $Na_x(MnFe)O_2$ [26].

Figure 1.29 shows first charge voltage profile of different phases of this compound. All phases exhibit a plateau at the beginning of the charge, corresponding to existence of a biphasic domain. The plateau is slightly higher in voltage for the O3 phases (+0.2 V versus P2 phases) indicating a higher energy required to remove Na-ions from the inter-layer space in the O3 oxygen stacking, and it explains why the discharge capacities of the O3 phases are lower than the ones observed for the P2 phases.

A summary of potentials and theoretical capacity for positive and negative electrode materials suitable for Na-ion batteries is presented in figure 1.30. Many of these materials are very similar to those that have been studied over years for Li-ion batteries, including layered structures, olivines and compounds with the NASICON framework.

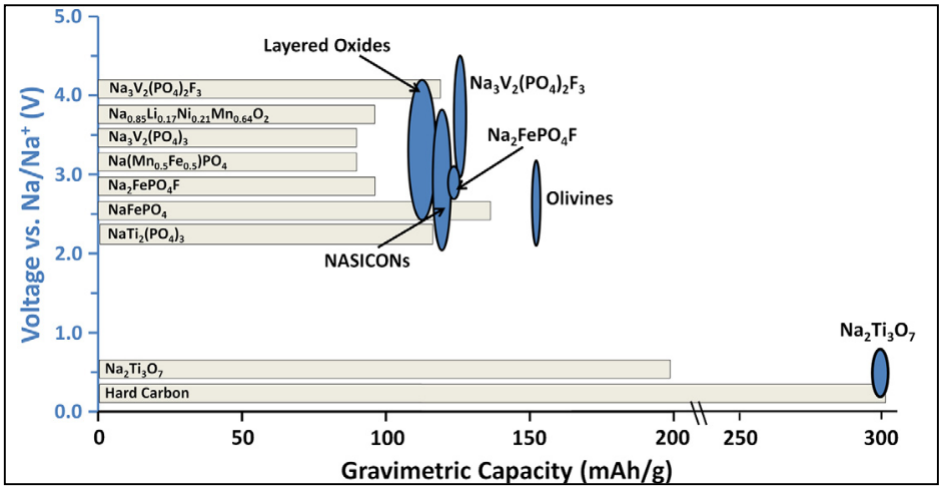

Figure 1.30. Negative and positive intercalation materials for Na-ion batteries. Theoretical capacity of the compounds are shown with blue curve, while achieved capacities are shown with gray bars [27].

1.7 The aim of thesis

Energy storage devices specially secondary (rechargeable) batteries play important role in modern society. Development of secondary battery systems which can be used in many applications requires many years of R&D efforts. In this thesis we tried to have wide look at different aspects of secondary batteries including materials and lifetime . In chapter 2 investigation of carbon based materials as high energy anodes for Li-ion batteries is presented. This is very critical in increasing the energy density of Li-ion batteries to be suitable for application such as electric cars. In fact many material scientist are putting a great deal of effort into studies of materials which can intercalate more lithium during cycling. Chapter 3 and chapter 4 are dedicated to studies of degradation mechanisms of Li-ion batteries. It is important to study Li-ion cells throughout their lifetime to be able to determine the failure mechanisms. Aged Li-ion cells were studied in chapter 3 to understand the mechanism of degradation over their lifetime of up to 12 years. Effect of discharge rate on capacity fading of Li-ion pouch cells is presented in chapter 4.

Chapters 5 and 6 are devoted to studies of electrode materials for Na-ion batteries. Studies of thick films of Sn, as negative electrode for Na-ion batteries is presented in chapter 5, while the promising $Na_{0.44}MnO_2$ cathode material is investigated by advanced electrochemical techniques and presented in chapter 6.

References :

1. M.S. Whittingham, Electrical energy storage and intercalation chemistry, Science, 192, 1126 (1976)
2. K. Ozawa, Lithium-ion rechargeable batteries with LiCoO2 and carbon electrodes: the LiCoO2/C system, 69, 212 (1994).
3. H. D. Yoo, et al, On the challenge of developing advanced technologies for electrochemical energy storage and conversion, Material. Today. 17, 110 (2014).
4. R. Yazami, Surface chemistry and lithium storage capability of the graphite - lithium electrode, Electrochem. Acta, 45, 87 (1999).
5. U. V. Sacken, et al. Comparative thermal stability of carbon intercalation anode and lithium metal anodes for rechargeable lithium batteries, J. Power. Sources, 54, 240 (1995).
6. H. G. Jung, et al. Microscale spherical carbon-coated Li4Ti5O12 as ultra high power anode material for lithium batteries, Energy. Environmentla. Science. 4, 1345 (2011).
7. M. N. Obrovac, et al., Alloy design for lithium ion battery anode, J. Electrochem. Soc. 154, A849 (2007).
8. J. H. Riu, et al., Failure Modes of Silicon Powder Negative Electrode in Lithium Secondary Batteries, Electrochem. Solid. State. Lett. 7, A306 (2004).
9. Y. Yao, et al., Interconnected Silicon Hollow Nanospheres for Lithium-Ion Battery Anodes with Long Cycle Life, Nano. Lett. 11, 2949 (2011).
10. H. Wu, et al., Stable cycling of double-walled silicon nanotube battery anodes through solid–electrolyte interphase control, Nature. Nanotech., 7, 310 (2012).
11. Dahn JR, Zheng T, Liu Y, Xue JS. Mechanisms for lithium insertion in carbonaceous materials. Science, 270, 590 (1995).
12. D. A. Stevens, and J. R. Dahn, High capacity anode materials for rechargeable sodium batteries, 147, 1271 (2000).
13. W. Xing, et al., Studies of lithium insertion in ballmilled sugar carbons, J. Electrochem. Soc, 145, 62 (1998).
14. T. Ohzuku, and R. J. Brodd, An overview of positive electrode materials for lithium ion batteries, J. Power. Sources, 174, 449 (2007).
15. J. R. Dahn, U. V. Sacken, C. A. Michal, Structure and electrochemistry of LiNiO2 and a new Li2NiO2 phase with the Ni(OH)2 structure, 44, 87 (1990).

16. J. Breger, et al., Effect of High Voltage on the Structure and Electrochemistry of LiNi0.5Mn0.5O2: A Joint Experimental and Theoretical Study, Chem. Mater. 18, 4768 (2006).

17. I. Belharouak, et al., Li(Ni1/3Co1/3Mn1/3)O2 as a suitable cathode for high power applications, J. Power. Sources, 123, 247 (2003).

18. Y. Shin , and A. Manthiram, Factors effecting the capacity fade of spinel lithium manganese oxide, J. Electrochem. Soc.,151, A204 (2004).

19. T. Ohzuku, et al., Solid-state redox potentials for LiwMe Mn xO Me: 3d-transition 1r2 3r2 4 metal/ having spinel-framework structures: a series of 5 volt materials for advanced lithium-ion batteries, J. Power. Sources, 81, 90 (1999).

20. A. K. Padhi et al., Phospho olivins as positive electrode materials for lithium ion batteries, J. Electrochem. Soc., 144, 1188 (1997).

21. B. Kang, and G. Ceder, Battery materials for ultra fast charging and discharging, Nature. Lett., 458, 190 (2009).

22. G. Grosjean et al., Assessment of world lithium resources and consequences of their geographic distribution on the expected development of the electric vehicle industry, Renewable & sustainable Enr. Rev. 16, 1735 (2012).

23. M. D. Slater, Sodium ion batteries, Advanced. Func. Mater. 23, 947 (2013).

24. J. M. Tarascon, Is Lithium the new gold?, Nature, 2, 510 (2010).

25. D. A. Stevens, and J. R. Dahn, The mechanisms of lithium and sodium insertion in carbon materials, J. Electrochem. Soc., 148, A803 (2001).

26. B. M. Boisse et al., Structural and Electrochemical Characterizations of P2 and New O3-NaxMn1-yFeyO2 Phases Prepared by Auto-Combustion Synthesis for Na-Ion Batteries, J. Electrochem. Soc. 160, A569 (2013).

27. B. L. Ellis, and L. Nazar, Sodium and sodium ion energy storages, Current. Opp. Solid. State. Material. Science. 16, 168 (2012).

CHAPTER 2

High capacity negative electrode for Li-ion batteries

2.1 Introduction

New electrode materials play a crucial role in increasing the energy density of LIBs, and are interesting from a practical viewpoint if they can reversibly host more lithium during intercalation and de-intercalation at a reasonable voltage. Although metal alloying systems; like $Li_{3.75}Si$ have extremely high specific capacity, issues related to high volume expansion of the Si electrode after lithiation [1-3**]** have delayed the practical implementation of Si-based negative electrodes. Various schemes have been proposed to produce sophisticated Si nanostructures which can overcome some of the difficulties associated with the use of Si [4-6]. However, these schemes appear to be expensive, and do not meet industrial requirements. With this in mind it is worth to investigate novel forms of carbon very carefully as carbon or graphite are the negative electrode materials of choice of Li-ion batteries [7].

As it has been discussed in chapter 1, there are three main types of carbonaceous materials which show dramatic differences in voltage-capacity profiles and in intercalation mechanism during the lithiation/delithiation process [8]. Graphitic carbons which are used commercially as negative electrode materials in LiBs can intercalate up to one lithium atom per six C atoms at room temperature leading to a specific capacity of 372 mAh/g. Nanoporous hard carbons show a specific capacity around 550 mAh/g but most of this capacity is delivered only 10 mV above the Li plating potential (safety issue) and they also show low density. Hydrogen-containing carbons can show capacities up to 900 mAh/g but these suffer from large charge-discharge voltage hysteresis and low density. Additionally, both the nanoporous hard carbons and the hydrogen containing carbons have large irreversible capacities [9]. Finally it has been shown that surface functional groups, for example containing oxygen, play an important role in the voltage hysteresis during electrochemical lithiation and delithiation [10, 11].

Recent work by Subramanian et al**.** [12] showed that sputtered carbon can have a reversible specific capacity near 600 mAh/g with small hysteresis. Figure 2.1 shows some of their electrochemical results, obtained from their sputtered carbon in a lithium ion half cell. Additionally, some works by Dahn group on combinatorial sputtered films of Si_xC_{1-x} or $[Sn_{0.55}Co_{0.45}]_{1-y}C_y$ ($0 < y < 0.5$) [13, 14], and Obrovac group on $Zn_{1-x}C_x$ [15] showed that films with $x \cong 1$ (almost pure carbon) gave specific capacities near 800 mAh/g.

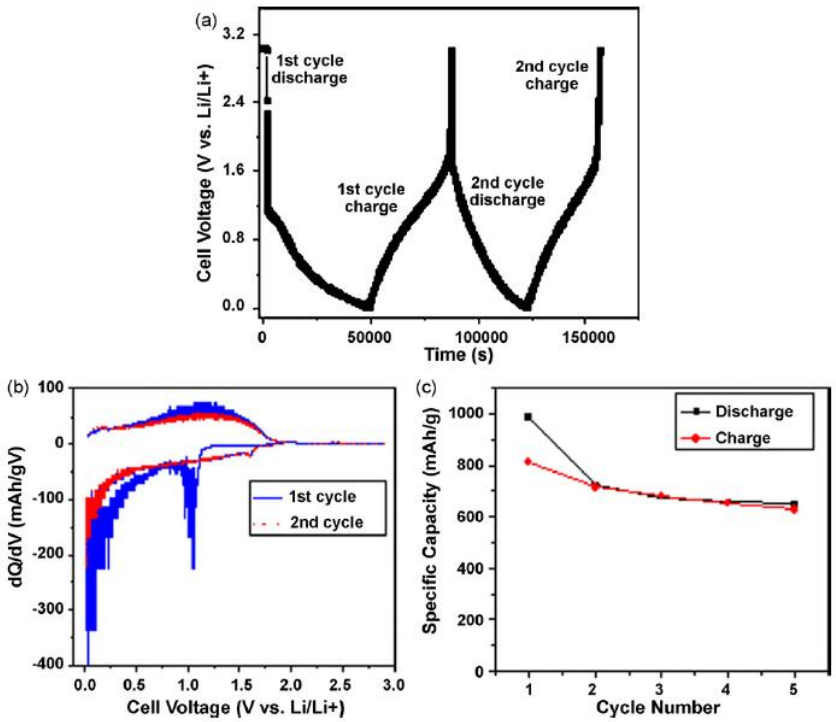

Figure 2.1. (a) Charge–discharge curves for the sputter deposited carbon film at 0.2 C rate in a 1MLiPF6/EC:DEC electrolyte cycled between 3 and 0.005 V. (b) Differential capacity plots. (c) Cycling performance of the sputter deposited carbon film at 0.2 C rate in a 1M LiPF6/EC:DEC electrolyte cycled between 3 and 0.005 V. [12].

Figure 2.2 also shows voltage profiles versus capacity for different libraries of Zn-C, obtained from combinatorial sputtering technique.

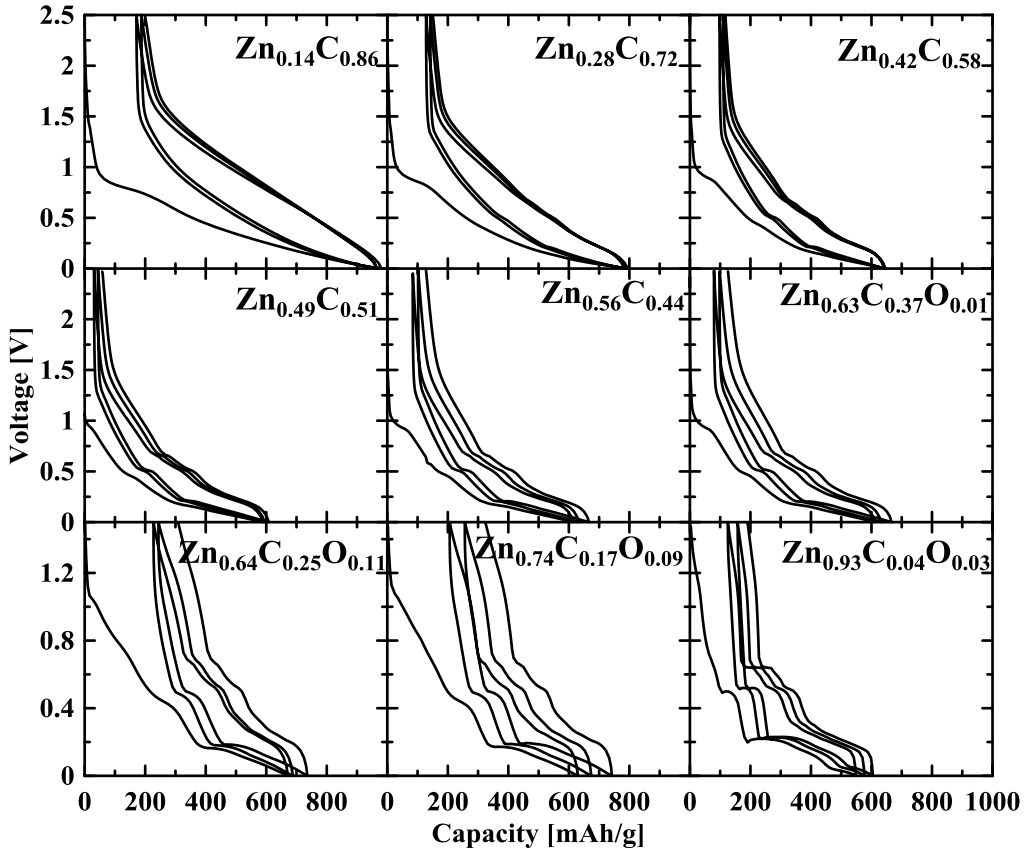

Figure 2.2. Voltage profiles of ZnC films, the composition of films are indicated in the figure [15].

However, a deeper analysis of pure sputtered carbon films is still missing and this chapter is devoted to such investigation.

2.2 Preparation of Carbon samples

Carbon films were sputtered on different substrates for different kinds of characterization. Silicon wafer substrates for electron microprobe analysis and half-taped silicon wafers for thickness measurements using a profilometer were included in each sputtering run. Alumina or quartz were used as substrates for heating the sputtered carbon films and copper foil disks were used as current collector for the films to be measured in the Li/carbon coin cells. Polystyrene film substrates (25 micrometers thick) were used to recover sputtered carbon as powder flakes after dissolving the polystyrene film in toluene. The recovered powder was rinsed up to 10 times in toluene to minimize the amount of residual polystyrene. Figure 2.3 shows the sputtering rotating table with different

mentioned substrates. Almost half area of table is covered with polystyrene film in order to recover as much carbon as possible.

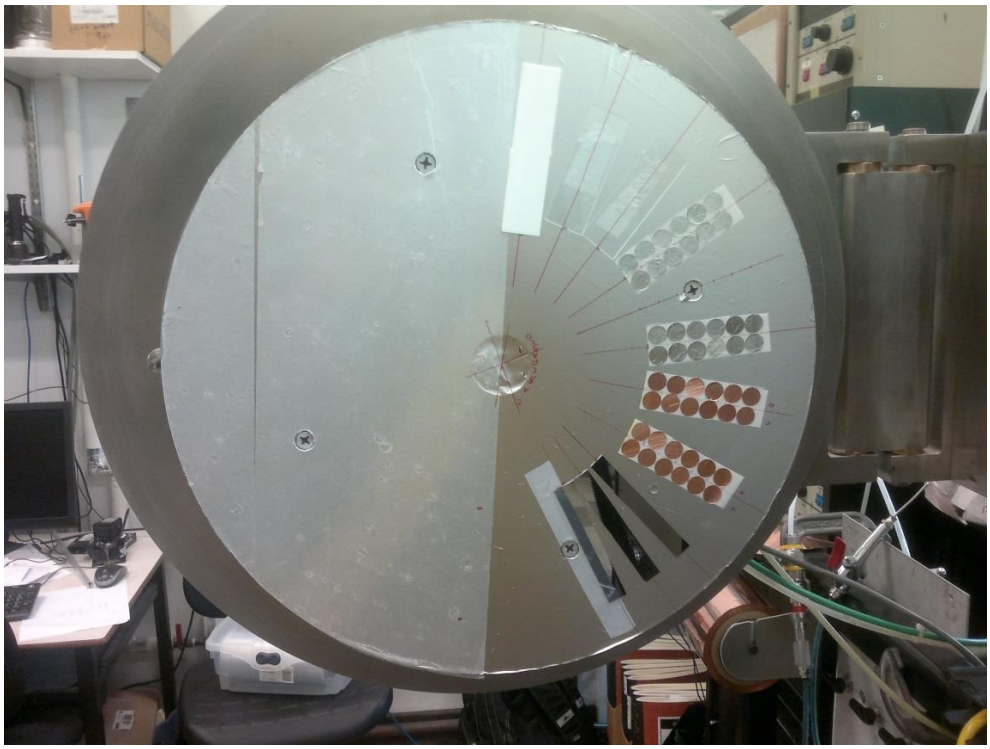

Figure 2.3. Sputtering rotating table loaded with different substrates.

The sputtering system used was a modified Corona V3-T magnetron deposition system (Corona Vacuum Coaters, Vancouver, BC Canada). The base pressure prior to deposition was about 3×10^{-7} Torr and the depositions were done under an argon gas pressure of 1, 6, 16, or 30 mTorr. Three 50mm diameter graphite targets (obtained from Kurt J. Lesker with a purity of 99.999 %) were used and were sputtered with a DC power of 150W. The various substrates were arranged on the rotating substrate table so that all the substrates passed sequentially under the three targets during film deposition.

2.3 Materials characterization

The copper current collector disks were weighed (before and after sputtering) using a SE2 Sartorius microbalance with 0.1 µg accuracy. Films thickness was measured using a Veeco Dektak 8 stylus profilometer. Carbon sputtered on Si was used in electron microprobe experiments to determine the chemical composition. Electron microprobe measurements were made using a JEOLJXA- 8200 super probe. Scanning electron

microscope (SEM) images were collected with a Hitachi S-4700 SEM. Powder X-Ray diffractometer (XRD) analysis was made using a Siemens D5000 diffractometer equipped with a copper target x-ray tube and a diffracted beam monochromator. Sputtered carbon powder (recovered from the polystyrene substrate) was placed on a Si (510) zero background holder for the XRD measurements. XRD measurements used a counting time of 60 seconds per 0.05 degree step. Raman experiments were done using a T64000 Raman Spectrometer (Horiba Jobin Yvon, Edison, NJ) with a JDS Uniphase 632.8 nm, 3 mW HeNe laser. The grating was 1800 grooves/mm and samples were collected over three integrations of 20 seconds each. Carbon powder collected from the polystyrene film was sent to Canadian Microanalytical Services (CMAS, Delta, B.C.), for determination of the oxygen and nitrogen content.

2.4 Characterization results

Table 2.1 shows the sputtering pressure, obtained density and the oxygen and nitrogen content in the samples achieved in 4 different sputtering runs.

Table 2.1 - Density, the oxygen and nitrogen content in the samples achieved in 4 different sputtering runs.

Sample	Sputtering pressure (mT)	Film density (g/cm^3)	O_2 content (wt %) Microprobe	N_2 content (wt%) Microprobe	O_2 content (wt %) CMAS	N_2 content (wt %) CMAS
SC_1	1	1.9±0.3	<1	<1	0.67	3.05
SC_6	6	1.9±0.3	3± 0.3	<1	–	_
SC_{16}	16	1.5±0.2	11± 0.5	2±0.2	_	_
SC_{30}	30	1.3±0.2	13± 0.5	5± 0.4	21.2	3.5

Sample labels were selected based on sputtering pressure; for instance SC_1 stands for "carbon sputtered at 1 mT Argon pressure" and so on. The SC_1 and the SC_{30} films were 1.0 μm and 1.4 μm in thickness, respectively. The intermediate films showed intermediate thicknesses. The amount of nitrogen and oxygen incorporated in the films are quite low in films SC_1 and SC_6, which is due to the low surface area of the sputtered carbon at these pressures. SC_1 and SC_6 have also extremely high density with respect to

carbons having high capacity for lithium made by pyrolysis of organic precursors in inert gas. Considering the error in the density calculation, the SC_1 and SC_6 samples have a density close to that of commercial graphite (graphite density: 2.09 - 2.23 g/cm^3), which is favorable in order to have high volumetric capacity (Figure 2.4).

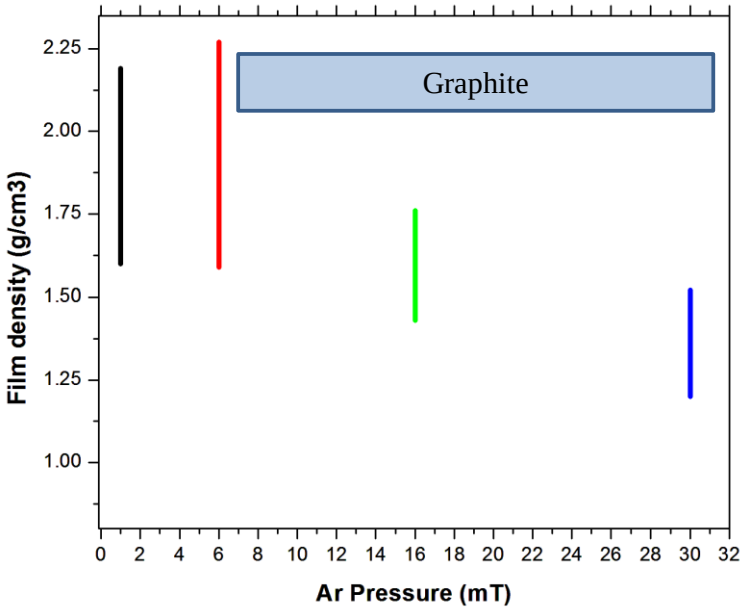

Figure 2.4. Density of carbon films obtained at different sputtering Ar pressure. Density of graphite showed in the figure for comparison.

Samples prepared at higher Ar pressure have lower densities and, presumably, higher surface area. For instance the density of SC_{30} is less than 1.5 g/cm^3 and the amount of oxygen and nitrogen in the film is larger, up to 18 wt% (Figure 2.5).

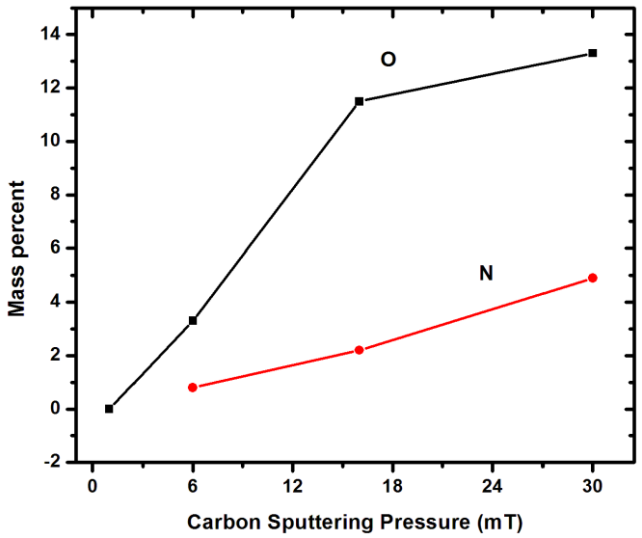

Figure 2.5 Oxygen and nitrogen content in sputtered carbon films versus Ar pressure.

Oxygen and nitrogen are incorporated at carbon atoms with unsaturated bonds upon exposure to air. The large amount of oxygen and nitrogen are consistent with the high porosity and high surface area that would result in a low density film. The oxygen and nitrogen in the SC_{16} and SC_{30} films will play a crucial role in their electrochemical behavior.

Figure 2.6 shows SEM images of the top surfaces of the SC_1 and SC_{30} films. The morphology of the SC_1 film in Figures 1a and 1b is highly compact without any apparent porosity. By contrast, the SC_{30} film shown in Figures 1c and 1d has a fluffy morphology showing clear porosity. As the sputtering pressure increases the density decreases and the porosity and surface area increase. This phenomenon is well known for sputtered films [16].

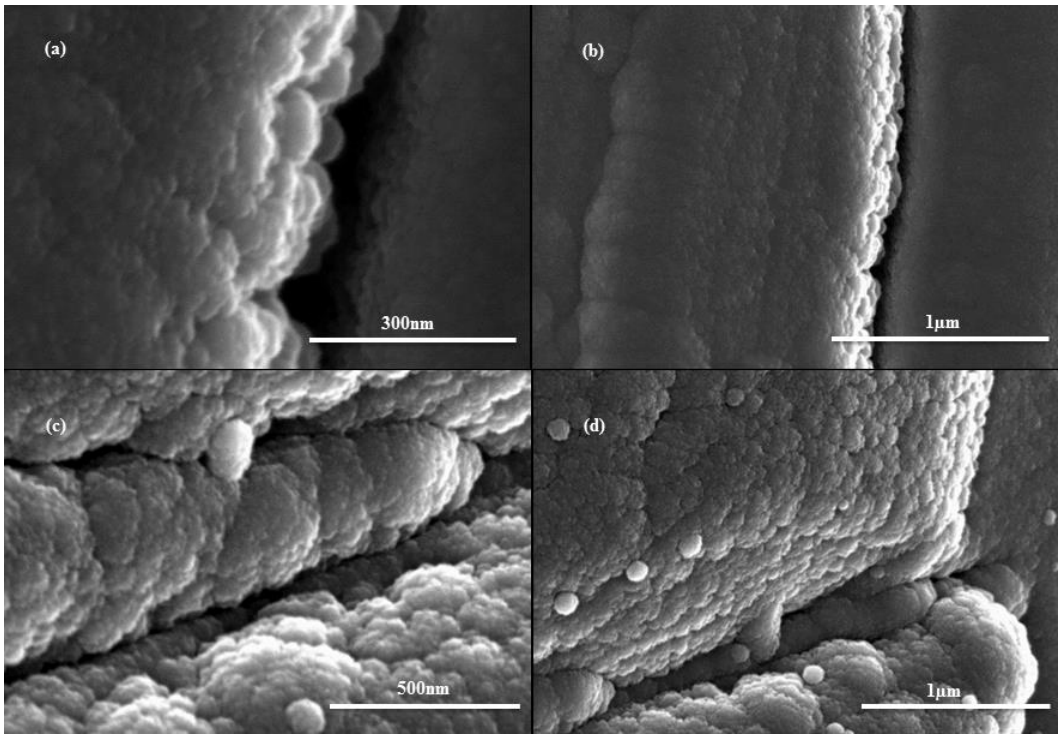

Figure 2.6. SEM images of the top surfaces of the SC_1 (a and b), and SC_{30} (c and d) films in different magnifications.

Figure 2.7 shows the powder XRD profiles of the different sputtered carbons. The intensity scales are different due to the different amount of carbon on the sample holder

for each sample. Figure 2.7a shows that SC_1 is highly amorphous with virtually no evidence of the broad (002) peak near $2\Theta=23$ shown by the other samples. After annealing the SC_1 film to 1000°C two typical broad peaks for disordered carbons at scattering angles of 25° and 45° appear as shown in Figure 2.7b. These peaks correspond to (002) and (100) Bragg peaks are seen in the as-sputtered SC_{16} and SC_{30} films (Figures 2.7c and 2.7d) which means the samples other than SC_1 and SC_6 (SC_6 has a similar structure to SC_1), have small domains of coherent graphene sheets.

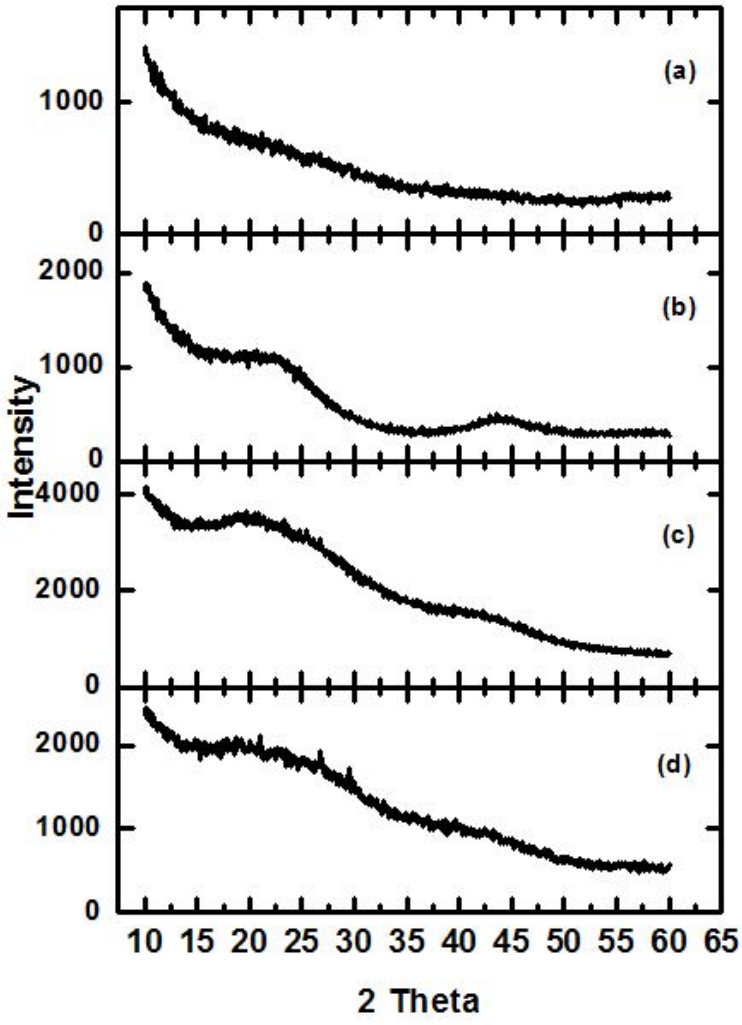

Figure 2.7. XRD profiles for samples (a) SC_1 (b) SC_1 heated to 1000°C (c) SC_{16} and (d) SC_{30}.

Figure 2.8 shows the Raman spectra of the carbon samples. For SC_1 and SC_6 (Figures 2.8a and 2.8c) there is a broad hump at around 1500 cm^{-1}, which is due to their amorphous nature with very little long range order in the carbon atoms. Figure 2.8b shows the Raman spectrum for sample SC_1 heated to 1000°C. Broad peaks corresponding to the D and G modes at around 1320 and 1590 cm^{-1}, respectively, are observed. The D peak corresponds

to disorder and it does not appear in perfect graphite [17]. The D mode arises from a breathing mode of sp^2 sites in carbon rings that are not in chains, while G mode corresponds to the stretching vibration of any pair of sp^2 sites, whether in C = C chains or in aromatic rings [18, 19]. The Raman spectra for the SC_{16}, SC_{30} and heated SC_{30} samples are shown in Figures 2.8d, 2.8e and 2.8f, respectively. SC_{16} and SC_{30} (both before and after heating to 1000°C) show broad D and G peaks very similar to the heated SC_1 sample. However, the heated and unheated SC_1 samples are much denser than SC_{16} and SC_{30} and do not contain significant amounts of oxygen or nitrogen. It is important to explore the differences between the electrochemical behavior of these samples.

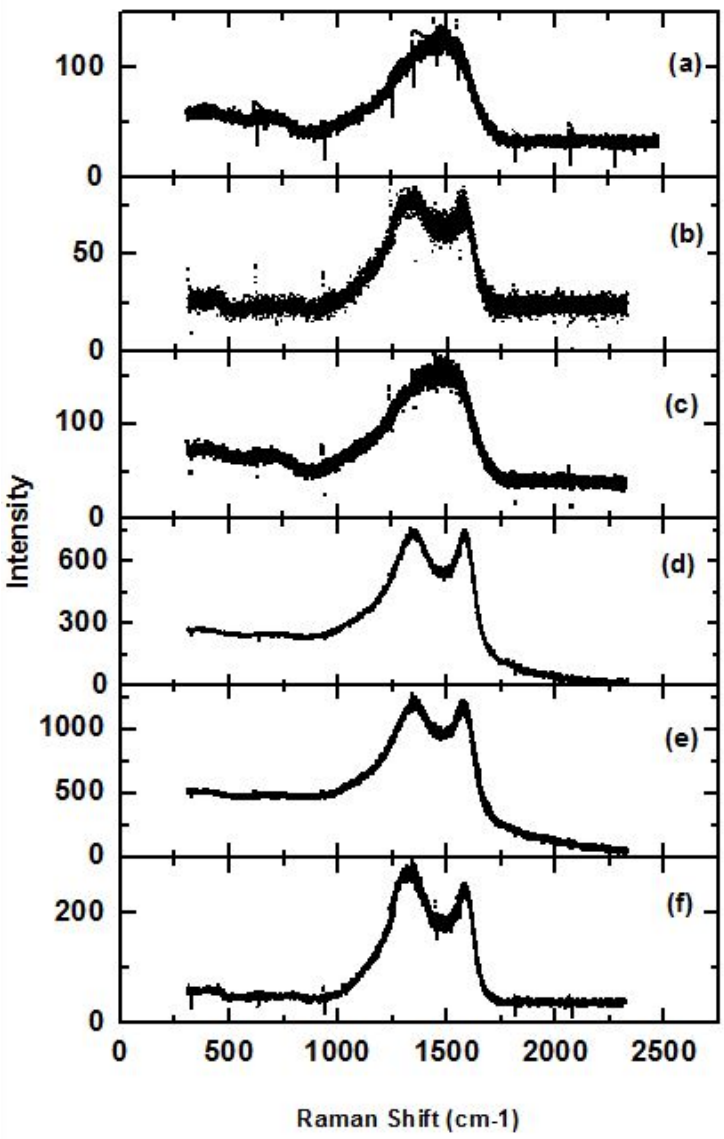

Figure 2.8. Raman spectra for (a) SC_1 (b) SC_1 heated to 1000°C (c) SC_6 and (d) SC_{16} (e) SC_{30} and (f) SC_{30} heated to 1000°C.

2.5 Electrochemical results

Figure 2.9 shows the cell voltage versus specific capacity (left) and the differential capacities versus the cell voltage (right) for all the as-sputtered samples. In the differential capacity plots, curves a′, b′, c′, d′ correspond to panels a, b, c, and d in the right half of Figure 2.9. The irreversible specific capacities in the first cycle are 205, 360, 415, and 420 mAh/g for SC_1, SC_6, SC_{16}, and SC_{30} respectively. Thus, sample SC_1 shows lower irreversible capacity with respect to the other samples.

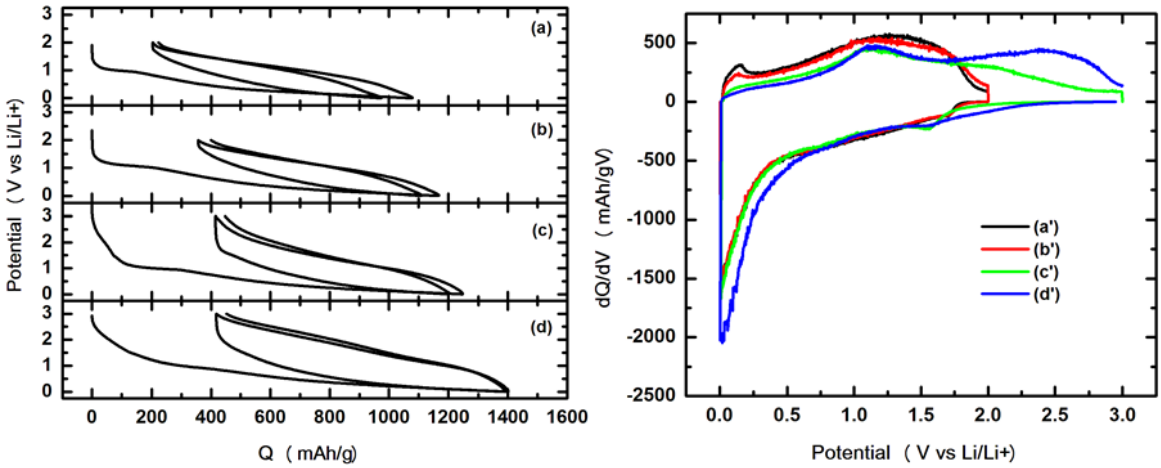

Figure 2.9. Voltage vs capacity for the first 2 cycles (left panels) for as-sputtered (a) SC_1 (b) SC_6 (c) SC_{16} and (d) SC_{30}, and the differential capacities (dQ/dV) versus cell voltage for the second cycle (right panel) for SC_1 (a′, black), SC_6 (b′, red) , SC_{16} (c′, green), and SC_{30} (d′, blue).

The irreversible capacity in the first cycle increases with increasing sputtering pressure as does the porosity, surface area and the amount of functional groups on the surface of the carbon layers. The high pressure samples with lower density probably have higher active surface area which leads to a larger irreversible capacity due to the solid electrolyte interphase (SEI) layer formation. The right panel of Figure 2.9 shows that SC_1 and SC_6 have smaller amounts of hysteresis in their voltage profiles and that they have no capacity above about 1.9 V. By contrast, SC_{30} has a large portion of its anodic capacity (about 400 mAh/g) between 2 and 3 V. SC_{16} shows an intermediate behavior. It is our opinion that the large reversible specific capacity of SC_1 and SC_6 (about 800 mAh/g) are due to Li atoms bonding near the large number of carbon atoms with unsaturated bonds which exist in the amorphous structure of SC_1. The sites would have varying local geometry, and hence binding energy for lithium throughout the film, which is why the voltage profile

extends over a 2 V range. Some of these sites are taken up by O and N in SC_{30} and SC_{16} and when Li bonds near O and N, apparently a large hysteresis results. It is also reasonable that it should be more difficult to remove a Li atom bonded near oxygen than one bonded near carbon since oxygen is a better electron acceptor than carbon – this could explain why SC_{16} and SC_{30} have substantial anodic capacity above 2 V and the larger hysteresis.

In order to understand if any ordering happens in the structure of sputtered carbon films, and to investigate its impact on electrochemical properties of films, SC_1 and SC_{30} were annealed up to 900^{o}C. The annealing time at the final temperature was 10 minutes. Figure 2.10 shows the annealing procedure.

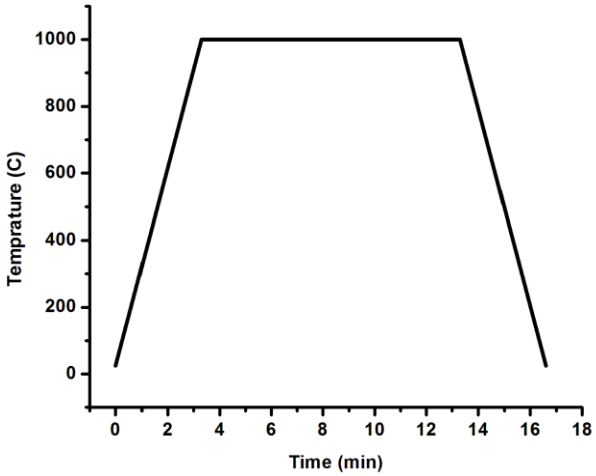

Figure 2.10. Annealing procedure of carbon films.

Heating the sputtered films on quarts causes the SC_1 to pill off from the substrate since internal stresses could not release in the highly dense carbon (Figure 2.11). This would definitely affect long term cycling of materials, therefore heated films were cycled for a limited number of cycles.

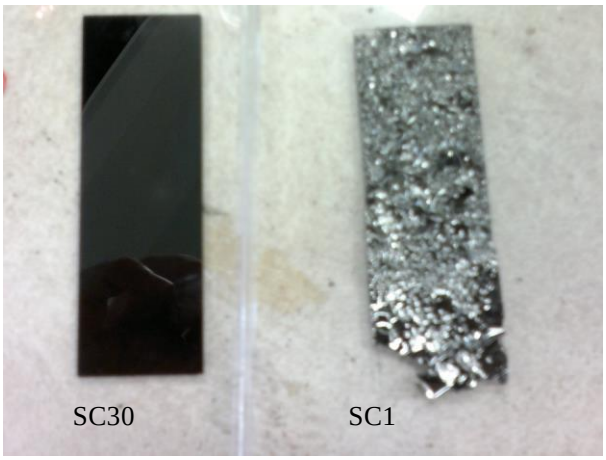

Figure 2.11. Photos of annealed carbon films sputtered on quartz substrate

Figure 2.12 shows the electrochemical behavior of the heat-treated SC_1 and SC_{30} films. Carbon and copper do not form any compounds or alloys, so the sputtered films on the copper foil discs (used directly as electrodes) were heated in a Modular Process Technology rapid thermal processor under argon to final temperatures of 700^{o}C or 900^{o}C.

Figure 2.12 shows that voltage profiles of all the films have changed dramatically after annealing. The specific capacity decreases for all samples, but the potential-capacity behavior is quite different. SC_1 heated to both 700 and 900^{o}C shows the emergence of a low voltage plateau highlighted in the inset panel of each Figure. In our opinion this may be due to some nanoporosity created when carbon atoms move to make small graphene sheets upon heat treatment of SC_1 as suggested by the results in Figures 2.7 and 2.8. Nanoporous carbons are known to exhibit such a low potential plateau [20, 21]. The right panel of Figure 2.12 shows the differential capacity curve for the as-sputtered and heated SC_1 samples. The development of the low potential plateau is clear as the temperature increase from 700 to 900^{o}C. The upper heating temperature in our experiments is limited by the melting temperature of copper (1085^{o}C).

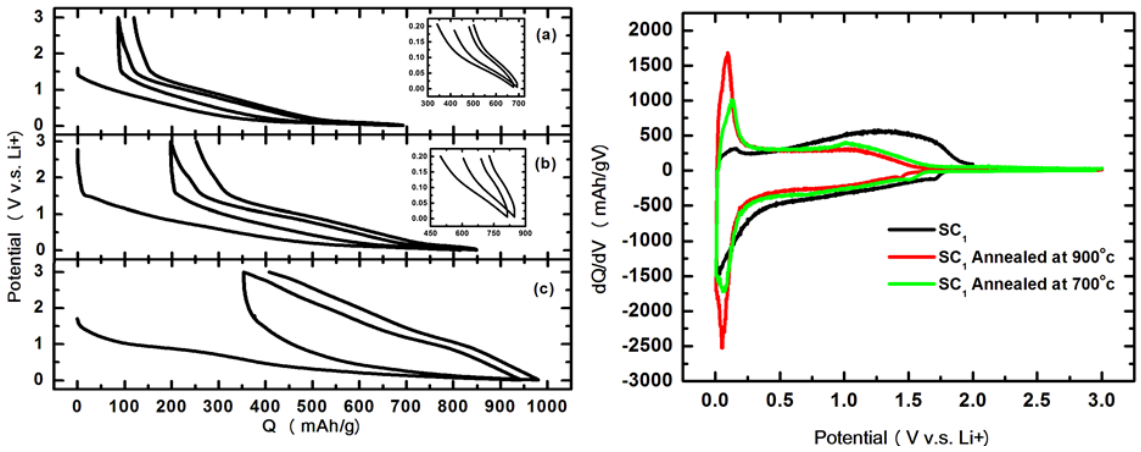

Figure 2.12. Voltage vs capacity (left panel) for first two cycles of (a) SC_1 heated to 700°C, (b) SC_1 heated to 900°C, and (c) SC_{30} heated to 900°C (The inset panels show the low voltage plateau for each figure), and the differential capacities (dQ/dV) versus cell voltage (right panel) for second cycle of SC_1 (black) as-sputtered, (green) heated to 700°C, and (red) heated to 900°C.

Figure 2.12 also shows that the behavior of sample SC_{30} changed dramatically after heating to 900°C, by comparing to the results in Figure 2.9. It is quite likely that many of the surface functional groups in as-sputtered SC_{30} were "burned-off" during the heating, but new surface groups would form upon cooling due to the porous nature of the film. These new surface functional groups were presumably different from the original ones and this could explain the differences in the voltage profiles between the as-sputtered and heated SC_{30} films.

References

1. Kasavajjula U, Wang C, Appleby AJ. Nano and bulk silicon based insertion anodes for lithium ion secondary cells. J. Power Sources 2007; 1003-39.

2. Liu XH, Zhang LQ, Zhong L, Liu Y, Zheng H, Wang JW et al. Ultrafast electrochemical lithiation of individual Si nanowire anodes. Nano Lett 2011; 11: 2251-58.

3. Obrovac M, Christensen L, Le D.B, Dahn J.R. Alloy Design for Lithium Ion Battery Anodes, J. Electrochem. Soc 2007; 154 **:** A849-A855.

4. Cui L.F, Yang Y, Hsu C.M, and Cui Y. Carbon-silicon core-shell nanowires as high capacity electrode for lithium ion batteries, Nano.Lett 2009; 9: 3370-74

5. Wu H, Chan G, Choi JW, Ryu I, Yao Y, McDowell MT, et al. Stable cycling of double-walled silicon nanotube battery anodes through solid-electrolyte interphase control. Nature Nanotech 2012; 7: 310-15.

6. Yao Y, McDowell MT, Ryu I, Wu H, Liu N, Hu L et al. Interconnected silicon hollow nanospheres for lithium-ion battery anodes with long cycle life. Nano Lett 2011; 11: 2949-54.

7. Flandrois S, Simon B. Carbon materials for lithium-ion rechargeable batteries. Carbon 1999; 37: 165-80.

8. Dahn JR, Zheng T, Liu Y, Xue JS. Mechanisms for lithium insertion in carbonaceous materials. Science 1995; 270: 590-93.

9. Xing W, Dunlap RA, Dahn JR. Studies of lithium insertion in ballmilled sugar carbon. J. Electrochem. Soc 1998; 145: 62-70.

10. Beguin F, Chevallier F, Vix C, Saadallah S, Rouzaud JN, Frackowiak E. A better understanding of the irreversible lithium insertion mechanisms in disorder carbons. J. phys. Chem. Solids 2004; 65: 211-17.

11. Xing W, Dahn JR. Study of irreversible capacities for Li insertion in hard and graphitic carbons. J. Electrochem. Soc 1997; 144: 1195-201.

12. Subramanian V et al. Low hydrogen containing amorphous carbon films-growth and electrochemical properties as lithium battery anodes. J. Power Sources 2010; 195: 2044-49.

13. Timmons A, Todd ADW, Mead SD, Carey GH, Sanderson RJ, Mar RE and Dahn JR, Studies of $Si_{1-x}C_x$ electrode materials prepared by high-energy

mechanical milling and combinatorial sputter deposition, J. Electrochem. Soc. 2007; 154: A865-74 .

14. Dahn JR, Mar RE, and Abouzeid A, Combinatorial Study of $Sn_{1-x}Co_x$ ($0 < x < 0.6$) and $[Sn_{0.55}Co_{0.45}]_{1-y}C_y$ ($0 < y < 0.5$) alloy negative electrode materials for Li-ion batteries, J. Electrochem. Soc. 2006; 153: A361-67.

15. Purcell M, et al. An investigation of C-Zn system as Li-ion battery anode materials, J. Electrochem. Soc. 2014 ; 161: A643

16. Mattox MD. Handbook of physical vapor deposition (PVD) processing. New Jersey: Noyes; 1998.

17. Ferrari AC, Robertson J. Interpretation of Raman spectra of disordered and amorphous carbon. Phys. Rev. B 2000; 61: 14095-107.

18. Ferrari AC, Robertson J. Raman spectroscopy of amorphous, nanostructured, diamond-like carbon, and nanodiamond. Phil. Trans. R. Soc. Lond. A 2004; 362: 2477-512.

19. Dresselhaus MS, Jorio A, Hofmann M, Dresselhaus G, and Saito R. Perspectives on carbon nanotubes and graphene Raman spectroscopy. Nano. Lett 2010; 10: 751-58.

20. Stevens DA, Dahn JR. The mechanisms of lithium and sodium insertion in carbon materials. J Electrochem Soc 2001;148:A803–11.

21. Nagao M, Pitteloud C, Kamiyama T, Otomo T, et al. Structure characterization and lithiation mechanism of nongraphatized carbon for lithium secondary batteries. J. Electrochem Soc 2006;153:A914–9.

CHAPTER 3

Degradation Mechanisms in Aged $LiCoO_2$/graphite Li-ion Cells

3.1 Li-ion battery degradation

The high power and energy density [1] of lithium-ion batteries make them suitable for electric vehicles, power tools and implantable biomedical devices. Applications such as electric vehicles and implantable devices need higher cycle life and longer calendar life (*more than 10 years and ideally many decades*) than portable electronics, and therefore the long-term aging of Li-ion batteries is important to understand. There are four major mechanisms for capacity loss with cycle number or time:

1. Loss of active Li-atoms that accumulate in the negative electrode solid electrolyte interphase (SEI) layer reducing cell capacity. This normally leads to impedance growth and causes capacity loss at high rates. The temperature raising accelerates the process [2 to 6]. Surface damage and graphite disordering, especially during high rate cycling, changes the SEI layer and this happens continuously eventually leading to the cell failure [4]. Carbon exfoliation could affect the SEI structure and accelerate the loss of active lithium [6].

2. Oxidation of electrolyte at the positive electrode and/or transition metal dissolution. Products of electrolyte oxidation can migrate to the negative electrode and react to produce a film of reaction products, increasing impedance, or they can perturb the negative electrode SEI. In addition, this process can lead to electrolyte consumption and cell dryout. The temperature or voltage and increase accelerates the process [7 to 9]. It has been showed by Dahn's group that electrolyte oxidation at positive electrode could have a huge negative effect on the lifetime of lithium ion batteries [8].

3. Lithium plating on the negative electrode surface can occur when cells are charged at high rates. Since Li plating has a coulombic efficiency lower than lithium intercalation in graphite, lithium plating accelerates capacity loss. Low temperature charge processes, high charging currents and capacity values close to 100% of state of charge (SOC) increase the probability of Li plating [3, 10]. In addition, cells with low SOC, show higher resistance, therefore it is essential to charge the cell in a slower rate not only at high SOC, but also at the beginning of charge (less than 10% of SOC) [10].

4. Loss of active materials from current collectors due to electrical disconnection. This is most common in cells with poorly fabricated electrodes or when physical stack pressure (due to gassing in pouch cells) is lost. Particle fracturing due to volume changes during

charge-discharge cycling may also contribute [11, 12, 13]. Electrical disconnection could cause local non-uniform charge and discharge of particles, which may lead to overcharge and overdischarge of some parts of cathode. This can rise up the internal impedance, the probability of Li plating and eventually kill the cell [11].

It is important to study Li-ion cells throughout their lifetime to be able to determine which failure mechanisms dominate so that appropriate changes to cell chemistry and cell design can be made to increase cell lifetime.

3.2 Using high precision coulometry to study degradation mechanisms in Li-ion batteries.

One way to investigate cell degradation is by measuring Coulombic efficiency (*CE*). The Coulombic efficiency of a cell can be simply defined as the ratio of the amount of charge delivered during discharge (Q_d) to the amount of charge stored during charge (Q_c):

$$CE = Q_d / Q_c \tag{3.1}$$

The Coulombic inefficiency (CIE) represents the fraction of charge lost to parasitic reactions (SEI formation, electrolyte oxidation, etc.) during a given cycle:

$$CIE = 1 - CE = 1 - Q_d / Q_c \tag{3.2}$$

Lithium-ion battery technology is a technology with CE very close to the ideal value of 1.0000 for well-made commercial Li-ion cells (where all lithium stored during charge is returned during the subsequent discharge). Standard commercially available instruments do not have the accuracy or precision to detect small changes in CE for each cycle, so cells need to be run for a long time before differences in Coulombic efficiency can be resolved at a statistically significant confidence level. The Ultra High Precision Charger (UHPC) systems at Dalhousie University (figure 3.1), have been designed to have significantly higher precision and accuracy levels than standard instruments [14, 15]. They are very useful for examining parasitic reaction rates in high quality machine-made cells with long lifetimes since they can reliably detect subtle differences in charge and discharge capacities that result from parasitic reactions in the cells. The use of the UHPC allows one to monitor the delivered charge precisely and learn about the charge consumed by those unwanted reactions and then make estimates of cell lifetime [16,17]. An important term in interpreting high precision coulometry data is charge end point

capacity. In voltage-capacity curves of Li-ion cell, the charge and discharge capacities do not exactly match due to parasitic currents, the curves shift sequentially from one cycle to the next. Generally, the more the curves slip to the right the more parasitic reactions have occurred. The amount of this shift at the top of chart is called charge end point capacity.

Figure 3.1. Photo of UHPC system at Dalhousie University

3.3 Using differential voltage analysis in understanding degradation mechanism of Li-ion batteries

Differential voltage analysis (*dV/dQ vs Q*) is a powerful tool to highlight tiny changes in the V(Q) curve of a cell during charge/discharge testing and hence to investigate the consequences of the parasitic reactions occurring inside the cell [18]. In order to understand the mechanism of cell degradation, single electrode contributions should be identify. For this reason, two half "reference" cells are prepared and preliminary analyzed: each reference cell is made by the positive or the negative materials as reference electrode vs. lithium foil as counter electrode. The voltage/specific capacity "reference" curves (q_p and q_n) enter the software to calculated full cell properties and

compared them with experimental data. In particular, the dV/dQ vs Q of the full cell can be obtained as:

$$dV/dQ = 1/m_p\,[dV_p/dQ_p] - 1/m_n[dV_n/dQ_n] \qquad (3.3)$$

where $Q_p = q_p\ m_p + \delta_p$, $Q_m = q_n\ m_n + \delta_n$, m_p and m_n are the positive and negative electrode masses in the full cell, while δ_p and δ_n are the positive and negative electrode "slippages", respectively. Slippage refers to the difference in capacity between the discharged state of the full Li-ion cell compared to the corresponding discharged state of either the positive or negative electrode. A software package was written at Dalhousie University in order to facilitate the procedure [19]. Figure 3.2 shows a screen shot of front panel of the software.

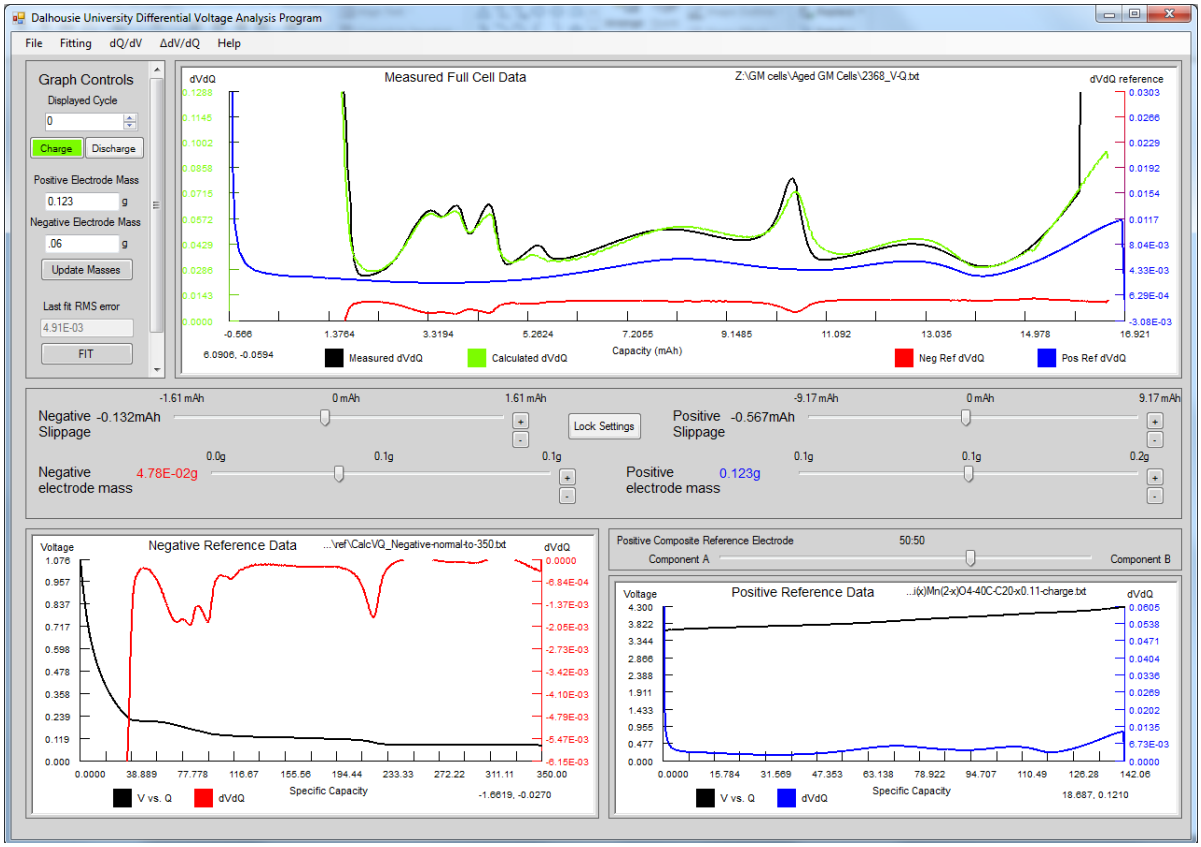

Figure 3.2. Screen shot of dV/dQ analysis software

The black curve in the upper panel of figure 3.2 is the experimental voltage measured at appropriate rate and temperature. The red curve represents the experimental data of

negative half cell, collected at same rate and temperature. The blue curve is the positive side collected again for the positive material at same rate and temperature. The software calculates the full cell data from the positive and negative half cells data that have been loaded on it. The user can easily fit the experimental full cell data by adjusting masses and slippages of reference curves derived from same electrode materials at same temperature and rate.

3.3 Study of aged $LiCoO_2$/graphite Li-ion Cells from Medtronic Inc.

Hard can prismatic Li-ion batteries were obtained from Medtronic Inc. to study aging mechanisms. These cells, comprised of $LiCoO_2$ positive electrodes and graphite negative electrodes, were delivered to Dalhousie University in five groups of four cells each with different ages and cycling history, as shown in Table 3.1. Cells in group 5 were explanted from human patients after approximately 4-6 years where the cycling regime is not well known. Only the highest possible upper cut-off voltage (4.075 V) and the lowest possible cut-off voltage (3.4 V) are known. Further details are given in the caption to Table 3.1.

Table 3.1. Descriptions of $LiCoO_2$/graphite received from the manufacturer. The cells tested under controlled conditions were charged and discharged between 3.4 V and 4.075 V at 37°C. The charge current was C/6 and the discharge was either C/24 or C/150 as indicated in the table below. The implanted cells were kept between the same potential limits and were also at 37°C (except for possibly brief periods of fever or hypothermia). The charging frequency and the state of charge at the end of charge or discharge for the implanted cells was controlled by the user and is not known.

Group-test protocol	Number of cells	Number of cycles	Years under test (years)	Years on shelf (years)	Total age (years)
G_1-fresh	4	~ 0	~ 0	~ 0.4	0.4
G_2-daily test (C/6 charge, C/24 discharge)	4	~ 500	~ 1.75	~ 1.35	3.1
G_3-weekly test (C/6 charge, C/150 discharge)	4	~ 435	~ 7.3	~ 0.6	7.9
G_4-weekly test (C/6 charge, C/150 discharge)	4	~ 700	~ 11.4	~ 0.5	11.9
G_5- post-Explant	4	N.A.	~ 6.5 (implanted)	~ 1.6	8.1

The electrolyte in these cells used $LiPF_6$ salt, a combination of carbonate solvents and one or more undisclosed electrolyte additives.

3.3.1 Experimental procedure at Dalhousie University

All the aged cells were cycled at Dalhousie University using the UHPC at C/20 and C/50 rates for the CE measurements and dV/dQ analysis, respectively. Cycling for all the cells has been done at 40 ± 0.1ºC between 3.4 and 4.075 V. The UHPC system at Dalhousie University is able to measure the CE of cells cycled at rates of C/20 with an accuracy of ±0.003%. Impedance spectra were collected after the UHPC cycling at 10ºC using a Biologic VMP3 battery tester equipped with an EIS board. EIS experiments were performed at 3.9 V over a frequency range of 100KHz to 50mHz. The EIS tests were performed at 10ºC to amplify the differences between the cells.

Reference curves for the electrodes in the cells were generated by cycling each electrode (obtained fresh from the manufacturer) separately in a 2325 coin-type cell vs lithium metal at a C/50 rate and 40 ± 0.1ºC. Each coin cell was assembled using a disk punched from electrode sample, two Celgard 2300 separators, and a lithium foil disk. The electrolyte in the coin cells was 1 M LiPF6 in ethylene carbonate: ethyl methyl carbonate (EC:EMC) 3:7 (by weight).

Several other similar $LiCoO_2$/graphite cells were obtained from Medtronic Inc. for studies of the impact of the upper voltage cutoff during long term testing at 55ºC. These cells used 1M $LiPF_6$ dissolved in EC:EMC (3:7 by volume) as the baseline electrolyte. Some cells had 0.3 wt% trimethoxyboroxine (TMOBX, obtained from BASF) added to the electrolyte while others had 2% vinylene carbonate (VC, obtained from Novolyte technologies, now BASF) and 0.3% TMOBX added to the electrolyte. These cells were cycled using a Maccor Series 2000 cycler, some between 3.4 and 4.075V while the rest were cycled between 3.4 and 4.175V.

3.3.2 Cycling history of aged $LiCoO_2$/graphite Li-ion Cells

Figure 3.3 shows discharge capacity vs. cycle number for cells from groups 2, 3, and 4 during their cycle testing at Medtronic Inc. before the UHPC testing at Dalhousie University. Testing protocols for these groups were different: group 2 (G_2) was tested using a "daily test" protocol, which consists of a ~ C/6 charge followed by a ~ C/24 discharge. The cycling rates for G_3 and G_4 cells were ~ C/6 and ~ C/150 for charge and

discharge, respectively, referred to as "weekly tests". The average discharge capacity losses for cells in groups G_2, G_3 and G_4 were ~12.3%, ~19.5% and ~21% of initial capacity after ~500, ~435, and ~700 cycles respectively.

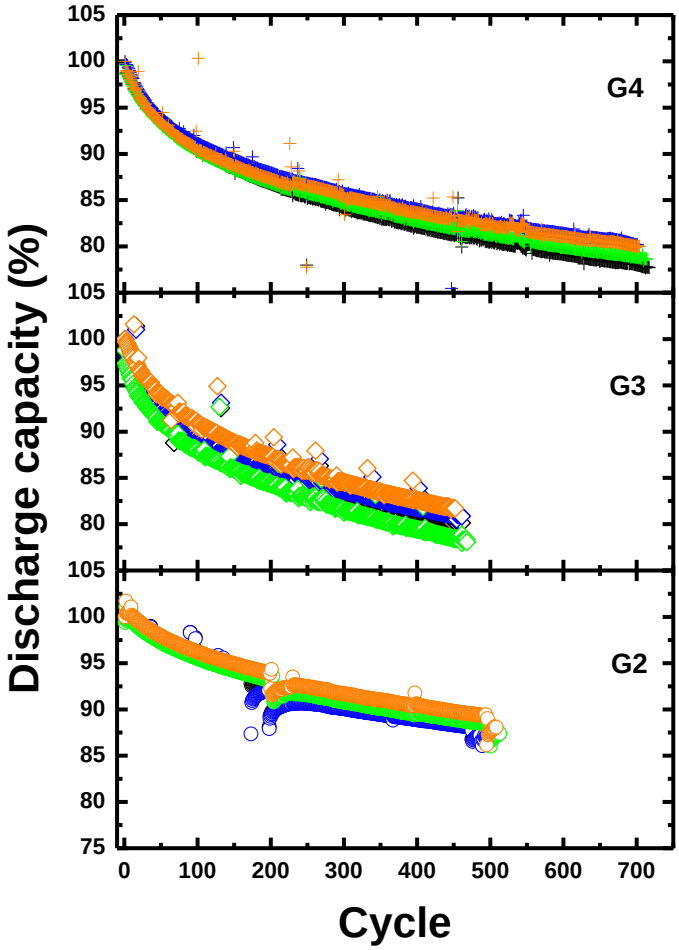

Figure 3.3. Discharge capacity versus cycle number for LCO/graphite cell groups G_2 (~3 years old), G_3 (~ 7.7 years old), and G_4 (~ 11.7 years old), provided by the manufacturer. The testing was carried out as described in Table 1.1.

The capacity loss for groups G_3 and G_4 are very similar even though G_4 is ~4 years older than G_3 and has been cycled an additional ~250 cycles. This suggests that the SEI layer on the negative electrode has become mature and stable so that capacity loss between 8 and 12 years of cycling is minimal.

3.3.3 Fitting of data using SEI growth law

Figure 3.4 (top panel) shows the fractional discharge capacity data **versus time** for two cells from each group. Curves for each of the three groups have been fit (see the solid green lines in Figure 2, top panel) using the expression:

$$q(t) = 1 - A\, t^{1/2} \qquad (3.4)$$

where q(t) is the fractional capacity and A is a fitting parameter which has units of $yr^{-1/2}$. The values of A which gave the best fit to the data are given in Table 2. The $t^{1/2}$ law given in equation 3 is characteristic of capacity loss due to SEI growth on the negative electrode where the fade rate slows down as the SEI film thickens with time following the parabolic growth law [5, 20].

Table 3.2. Parameter, A, in the fit to the capacity versus time curves in Figure 3.4 using the equation $Q(t) = Q_o (1 - A\, t^{½})$

Cell group	Value of A ($yr^{-1/2}$)
G_2 - fresh	0.093
G_3 – weekly life test	0.078
G_4 – weekly life test	0.068

Although fits in Figure 3.4 are not perfect, they do describe the data fairly well. The data for group G_2 clearly fades more rapidly than groups G_3 and G_4, as reflected by the larger value of A needed to fit the data. This may be caused by a greater number of cycles during the same time for the group G_2 cells, possibly leading to more expansions and contractions of the graphite particles and more rapid SEI growth. This is discussed in more detail with the dV/dQ analysis later in the chapter.

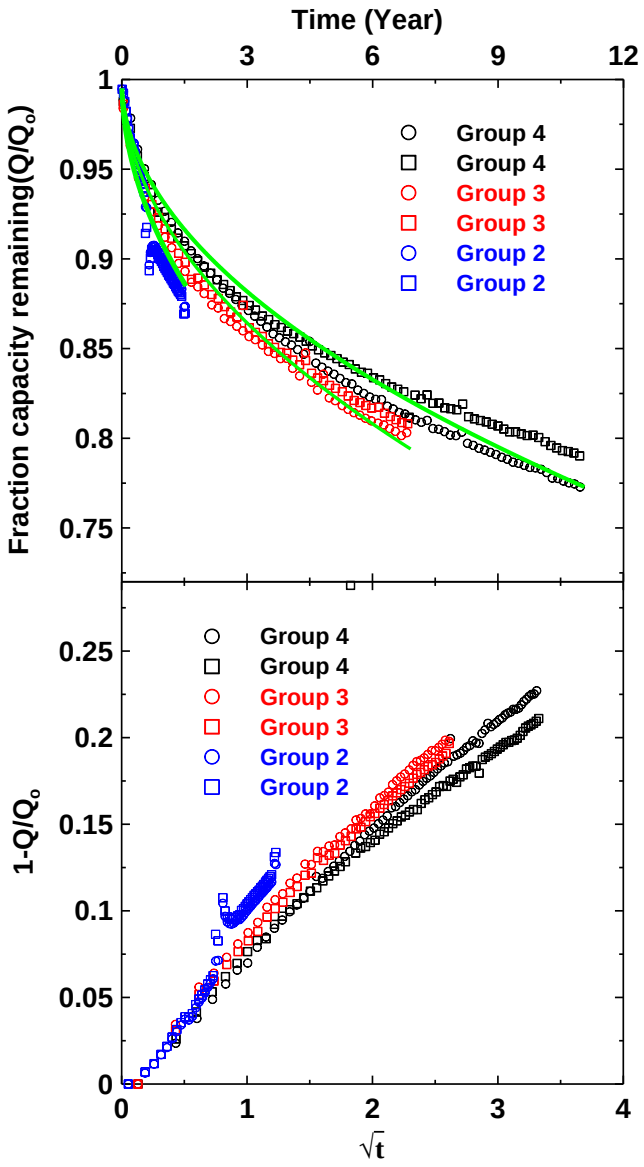

Figure 3.4. Fractional discharge capacity versus testing time (top panel) and fractional capacity loss versus $(t)^{1/2}$ (bottom panel) for LCO/graphite cell groups G_2 (~3 years old), G_3 (~ 7.7 years old), and G_4 (~ 11.7 years old), provided by the manufacturer. The solid curves are fits to the data using equation (3.4) and the values of A used are listed in Table 3.2.

On the other hand, as mentioned in Table.1.1, these cells have shelf age (before and/or after testing) of 1.35, 0.6, and 0.5 years for G_2, G_3, and G_4 respectively. The temperature was uncontrolled during these time and this could explain why these cell do not follow same capacity fade profile. Figure 3.4 bottom panel shows fractional capacity loss versus $(t)^{1/2}$, as it shows, fractional capacity loss for G_2, G_3, and G_4 are align on almost straight line versus $(t)^{1/2}$ which suggest that data is following parabolic growth low.

3.3.4 UHPC cycling

Figure 3.5 shows cycling data measured by UHPC, collected after the cycling shown in Figures 3.1 and 3.2, at a rate of C/20 at 40ºC including charge endpoint capacity (top panels), discharge capacity (middle panels) and coulombic efficiency (bottom panels).

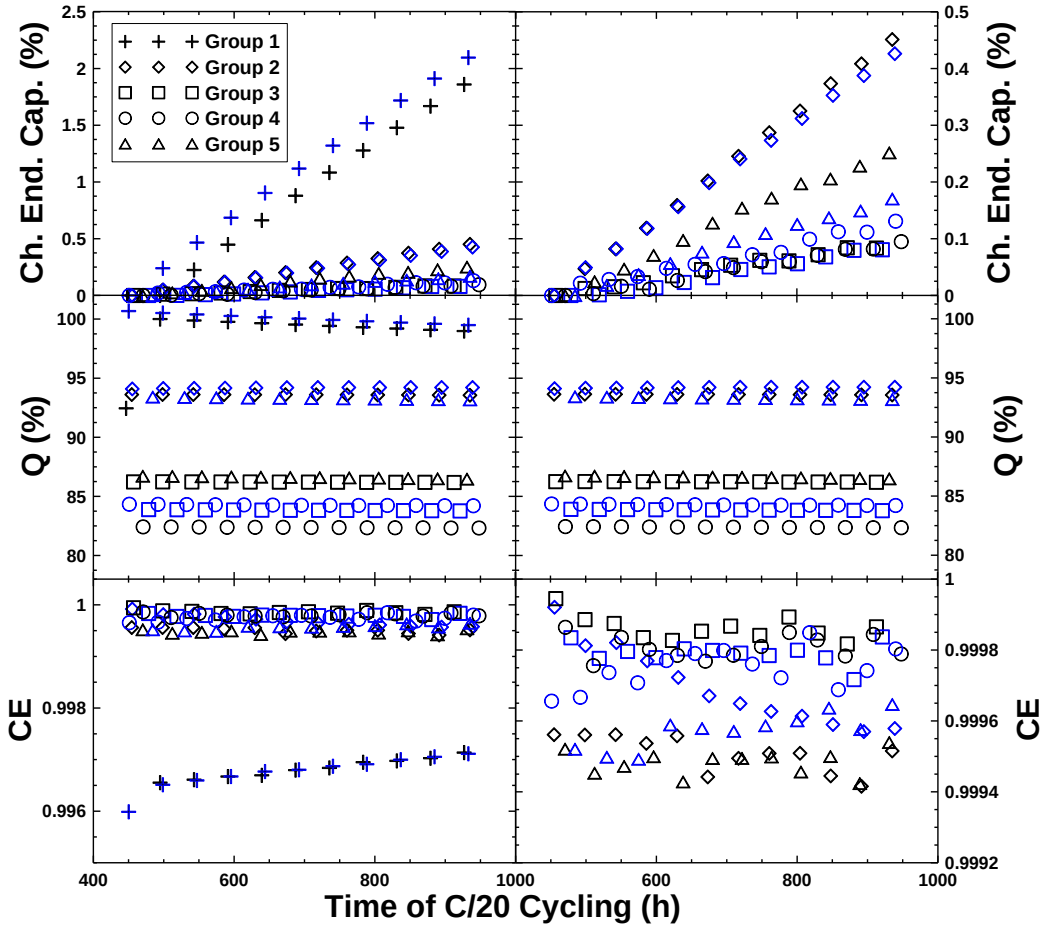

Figure 3.5. Charge endpoint capacity (top panels), discharge capacity (middle panels), and colombic efficiency (bottom panel) plotted versus time during C/20 (40.0ºC) charge-discharge cycling at Dalhousie University on the UHPC for a pair of cells (blue and black) from each group as indicated.

The right panels show the same data as the left panel except on an expanded scale for coulombic efficiency and charge endpoint capacity so the small differences between cells in groups G_3. G_4 and G_5 can be better observed.

Monitoring capacity loss along with accurate measurements of CE and charge endpoint capacity slippage is an effective way to learn about parasitic reactions in the cells. Obviously, less capacity loss indicates better performance of cell, but it does not give complete information about parasitic reaction rates. Cells with CE closer to 1.0000 and

smaller endpoint slippage rates have a lower rate of parasitic reactions and therefore should have a longer life time. Figure 3.5 shows that the CE increases as cells get older. In addition to increased CE for aged cells, the charge endpoint capacity slippage slows down indicating a lower rate of oxidation reactions at the positive electrode [21]. The upper left panel of Figure 3.5 shows that fresh cells (G_1) have a much higher charge endpoint slippage compared to all the aged cells. The upper right panel of Figure 3.5 shows that G_5 cells have noticeably higher slippage rates than G_3 cells, even though they are at same age. In the human implant condition (G_5) recharge sessions were carried out by the end-user. While the upper cut-off voltage is bounded by the device design at 4.075 V, a distribution of recharge habits, including number of charge sessions and early cessation of charging is likely. The greater slippage for G5 cell is consistent with these cells not having been charged to 4.075 V as often, thus slowing the formation of protective films at the positive electrode. This correlates well with their lower CE shown in the lower panels of Fig. 3.5. Groups G_3 and G_4 have almost the same charge endpoint slippage and CE indicating that there is only a small difference in passivation, and thus parasitic reaction rate, between the ages of ~8 and ~12 years for these cells.

Figure 3.6 shows the average values for CE (calculated from an average of the last 5 data points) and charge endpoint capacity slippage rate (calculated from the slope of the slippage versus time curves) versus cell age. Generally speaking, charge endpoint slippage decreases and CE increases as cell age increases. This suggests that parasitic reaction rates decrease as cell age increases but since the CE never reaches 1.0000 and the charge slippage never reaches zero, parasitic reactions are still occurring in these cells. Post-implant cells, shown with red data points, do not follow the trend of lower reaction rates with increased cell age. The group G_5 cells show a CE very similar to group G_2 and a charge endpoint capacity slippage rate slightly higher than group G_3. Therefore, one can say that group G_5 cells have an effective 'cell age' close to group G_2 cells even though they are nominally older. This is very good news for the application of these cells as their field performance should be more favorable than that predicted by laboratory, cycle testing.

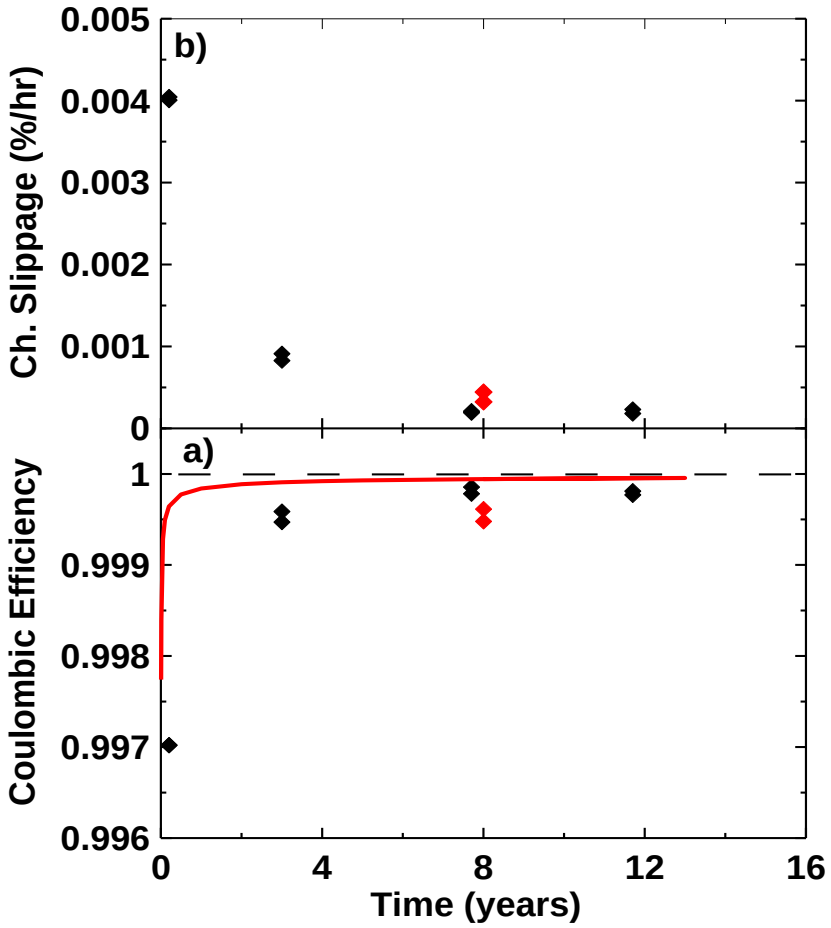

Figure 3.6. Average data over last five cycles for pairs of cells from each group. (a) CE versus age, (b) charge endpoint capacity slippage versus age. The data was extracted from Figure 3. The solid red curve is the prediction of equation (4) with A = 0.08 $(yr)^{-1/2}$.

The good fits to the data in Figure 3.4 using a parabolic growth model for the negative electrode SEI allow one to estimate what the CE of the cells would be **if only SEI growth** at the negative electrode were occurring and **no electrolyte oxidation** at the positive electrode were occurring. The expected CE under these conditions can be derived from Equation 3.5 and is:

$$CE(t) = 1 - [A\, t^{-1/2}\, t_o] \qquad (3.5)$$

where t_o is the initial time of a discharge (in years). The red curve in Figure 4a has been calculated for A = 0.08 $yr^{-1/2}$ (see fits to Figure 3.4) and t_o = 0.00228 yr (20 hours), which corresponds to the conditions in this study. The departure of the data in Figure 3.6.a from the red curve, and the non-zero charge endpoint capacity slippage rate in Figure 3.6.b,

indicate that some (albeit exceedingly low) electrolyte oxidation in these cells is occurring even after 12 years of testing.

Reference 21 considers how coulombic efficiency, charge endpoint capacity slippage and capacity fade should be related. Equations 11 – 14 in that paper can be rewritten (in the case where there is no positive electrode damage and no reduction of salt concentration in the electrolye) as:

$$1 - CE = f/Q + \Delta_c/Q \quad (3.6)$$

where f is capacity loss per cycle (in mAh/cycle), Δ_c is the charge endpoint capacity slippage per cycle (in mAh/cycle) and Q is the cell capacity (in mAh). Table 3.3 compares 1- CE, f/Q and Δ_c/Q for the UHPC measurements on all cells in groups G_1 to G_5. In addition, Table 3.3 compares the capacity fade rates measured in the final 50 cycles of testing at Medtronic (37^{o}C) and in the testing at Dalhousie (40^{o}C) in %/year for groups G_2, G_3 and G_4. The capacity fade rates are extremely small and differences in the testing conditions (temperatures, rates) could be responsible for the difference between the Dalhousie and Medtronic values.

The last three columns of Table 3.3 show that equation (3.6) is satisfied, in general, to within the error of the UHPC measurements. The accuracy and precision of the UHPC equipment in the units of Table 3.3 are ±0.00003 per cycle and ±0.00001 per cycle, respectively, as indicated in reference 15. Table 3.3 shows that electrolyte oxidation, as evidenced by charge endpoint capacity slippage, contributes about 50% to the departure of the CE from 1.00000 for the group G_3, G_4 and G_5 cells. Traditional measurements of capacity versus cycle number during long term cycling do not capture this important parasitic process which is occurring in cells and which consumes electrolyte.

Table 3.3. Summary of long term cycle testing and ultra-high precision charger (UHPC) testing for the group G_1 to group G_5 cells. Only two cells from each group were tested on the UHPC.

Group	cell	Fade at end of long term test %/yr	Fade during UHPC test %/yr	Fade during UHPC test fraction/cycle	Charge slippage rate fraction/cycle	1 - CE
1	1	N/A	N/A	N/A	N/A	N/A
1	2	N/A	N/A	N/A	N/A	N/A
1	3	N/A	19.81	0.001082	0.00189	0.00298
1	4	N/A	19.84	0.00109	0.00194	0.00298
2	1	3.39	N/A	N/A	N/A	N/A
2	2	3.44	N/A	N/A	N/A	N/A
2	3	3.33	1.50	0.00007	0.00037	0.00053
2	4	3.23	-0.09	-0.000004	0.00033	0.00041
3	1	1.03	N/A	N/A	N/A	N/A
3	2	1.11	N/A	N/A	N/A	N/A
3	3	1.31	1.21	0.00006	0.00008	0.00014
3	4	1.20	2.17	0.00011	0.00008	0.00022
4	1	0.78	N/A	N/A	N/A	N/A
4	2	0.73	N/A	N/A	N/A	N/A
4	3	0.74	1.68	0.00008	0.00009	0.00023
4	4	0.67	1.73	0.00007	0.00007	0.00019
5	1	N/A	N/A	N/A	N/A	N/A
5	2	N/A	N/A	N/A	N/A	N/A
5	3	N/A	4.35	0.00022	0.00015	0.00038
5	4	N/A	5.59	0.00027	0.00020	0.00052

3.3.5 Impedance spectroscopy measurement

Figure 3.7 shows electrochemical impedance spectroscopy (EIS) data collected at 10ºC at 3.90 V for two cells from each group after the UHPC testing. Generally speaking, the cell impedance increases as cell age increases [22]. Based on previous EIS work on similar cells [23, 24], the low frequency semicircle originates from the positive electrode and it is the impedance of the positive electrode that increases most dramatically for cells in groups G_3 and G_4. This is consistent with persistent electrolyte oxidation occurring in these cells [23, 24]. Cells from group G_5 have significantly lower impedance than cells from group G_3, even though they have the same calendar age. At high state of charges (SOC), the positive electrode is at a higher potential which increases the rate of parasitic

reactions leading to impedance growth [25]. This again agrees well with the assumption that the implanted cells spend most of their time at lower SOC.

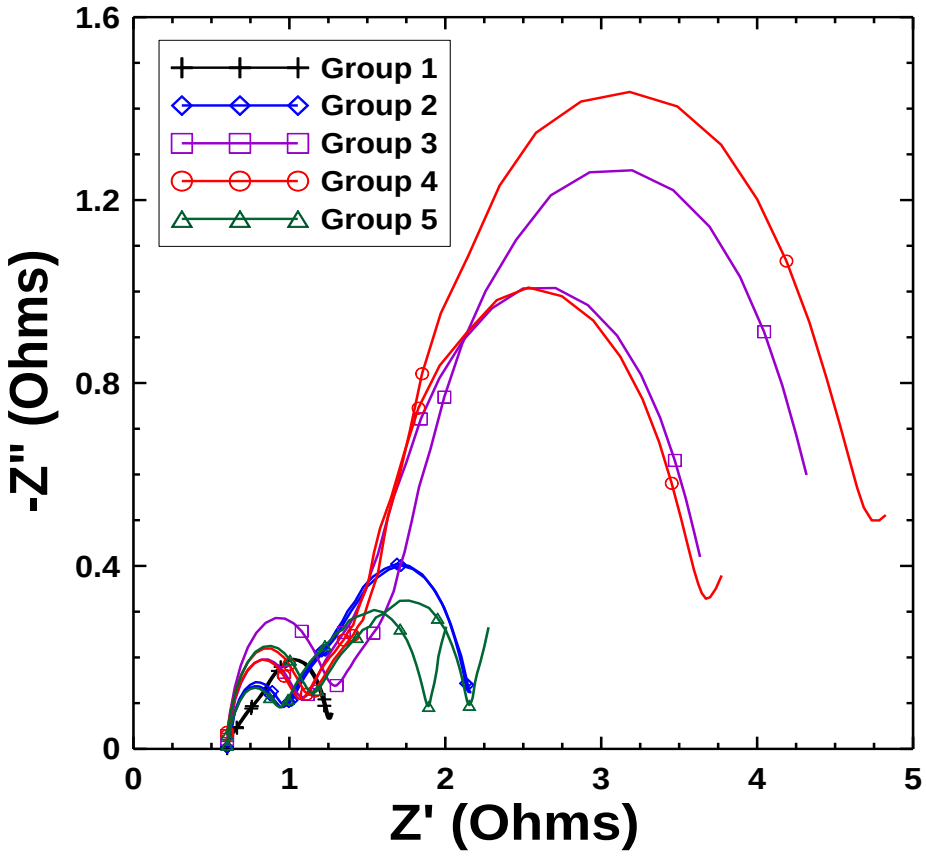

Figure 3.7. Impedance spectra of a pair of cells from each group at 3.9 V and 10ºC after the UHPC cycling tests.

3.3.6 Differential voltage analysis

It is important to verify that the capacity loss with cycle number or with time displayed in Figures 3.3 and 3.4 is not caused by loss of active mass, even though the fit to the data in Figure 3.4 using equation 3.4 suggests there is little, if any, loss of active mass. Figure 3.8 shows differential voltage analysis for a representative cell from each group. The black curves are the experimental data (collected on the UHPC at a C/50 rate and at 40ºC) and the red curves are calculated data from Equation 3.3. The dV/dQ vs Q fitting strategy adopted was to fix the positive electrode mass to be equal to that on the cell build sheets from the manufacturer and then let the dV/dQ program determine the relative slippage between the positive and negative electrodes and the negative electrode mass that give the best fit. The calculated dV/dQ vs. Q curves match the experimental curves quite nicely for all cells, especially for groups G_1 and G_5.

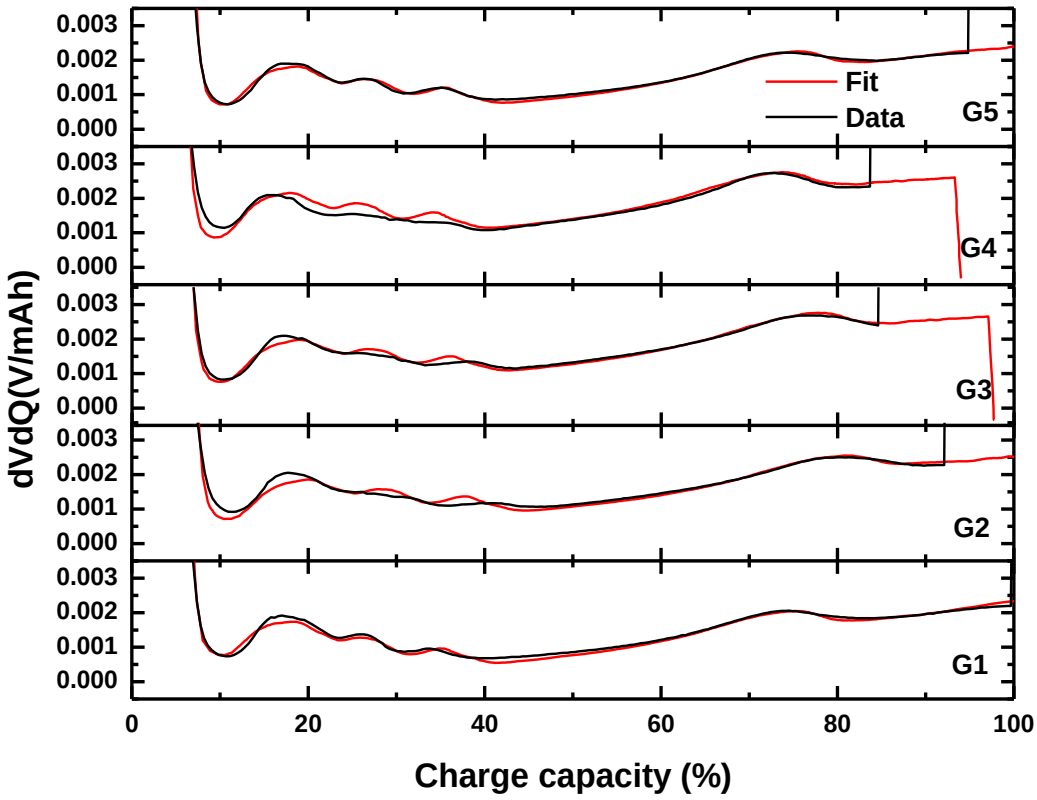

Figure 3.8. Differential voltage analysis (dV/dQ vs.Q) for a representative cell from each group as indicated. Charge cycles at C/50 rate were selected to fit using reference curves generated from the same electrode materials as used in the cells.

The fits of the data for groups G_2, G_3 and G_4 is not as good, in particular for peaks that originate from the graphite electrode at relatively low SOC. This could be due to turbostratic disorder of some adjacent graphene sheets occurring during long term cycling due to stress/strain caused by intercalation. The presence of turbostratic disorder has been shown to cause subtle changes in the differential capacity versus potential of the graphite electrode [26].

Figure 3.9 shows the potential vs. capacity curves of both negative and positive electrodes (vs. Li/Li^+) derived from the dV/dQ software as well as the experimental full cell V(Q) curves for those cells shown in Figure 3.8. The potential of the positive electrode and voltage of the experimental full cell are shown at left axis of Figure 3.8 while the potential of the negative electrode is shown on the right axis. The negative electrode mass and both the negative and positive electrode slippages are those that provided the best fit to the experimental data.

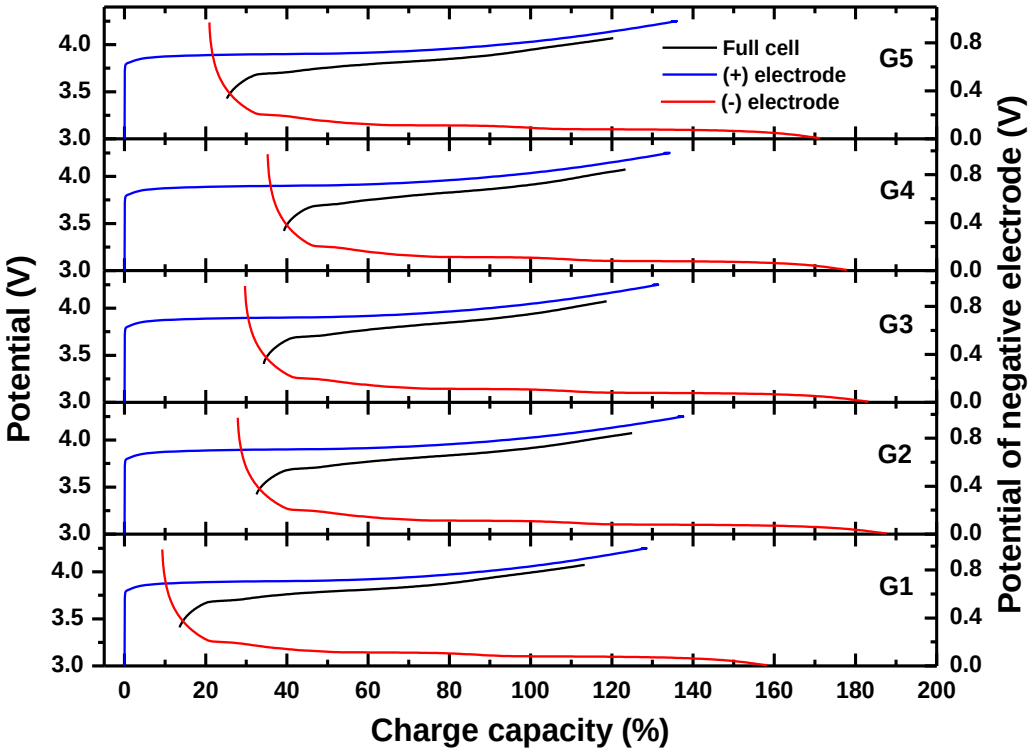

Figure 3.9. Voltage versus capacity for charge cycles at C/50 rate of group G_1 to group G_5 cells shown in Figure 6. The potential versus capacity of the positive (blue) and negative electrodes (red) vs. Li/Li^+ as determined from dV/dQ analysis in Figure 6 are also shown. The black curve is the experimental full cell voltage curve. All curves have been offset so the fully lithiated positive electrode is at Q = 0.

For all cells, the negative electrode slips to higher capacity with respect to the positive electrode compared to the fresh, group G_1, cells. This is due to the lithium atoms consumed to increase the SEI layer thickness at the negative electrode. The negative electrode slippage is greater in the older group G_3 and group G_4 cells compared to the younger cells. The post-implanted group G_5 cells show a negative electrode slippage close to that of the group G_2 cells suggesting that their apparent age is less than their calendar age, in agreement with the results from UHPC testing.

Figure 3.10 shows the relative electrode slippage vs. calendar age of all the cells. Relative electrode slippage is defined here as the difference between the capacity at which the positive electrode is fully lithiated and the negative electrode is fully delithiated. This is derived from the fitted experimental data for all cells, and shows that the relative slippage for implanted cells in some cases is even less than that of the 3 years old cells. The vertical error bars are due to different fitting strategies that were applied to probe the reliability of the dV/dQ analysis.

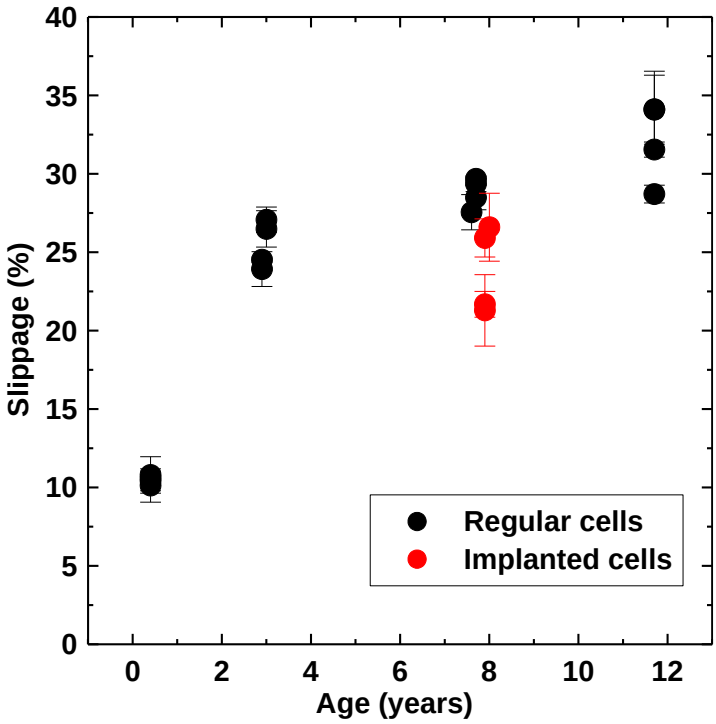

Figure 3.10. Relative slippage (discharge slippage minus charge slippage) versus age for all the group G_1 to G_5 cells as determined using the differential voltage analysis software. Post-implanted cells (group G_5) are shown with red data points as indicated.

Figure 3.11 shows the change in active mass compared to that of the as-built cells of the negative electrode for all cells. The initial active mass of the negative electrodes was provided by the manufacturer and the final mass was obtained from dV/dQ analysis. A negative value means that the negative electrode has lost active mass and a positive value is likely due to error in fitting the differential voltage curves. There is negligible loss of negative electrode active mass for all cells except for the group G_4 cells where some cells could have as much as 5% of negative electrode active mass loss. It should be emphasized that an active mass loss of only 5% is quite impressive for a 12 year old cell.

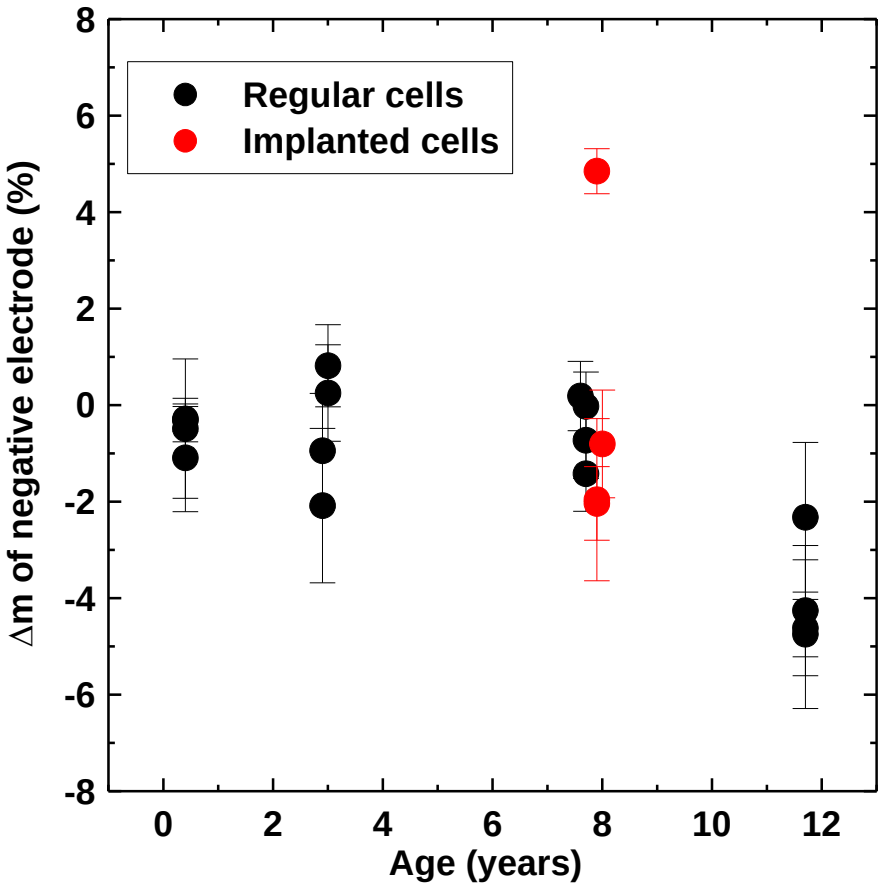

Figure 3.11. Change in active mass of the negative electrode (%) calculated using differential voltage analysis software versus cell age for all 20 cells. Post-implanted cells (group G_5) are shown with red data points as indicated.

Figure 3.12 shows relative electrode slippage vs. capacity loss for all the cells during their respective long-term cycling periods. The horizontal error bars on the implanted cells are due to the fact that initial capacities for these cells are not available and the average of the initial capacities of the Group G_1 – G_4 cells was used for the initial capacity of all the group G_5 cells. Figure 3.12 shows that the capacity loss (Figure 3.3) and the relative slippages from the dV/dQ analysis are well correlated. The slope of the linear fit, shown with a red dashed line, is almost exactly 1.0 suggesting that negligible active material loss is occurring in these cells and thus that essentially all capacity loss can be attributed to parasitic reactions, in particular those that lead to consumption of active Li atoms in the negative electrode SEI which causes relative electrode slippage.

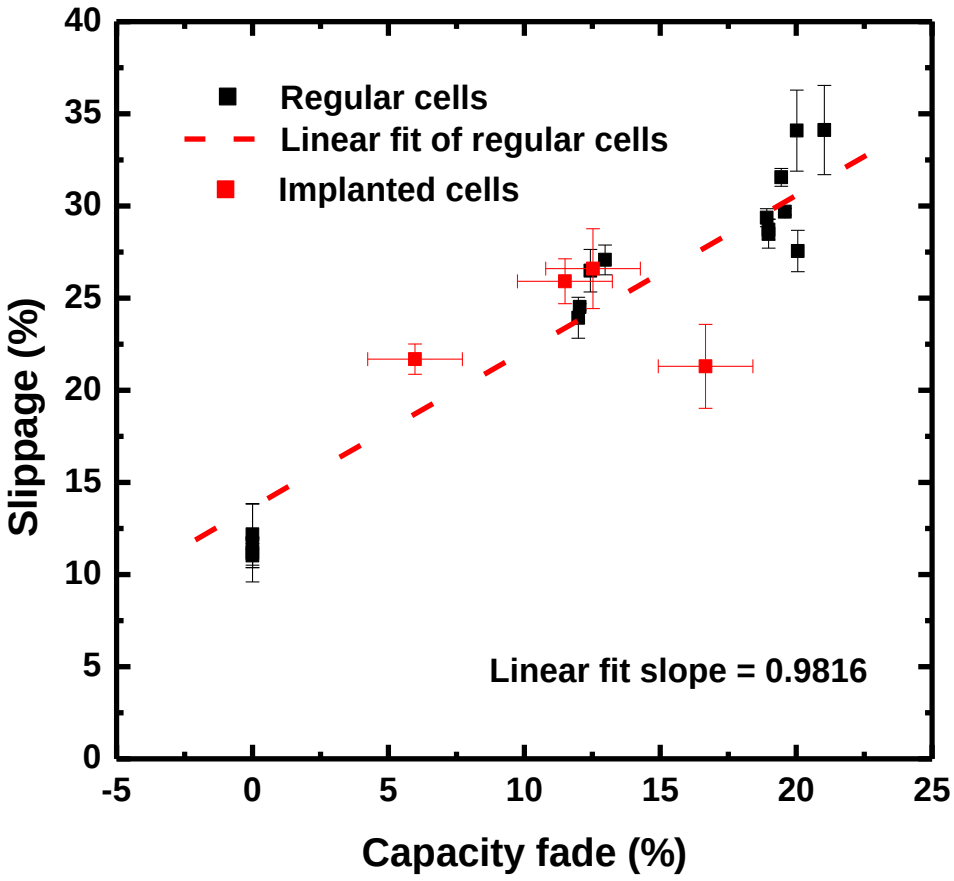

Figure 3.12. Relative slippage for all 20 cells as determined from differential voltage analysis software versus capacity loss during long-term cycling at the manufacturer. Post-implant cells (group G_5) are shown with red data points. A linear fit to the data is shown by the red dashed line.

This means that reducing parasitic losses at the electrodes due to electrolyte/electrode reactions will improve the lifetime of these cells. The data for the 8-year old implanted cells (group G_5), in red, cluster around the results for the 3 year old G_2 cells. This suggests that the upper cut-off voltage plays crucial role in the lifetime of these cells.

A higher upper cut-off voltage has minimal impact on the potential of the negative electrode, so oxidized species created at the positive electrode must migrate to the negative electrode and perturb the SEI forming reactions. Limiting the formation of such species is the best strategy for improving the lifetime of these cells and short-term measurements of coulombic efficiency and charge endpoint capacity slippage can be used to detect when changes to cell chemistry make a positive impact [27].

Figure 3.13 shows the capacity versus cycle number for similar style $LiCoO_2$/graphite cells tested to different upper cut-off voltages at a C/10 rate at 55ºC for over two years. Data is shown for two different electrolyte additive combinations studied in a previous experiment [27]. The circles show data for cells with mixture of trimethoxyboroxine ($C_3H_9B_3O_6$ - *referred to here as TMOBX*) and vinylene carbonate (*VC*), while the squares show data for cells with only TMOBX as an additive.

Data in the upper panel are for cells that were charged to a higher upper cut-off voltage (*4.175 V - HVC*) and those in the bottom panel are for cells that were charged to a lower upper cut-off voltage (*4.075 - LVC*). All four cells show typical capacity fade according to the parabolic SEI growth law for about the first 400 cycles regardless of upper cut-off voltage. However, at cycle 400 the HVC cell containing only TMOBX begins to fade more rapidly while the LVC cell continues cycling with minimal capacity loss. The same is seen for the VC + TMOBX-containing cells where at cycle 600 the HVC cell begins to fail more rapidly while the LVC cell continues to cycle well. It is unclear at this time how much longer the LVC cells will cycle but it is clear that the small difference of 100 mV in upper cut-off voltage has a major impact on cycle and calendar life.

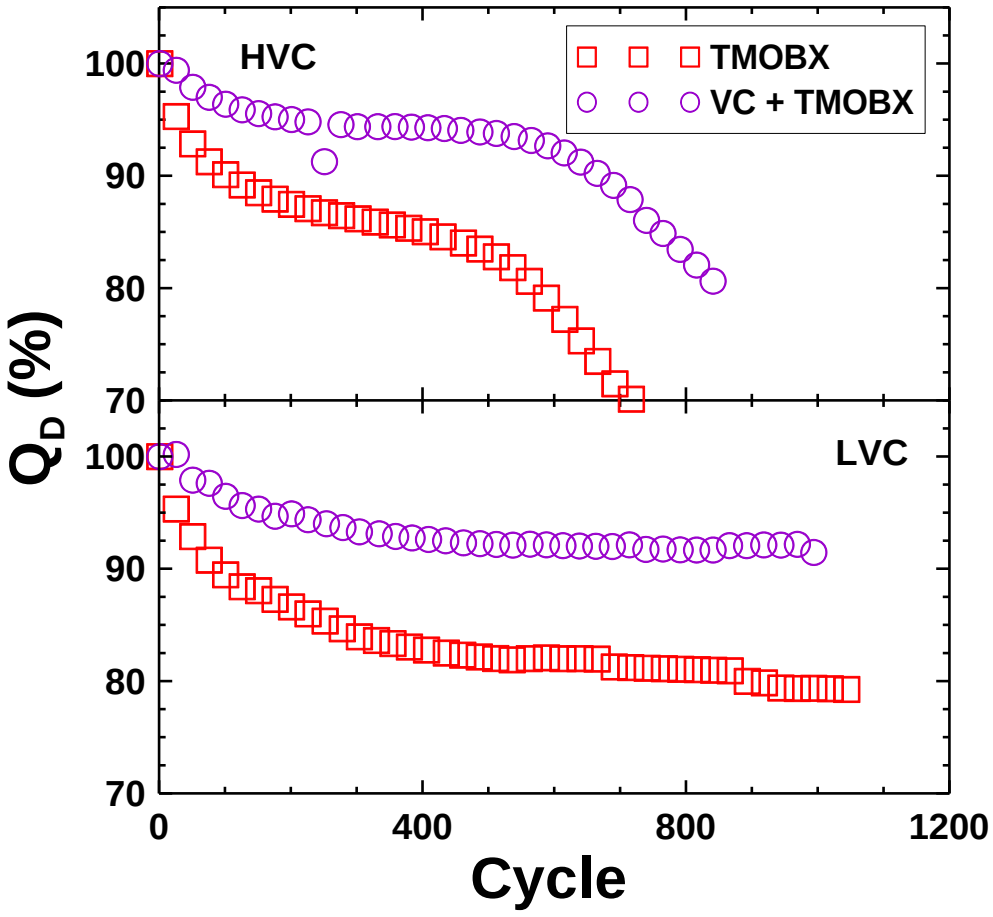

Figure 3.13. Cycling data at a C/10 rate and 55ºC for 4 cells with same electrode chemistry as the 20 aged cells also obtained from Medtronic Inc. Two cells were cycled between 3.4 V and 4.175 V (HVC) and two were cycled between 3.4 V and 4.075 V (LVC). The electrolyte additives used are indicated in the legend. The testing has continued for more than 2 years for the LVC cells.

This strongly suggests that electrolyte oxidation at positive electrode is a major side reaction affecting the lifetime of these cells, and the effect of using electrolyte additives to improve cycle life is clearly seen as the cell containing VC + TMOBX shows better cycling performance than the cell containing only VC regardless of which upper cut-off voltage is chosen. As a side note, this behaviour is completely predictable based on the short term high precision coulometry results presented on the same cells when they were fresh some years ago [23]. These results support the hypothesis that the reason the implanted group G_5 cells have a smaller "effective age" than the group G_3 and group G_4 cells is because the group G_5 cells did not experience high states of charge as often.

References

1. J.M. Tarascon, M. Armand, Nature., 44, 359 (2001).
2. M. Broussely, S. Herreyre, P. Biensan, P. Kasztejna, K. Nechev, R.J. Staniewicz, J. Power Sources., 97, 13 (2001).
3. J. Vetter et al., J. Power Sources., 147, 269 (2005).
4. L. J. Hardwick, M. Marcinek, L. Beer, J. B. Kerr, and R. Kostecki, J. Electrochem. Soc., 155, A442 (2008).
5. A. J. Smith, J. C. Burns, Xuemei Zhao, Deijun Xiong, and J. R. Dahn, J. Electrochem. Soc., 158, A447 (2011).
6. P. Liu et al., J. Electrochem. Soc., 157, A499 (2010).
7. M. Wohlfahrt-Mehrens, C. Vogler, and J. Garche, J. Power Sources., 127, 58 (2004).
8. A. J. Smith, N. N. Sinha, and J. R. Dahn, J. Electrochem. Soc., 160, A235 (2013).
9. D. Lu, M. Xu, L. Zhou, A. Garsuch, and B. L. Lucht, J. Electrochem. Soc., 160, A3138 (2013).
10. S.S. Zhang, J. Power Source., 161, 1385 (2006).
11. R. Kostecki, J. Lei, F. McLarnon, J. Shim, and K. Striebel, J. Electrochem. Soc., 153, A669 (2006).
12. M. Dubarry et al., J. Power Sources., 196, 10336 (2011).
13. M. Dubarry et al., J. Power Sources., 196, 3420 (2011).
14. A. J. Smith, J. C. Burns, S. Trussler, and J. R. Dahn, *J. Electrochem. Soc.*, 157, A196–A202 (2010).
15. T. M. Bond, J. C. Burns, D. A. Stevens, H. M. Dahn, and J. R. Dahn, *J. Electrochem. Soc.*, 160, A521–A527 (2013)
16. A. J. Smith, J. C. Burns, and J. R. Dahn, J. Electrochem. Soc., 13, A177 (2010).
17. J.C. Burns, A.Kassam, N.N. Sinha, L.E. Downie, L. Solnickova, B.M. Way, and J.R. Dahn, J Electrochem. Soc., 160, A1451 (2013).
18. I. Bloom, A. N. Jansen, D. P. Abraham, J. Knuth, S. A. Jones, V. S. Battaglia, G. L. Henriksen, J. Power. Sources., 139, 295 (2005).
19. Hannah M. Dahn, A. J. Smith, J. C. Burns, D. A. Stevens, and J. R. Dahn, J. Electrochem. Soc, 159, A1405 (2012).
20. Q. Zhang and R.E. White, J. Power Sources., 179, 793 (2008).

21. A.J. Smith, J. C. Burns, D. Xiong, and J.R. Dahn, J Electrochem. Soc., 158, A1136 (2011)
22. A. Barre, B. Deguilhem, S. Grolleau, M. Gerard, F. Suard, and D. Riu, J. Power. Sources., 241, 680 (2013).
23. R. Petibon, N.N. Sinha, J.C. Burns, C.P. Aiken, Hui Ye, Collette M. VanElzen, Gaurav Jain, S. Trussler and J.R. Dahn, Journal of Power Sources, **251**, 187 (2014)
24. R. Petibon, C.P. Aiken, N.N. Sinha, J.C. Burns, Hui Ye, Collette M. VanElzen, Gaurav Jain, S. Trussler and J.R. Dahn, J. Electrochem.Soc. **160**, A117, (2013).
25. A.J. Smith, N.N. Sinha and J.R. Dahn, J.Electrochem. Soc. **160**, A235, (2012).
26. T. Zheng and J. R. Dahn, Phys. Rev. B, 53, 3061 (1996).
27. J.C. Burns, N.N. Sinha, G. Jain, H. Ye, C.M. VanElzen, W.M. Lammana, A. Xiao, E.Scott, J.Choi, and J.R. Dahn, J. Electrochem. Soc., 159, A1105 (2012).

CHAPTER 4

Effect of Discharge rate on Capacity Retention of $Li[Ni_{1/3}Mn_{1/3}Co_{1/3}]O_2$/Graphite pouch cells

4.1 Introduction

Although few companies have launched production of electric vehicles, most of vehicles around the world are powered by combustion engines. This is a real concern in terms of petroleum shortage/cost, and environmental problems, and it needs to be replaced by a green technology. Lithium-ion batteries are considered as the best technology to replace the old petroleum related technologies in vehicles. In fact, lithium-ion battery is the only viable technology for ground transportation unless major improvement happens in the other power source technologies like fuel cells [1]. Therefore, it is essential to investigate lithium ion batteries and improve their performance, in order to meet the costumer's needs. Discharge rate capability of lithium ion cell is of great importance in automotive application specially during the period of high acceleration. Generally speaking, battery performance would suppress with cycle and calendar life. Even though, performance of Li-ion cell extremely depends on application type (operating temperature/voltage) [2], but one can generally say that the failure of Li-ion cell could be due to the capacity fading or/and impedance rising. This is due to the parasitic reactions happening inside the cell between charged electrode and electrolyte. The failiur mechanisms were discussed before in chapter 3. The main purpose of this study is to probe condition that may accelerate active material loss mechanism in failure of pouch cells. It is essential to understand which failure mechanism is dominant at a certain application so an appropriate change in Li-cell can be made in order to prolong its life time.

4.2 Pouch cell preparation

Dry machine-made $Li[Ni_{1/3}Mn_{1/3}Co_{1/3}]O_2$/graphite pouch cells, with 220 mAh capacity, were obtained without electrolyte from Whenergy (Shandong, China). The cells were vacuum sealed in China after assembly and shipped to us in a sealed state. The pouch cells were cut open and were vacuum dried overnight (10 to 14 hours) at 80°C to remove any residual water. The pouch cells were filled with 0.90 g of 1M $LiPF_6$ in ethylene carbonate:ethyl methyl carbonate (EC:EMC, 3:7 by weight obtained from Novolyte Technologies, now BASF) electrolyte with 2% Vinylene Carbonate (VC) as additive (obtained from BASF). After filling, the cells were vacuum sealed at -94 kPa (gauge pressure) with a sealing bar temperature of 150°C. All the mentioned processes have been done in an Argon filled glove box. After filling with electrolyte, the pouch cells were connected to a Maccor 4000 series charger and held at 1.5 V for 24 h in a 40°C (± 0.1°C)

temperature-controlled box. Then the pouch cells were opened and resealed inside the glove box after being charged to 3.6 V at C/20 rate and same temperature, in order to remove any produced gasses during formation process. The pouch cells then were connected to Moli system charger for those cells that were charged at C/5 and discharged at C/2, C, and 2C. Every 20 (or in some cases 25) cycles cells were cycled at C/25 for one charge and discharge in order to scan the fade and also generate a low rate cycle for dVdQ analysis which will be explained later. Because of the current limitation of Moli system, a pair of cells was connected to Maccor charger to cycle at C/5 and 4C (charge and discharge respectively). Then they were connected to Moli system frequently to generate low rate cycle at C/25. All the cycling processes on both Moli and Maccor have been done at 30^{o}C in a temperature-controlled box using lower and higher cut-off voltage of 3 and 4.2 V respectively.

4.3 Aging mechanism study method

Differential voltage analysis was performed on all the cells using a software package written at Dalhousie University[3]. This was discussed in detail in chapter 3.

Reference curves for the electrodes in the cells were generated by cycling each electrode (obtained from fresh dried pouch cell after removing electrode from one side of current collector using N-Methyl-2-pyrrolidone/NMP) separately in a 2325 coin-type cell vs lithium metal at a C/25 rate and 30 ± 0.1^{o}C. Each coin cell was assembled using a disk punched from electrode sample, two Celgard 2300 separators, and a lithium foil disk. The electrolyte in the coin cells was same as that in the pouch cells.

Electrochemical impedance spectra (EIS) were measured using a BioLogic VMP3 equipped with two EIS boards. All impedance spectra were collected at a cell potential of 3.60 V over a frequency range of 100 KHz to 10 mHz. EIS measurements were performed at constant temperature by housing the cells in thermostats controlled at 10.0°C (± 0.1°C).

Scanning electron microscope (SEM) images were collected with a Hitachi S-4700 SEM after rinsing the electrodes in Dimethyl Carbonate (DMC) for 5 minutes inside the glove box to ensure there is no residual salt remaining on the surface of electrodes.

4.3 cycling behaviour

Figure 4.1 shows the cycling behavior of the representative cells from each group of cells with different discharge rate.

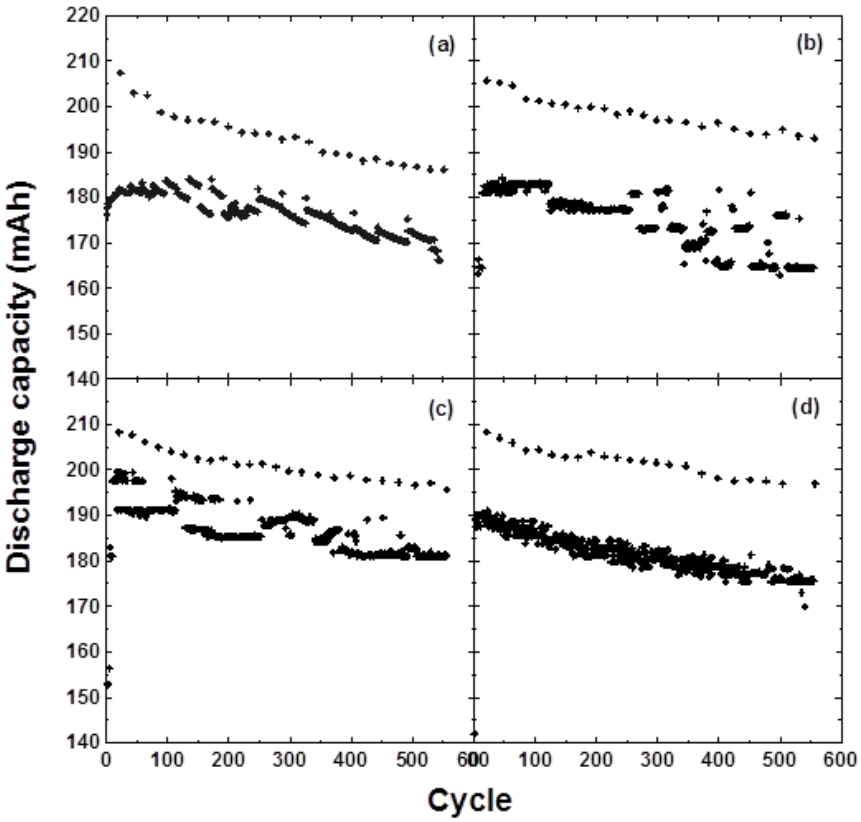

Figure 4.1. Discharge capacity versus cycle number for pouch cells cycled at (a) 4C, (b) 2C, (c) C, and (d) 0.5C rate.

The upper data points in each panel correspond to cycling at C/25 rate, which obviously show higher capacity with respect to high rate cycling showed at lower data points in each panel. The segmentation in data point for the 4C cell connected to Maccor is due to the stabilization of cell when it is being reconnected to Moli for low rate cycle at C/25 after being idle for about couple of hours at fully charge state, and being on the bench for couple of days before measuring impedance at 3.6V (Fig.4.1a). This suggest that lithium atoms get stock in over hang region and come back to shuttling process when cell is reconnected to the charger. The fluctuation in high rate cycling data points is due to the inaccurate timing of Moli system when high current has been applied. This become better with decreasing the current (Fig.4.1.b,c, and d). According to low rate cycles, 0.5C, C, 2C, and 4C pouch cells have lost 4.7%, 5.7%, 7.2%, and 10.6% of their initial capacity

respectively. Later in this chapter the reason that high rate cells have lost more capacity with respect to low rate ones will be discussed.

Figure 4.2 shows differential voltage analysis for different cycles of 0.5C pouch cell.

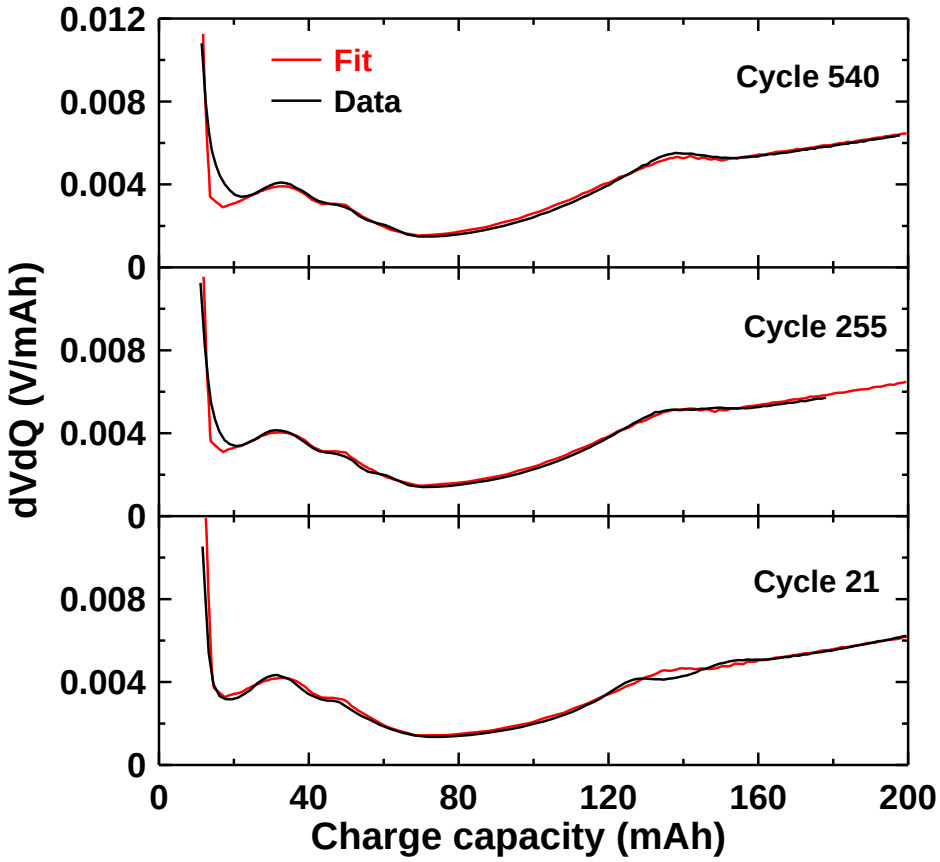

Figure 4.2. Differential voltage analysis (dV/dQ vs.Q) for pouch cell cycled at 0.5C. Charge cycles of 21 (lower panel), 255 (middle panel), and 540 (upper panel) at C/25 rate were selected to fit using reference curves generated from the same electrode materials as used in the cells.

The black curves are the experimental data (collected on the Moli system at a C/25 rate and at 30ºC) and the red curves are calculated data from Equation 3.3. As it shows in lower panel of Figure 4.2, at very early cycles, there are two unusual humps corresponding to graphite staging at capacity about 140mAh. This causes poor fitting at cycle 21 for these cells. At higher cycles these two humps merge together slowly with cycle number which seems to happen earlier at pouch cells experienced lower rates of cycling. Middle panel of Figure 2 shows the first low rate cycle that does not show the two humps at mentioned capacity. As it showed at middle and upper panel of Figure 4.2,

fits on both cycle 225 and 540 are pretty decent. It is unclear to us why these two humps are showing up at early cycles and merge together later on.

Figure 4.3 shows differential voltage analysis for the last cycle (just before disassembling the cells) of a representative cell from each group of twin cells discharged at different rates. Both negative and positive masses are stable as it has been shown in Table 4.1.

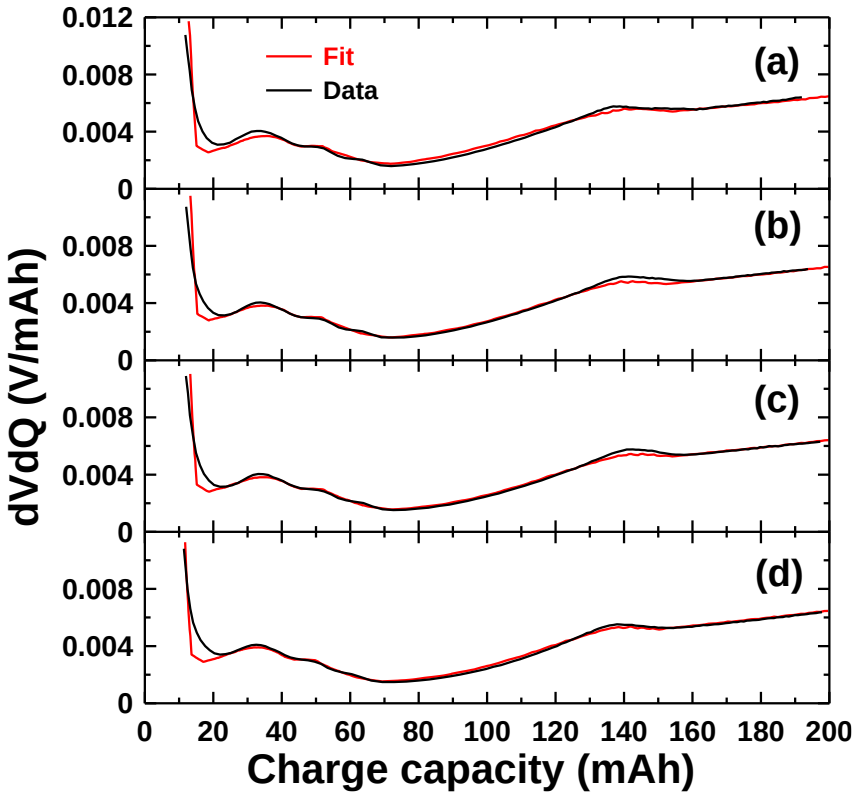

Figure 4.3. Differential voltage analysis (dV/dQ vs.Q) for pouch cells cycled at (a) 4C, (b) 2C, (c) C, and (d) 0.5C rate. Charge cycles of 540 at C/25 rate were selected to fit using reference curves generated from the same electrode materials as used in the cells.

Table 4.1. Differential voltage (dvdQ vs. Q) analysis results of pouch cells discharged at 0.5C, C, 2C, and 4C. This masses and slippages are those that provided best fit of experimental results.

Rate/Cycle	**Mass(-) (g)**	**Mass(+) (g)**	**ΔMass(-) (%)**	**ΔMass(+) (%)**	**Relative slippage (mAh)**	**Capacity (mAh)**
4C/21	0.812	1.276	N/A	N/A	4.11	207.33
4C/320	0.828	1.309	1.97	2.58	17.80	192.15
4C/540	0.833	1.306	2.58	2.35	24.97	186.19
2C/21	0.800	1.295	N/A	N/A	3.82	205.72
2C/255	0.829	1.273	3.62	-1.70	9.39	198.90
2C/540	0.821	1.274	2.62	-1.62	15.87	193.00
C/21	0.799	1.290	N/A	N/A	2.52	208.22
C/255	0.821	1.264	2.75	-2.01	5.02	201.30
C/540	0.832	1.280	1.33	1.26	13.43	195.64
0.5C/21	0.796	1.275	N/A	N/A	1.10	208.26
0.5C/255	0.812	1.256	2.01	-1.49	6.39	202.14
0.5C/540	0.818	1.273	2.76	-0.15	11.44	197.00

The negative electrode mass, positive electrode mass and slippages are those that provided best fit to the experimental data. The small differences in masses are close to the level of error in this technique, and also error due to the unusual humps at early cycles, so it is very likely that no loss of active mass occurred during cycling of these cells. Δmass presented in the Table.1, is the difference of mass between mentioned cycle in the table and cycle 21. In fact, if we look at just cycles 255 and 540 to eliminate the error made by previously mentioned humps at cycle 21, the mass change become way less than what is reported in the Table 4.1.

Figure 4.4 shows the potential vs. capacity of both negative and positive electrodes versus lithium metal as exported from dVdQ analysis, also the full pouch cell V(Q) curves of different rates shown in Figure 4.3. The potential of both positive electrode and full pouch cell are shown at left axis while the potential of negative electrode is shown on right axis. As it can be seen in Figure 4, for all the cells, negative electrode slips to higher capacity with respect to positive electrode. The slippage is increasing with C-rate, which suggests that in high rate cells more lithium atoms have been consumed to thicken and/or repair the SEI layer of the negative electrode during the cycling.

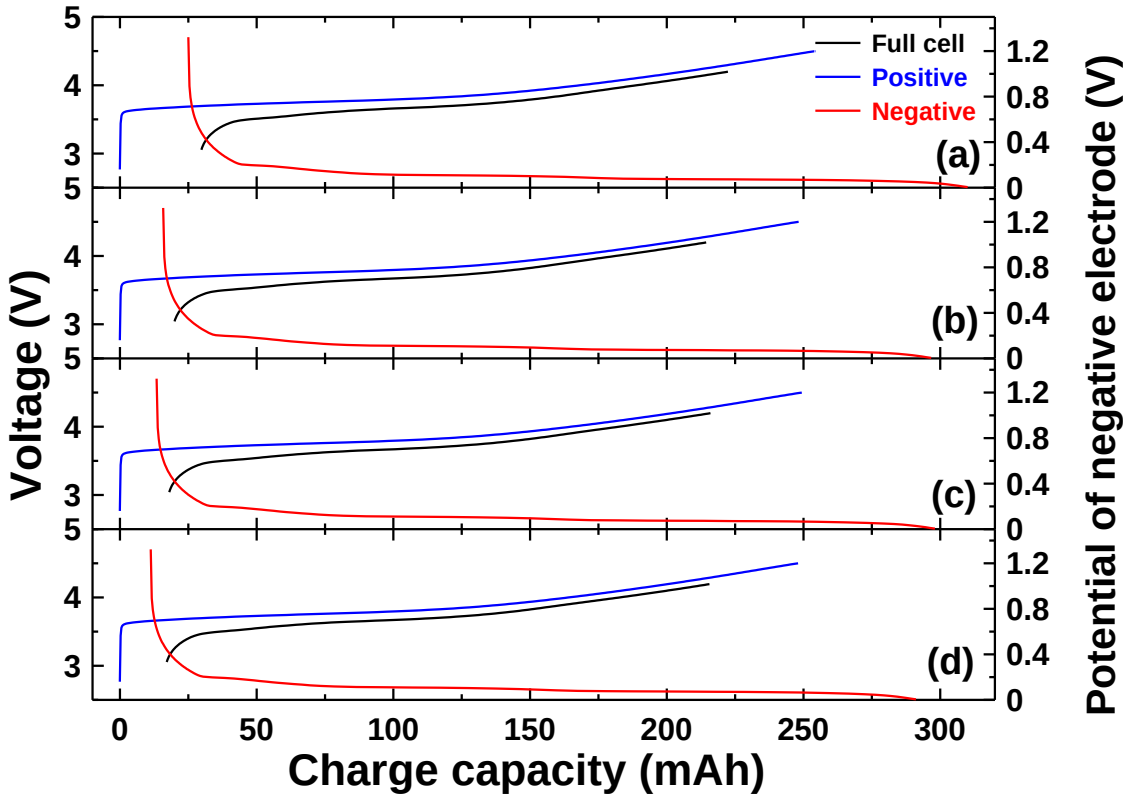

Figure 4.4 Voltage versus capacity for charge cycles at C/25 rate of pouch cells shown in Figure 3. The potential versus capacity of the positive (blue) and negative electrodes (red) vs. Li/Li^+ as determined from dV/dQ analysis in Figure 3 are also shown. The black curve is the experimental full cell voltage curve. All curves have been offset so the fully lithiated positive electrode is at Q = 0.

Figure 4.5 shows relative electrode slippage versus capacity fade. Relative electrode slippage is the difference between capacities of fully lithiated NMC and fully delithiated graphite, and it is exported from dVdQ analysis fits. A dashed line with slope of 1.00 is placed in Figure 5, which shows that the capacity loss and relative slippages are correlated fairly well. This suggest that negligible mass loss is occurring in these cells and almost all the capacity loss is due to the unwanted reaction happening between electrode and electrolyte, specially at negative electrode SEI.

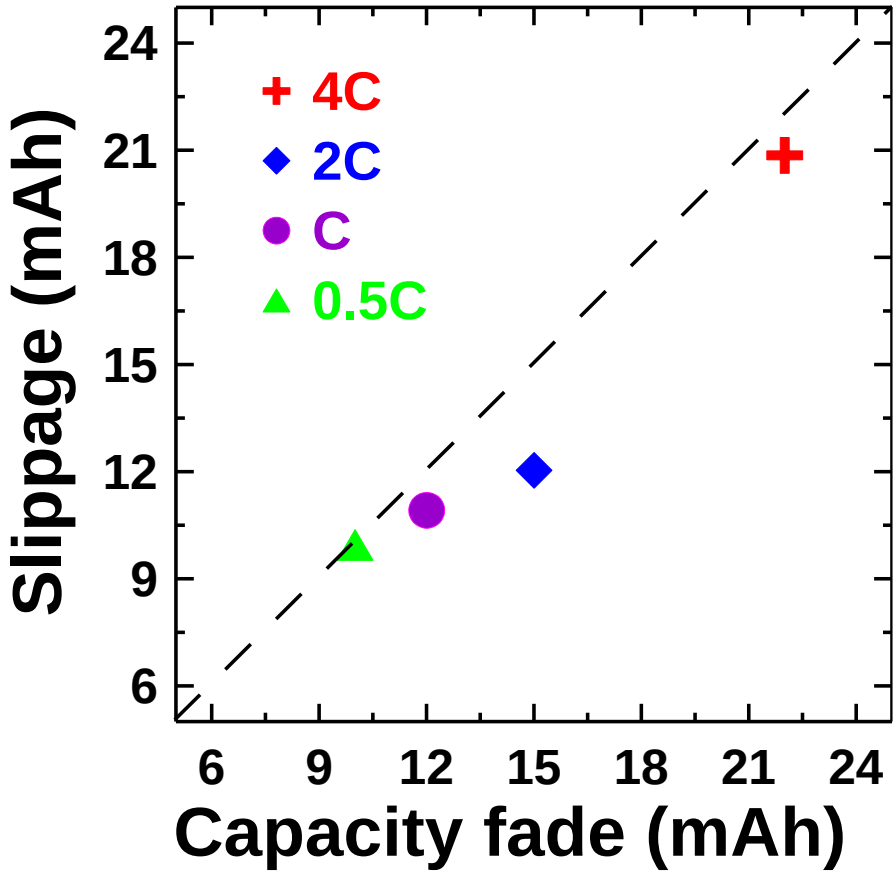

Figure 4.5. Relative slippage for pouch cells as determined from differential voltage analysis software versus capacity loss during cycling at different rates as mentioned in the figure. Dashed line with slop of one is placed in the figure.

Figure 4.6 shows the electrochemical impedance spectroscopy (EIS) data collected at 10°C and 3.6V. Figure 4.6.a shows the EIS data of 4C pouch cell collected at different cycle number. The impedance spectra is a perfect semicircle at beginning and it turned to two semicircle which according to our previous studies **[**4, 5**]** the first one corresponds to negative electrode and second one to positive electrode. Generally speaking, negative electrode impedance is decreasing with cycle number while positive electrode impedance is increasing with cycle number. Looking at whole spectra, impedance is growing as products of side reactions on electrode surface increases the internal resistance, but at some point (cycle 315) impedance stops growing. This behaviour has been seen in the other pouch cells as well. This could be due to the decrease in negative electrode impedance which will be explain later in this paper why is happening. Figure 4.6.b shows the impedance spectra at both cycle 63 and cycle 540 for pouch cells cycled at different rates. At cycle 63, impedance spectra are almost a perfect semicircle, specially, for low rate cells which slowly turn to two semicircles with different shapes corresponding to contribution of negative and positive electrodes.

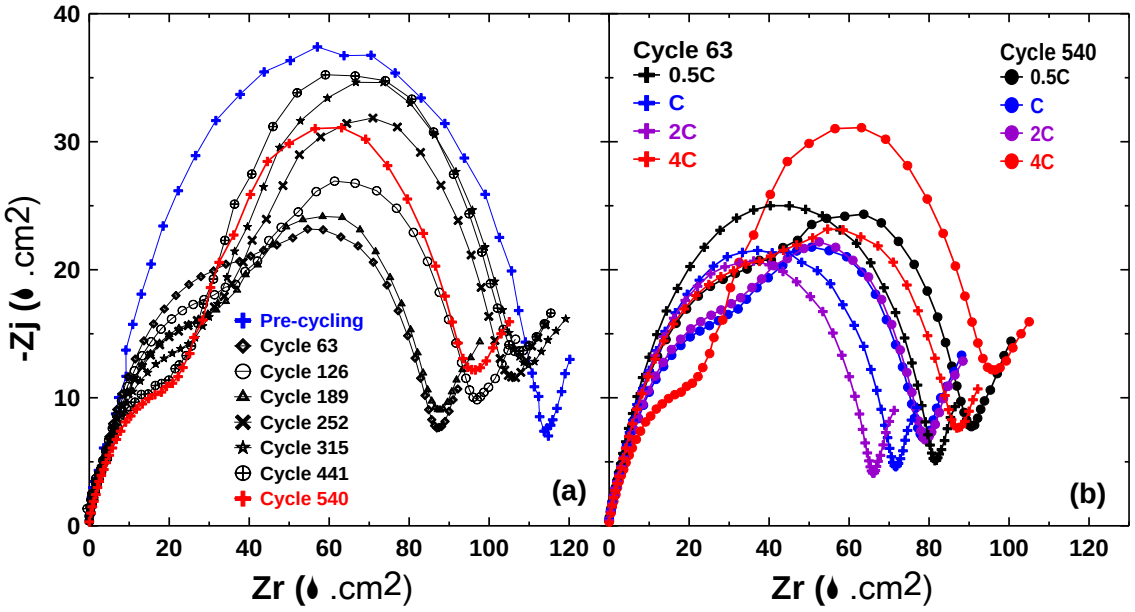

Figure 4.6. Impedance spectra of (a) pouch cell cycled at 4C rate at different cycles as mentioned in the figure, and (b) very early and last cycle of pouch cells cycled at different rates as mentioned in the figure. Impedance spectra were collected at 3.6 V and 10 °C.

Figure 4.7 shows the Bode plot of symmetric cells prepared after disassembling the 0.5C, and 4C pouch cells. The presented Bode plot is real and negative imaginary part of the impedance as function of the logarithm of frequency. Bode plots are very useful to compare impedance of negative and positive symmetric cells, as well as the remade full cells at same frequency. Figure 7 shows the Bode plot of the remade full cell impedance along with negative symmetric impedance divided by two [(-/-)/2] and positive symmetric impedance divided by two [(+/+)/2]. As it can be seen in Figure 4.7 a& d, both imaginary and real parts of impedance are smaller in remade full cell of 0.5C pouch cell with respect to 4C pouch cell. This is in agreement with pouch cell impedance showed at Figure 4.6.b. This trend is also clearly seen at Figure 4.7 c& f, which shows the impedance of positive symmetric cell. As expected from Figure 4.6.a, negative symmetric cell shows that impedance of negative electrode in 4C pouch cell is less than the 0.5C pouch cell (Figure 7 b& e). Figure 4.7 shows excellent agreement with our assumption of positive and negative impedance in Figure 4.6.

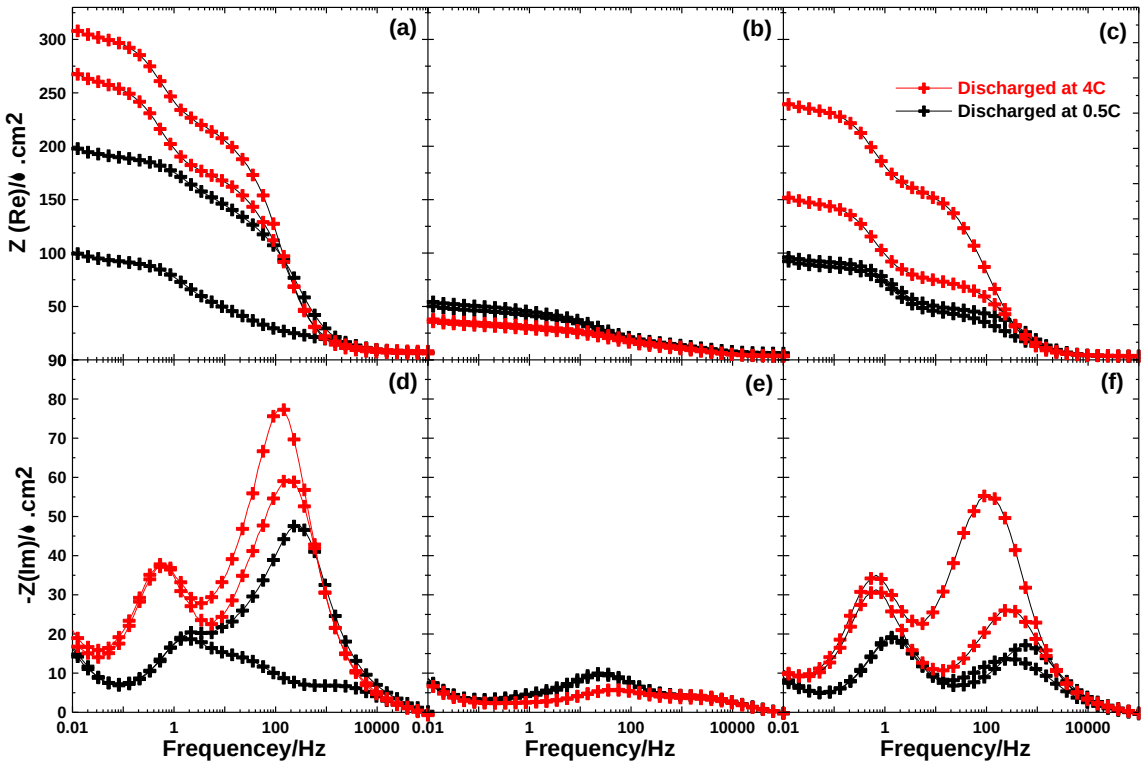

Figure 4.7. Area-specific real impedance as a function of logarithm of frequency (a to c) and area-specific negative imaginary impedance as function of logarithm of frequency (d to f) for remade full cell (a& d), negative symmetric cell divided by two (b& e), and positive symmetric cell divided by two (c& f). Data presented is for 0.5C pouch cell (black) and 4C pouch cell (Red) as mentioned in the figure.

Figure 4.8 shows the summarized bar chart of fitted impedance spectra of pouch cells and symmetric cells. A simple RC circuit was used to fit all the impedance data presented in Figure 4.8. Figure 4.8.a shows the fitting results of pouch cells discharged at 0.5C, C, 2C, and 4C. As it shows, negative impedance is decreasing with C-rate while positive impedance generally follows an increasing path. This is clearly seen at fitted results of two remade full cells from 0.5C pouch cell, and 4C pouch cell presented in Figure 8.b. Fitting results of impedance spectra of 4C pouch cell at different cycle number shows also that negative impedance is decreasing with cycle number (Figure 4.8.c).

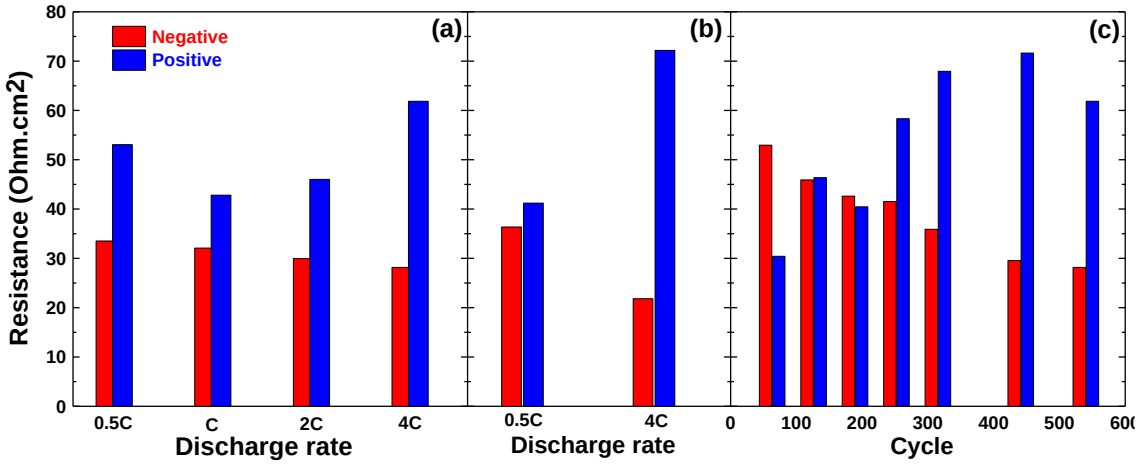

Figure 4.8. Charge transfer resistance of (a) pouch cells at cycle 540, (b) symmetric cells made from 0.5C and 4C pouch cells, and (c) 4C pouch cell at different cycles. Negative resistance is shown by red bars and positive resistance by blue bars**.**

Figure 4.9 shows the SEM images of positive electrode of pouch cells. The low magnification NMC images presented at Figure 4.9.a,c, and e, clearly show side reaction products on the surface of 0.5C cell and 4C cell electrodes compare to pristine NMC. Although it is hard to compare SEM images of positive electrode of 0.5C pouch cell and 4C pouch cell, but it clearly shows some species on the surface of particles as a reason of positive impedance growing. High magnification images at Figure 4.9.b, d, and f, show that even by hammering the positive electrode at 4C rate no particle damage is occurring and particles are nicely connected by carbon black. Therefore, positive mass loss and/or disconnection of positive particles could not be responsible for capacity loss in these cells.

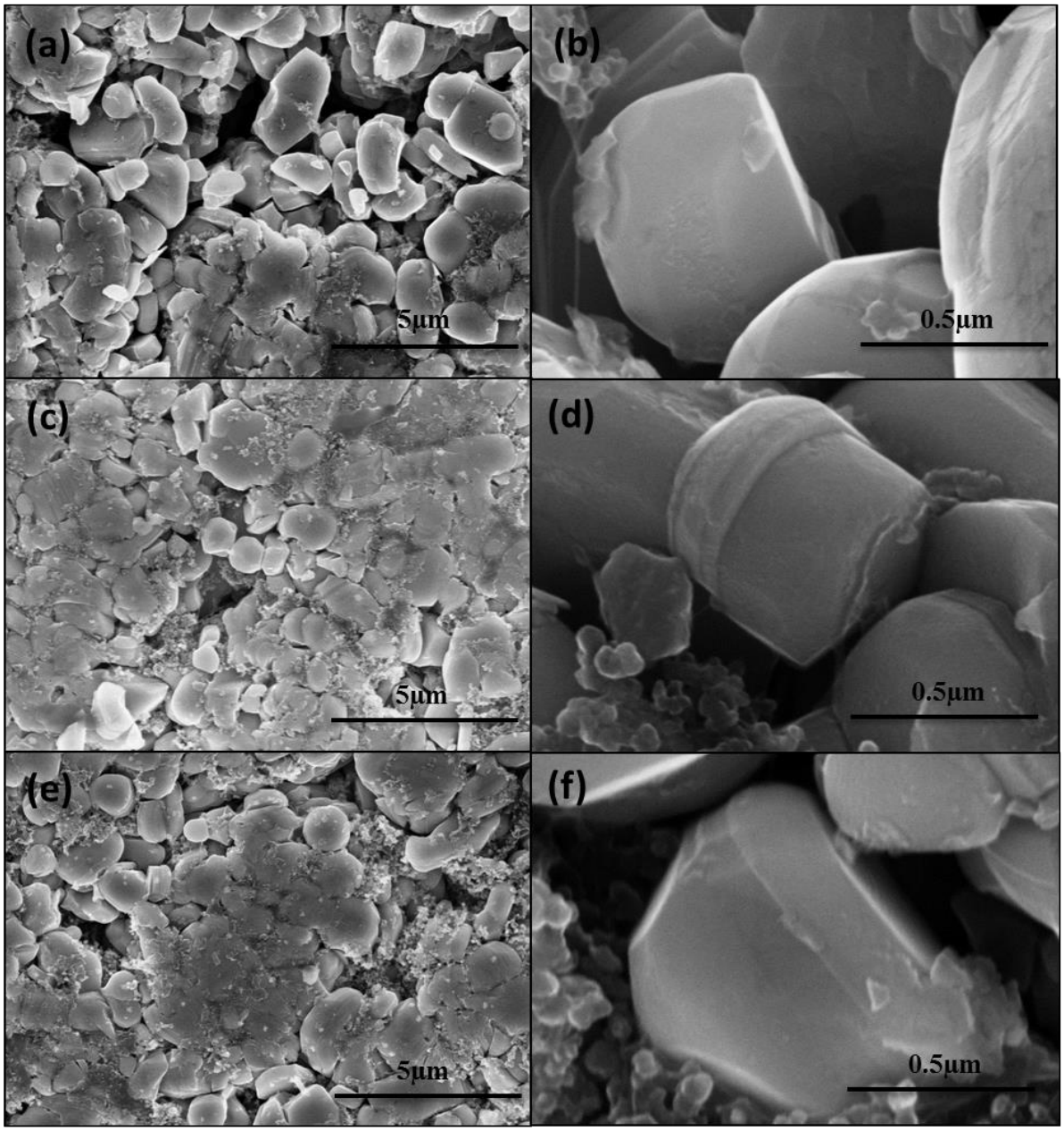

Figure 4.9. SEM images of positive electrode of pristine pouch cell (a& b), pouch cell cycled at 0.5C (c& d), and pouch cell cycled at 4C (e& f).

Figure 4.10 shows SEM images of negative electrode of disassembled pouch cells. Pristine negative electrode presented at Figure 4.10.a& b shows graphite particles in a healthy and solid manner. By looking at graphite particle of 0.5C pouch cell (Figure 4.10.c& d) small cracks can be easily seen. These cracks and holes get bigger in 4C pouch cell presented in Figure 4.10.e& f. This nicely explains the higher slippage of 4C pouch cells with respect to lower rate pouch cells. The creation of these cracks and holes (either particle crack or SEI crack) by high rate lithium de-intercalation of graphite exposes new and clean surface of graphite to the electrolyte. Consumed lithium atoms in

forming new SEI and repairing damaged SEI layer are responsible of higher slippage and capacity fade in high rate cells. This is also in extreme agreement with lower impedance of negative electrode at high discharge rate cells, since increasing the surface area makes lithium intercalation easier and its internal resistance lesser.

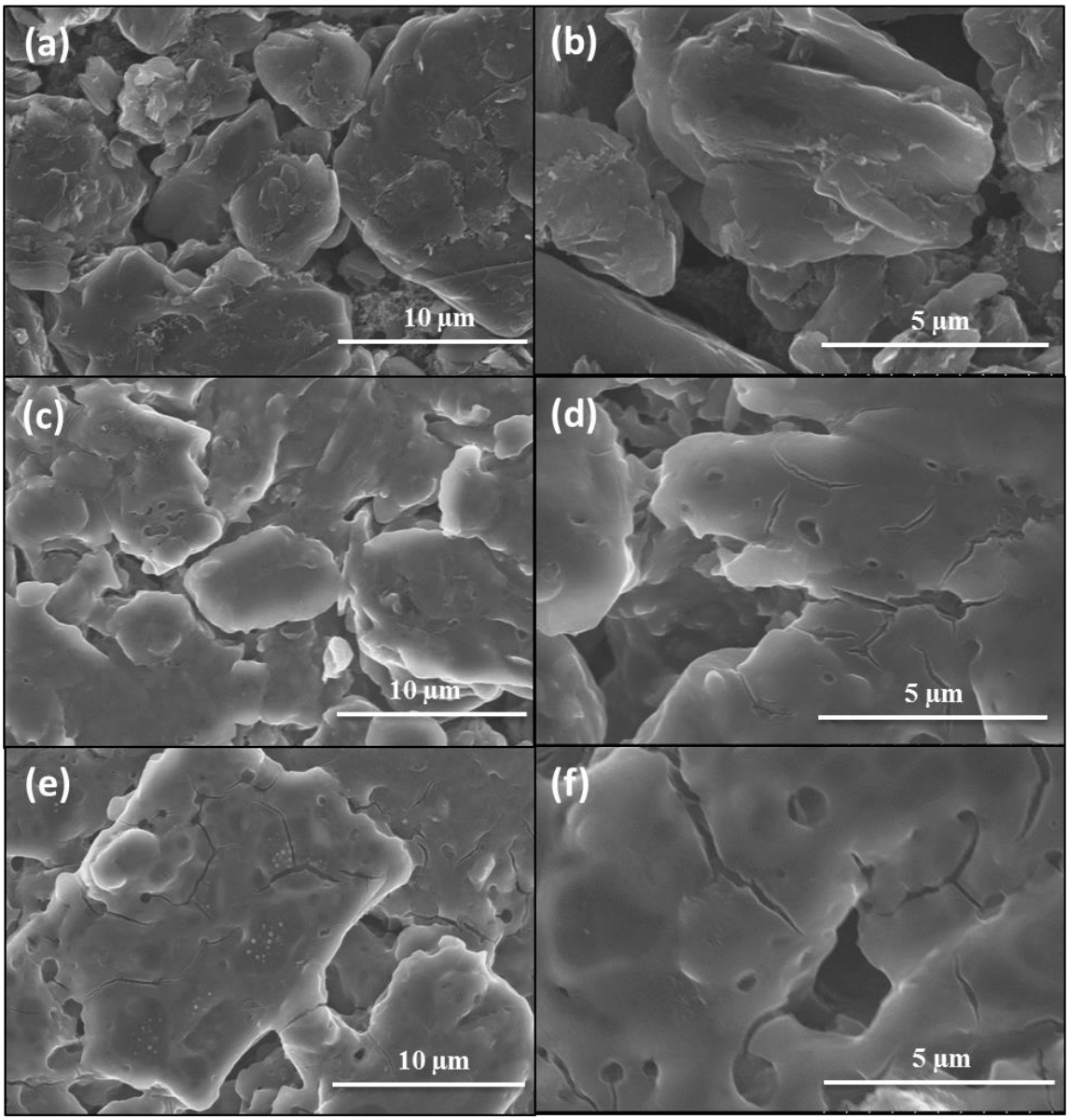

Figure 4.10. SEM images of negative electrode of pristine pouch cell (a& b), pouch cell cycled at 0.5C (c& d), and pouch cell cycled at 4C (e& f).

References

1. H.D. Yoo, E. Markevich, G. Salitra, D. Sharon, and D. Aurbach, Mater Today., 17, 110 (2014).
2. R. Fathi, J. C. Burns, D. A. Stevens, Hui Ye, Chao Hu, Gaurav Jain, Erik Scott, Craig Schmidt, and J. R. Dahn, J. Elechtrochem. Soc., 161, A1572 (2014).
3. Hannah M. Dahn, A. J. Smith, J. C. Burns, D. A. Stevens, and J. R. Dahn, J. Electrochem. Soc, 159, A1405 (2012).
4. R. Petibon, N.N. Sinha, J.C. Burns, C.P. Aiken, Hui Ye, Collette M. VanElzen, Gaurav Jain, S. Trussler and J.R. Dahn, Journal of Power Sources, **251**, 187 (2014)
5. R. Petibon, C.P. Aiken, N.N. Sinha, J.C. Burns, Hui Ye, Collette M. VanElzen, Gaurav Jain, S. Trussler and J.R. Dahn, J. Electrochem.Soc. **160**, A117, (2013).

CHAPTER 5

Electrochemical properties of Tin as a possible anode material for Na-ion batteries

5.1 Introduction

Since first commercial production of Li-ion batteries in 1991, Li row material has been highly demanded to power not only portable electronic devices but also EVs and HEVs (electronic and hybrid electric vehicles). As it was mentioned in chapter 1, this issue has turned Li to a strategic and expensive material which is unfortunately in short supply and it may not meet the industrial needs in the near future. This concern has motivated scientists to develop different battery systems and, recently, among them the Na ion rechargeable batteries, which were initially investigated earlier than Li-ion batteries became commercially available [1-3]. Since Na is one of the most abundant elements in the Earth's crust, Na–ion systems can really become alternative for Li-ion batteries. Considering carbon [4] and Nax(x = 0.66)Mn0.5Fe0.5O2 [5] as a possible anode and cathode, respectively, the energy density, calculated according to only active materials weigh, for such a Na ion battery would be around 275 Wh/kg, which is about 70% of commercially available Li-ion battery, so far. This limitation is mainly due to two factors: The discharge voltage profiles of the mixed oxide which would reduce the operative voltage of the whole system and the lower specific capacity of the hard carbon/Na+ system compared to the lithiated graphite. Moreover, the specific power of the battery may be limited by the low discharge kinetic of hard carbon. Similar electrochemical properties of Na and Li show that materials, electrolytes, and cell structures, which have been used in Li-ion batteries, may be suitable for Na ion rechargeable batteries; this has been already proven. Many positive electrodes, constituted of some metal oxides (Na0.44MnO2 [6], Na*x*CoO2 [7] Na*x*Mn0.5Fe0.5O2 [5]), NASICON-type materials (Na3V2(PO4)3 [8]), olivine phases (NaFePO4 [9]), and others (NaVPO4F [10]) were successfully used. On the contrary, even if there are some studies of possible anode materials, a good negative electrode is still one of the fundamental impediments in progressing Na-ion batteries; in fact, Na does not intercalate between typical graphitic carbon sheets [11]. Nevertheless, other different materials can be used as negative electrodes, among them the Na-metal alloys showing, in phase diagram wide biphasic regions can play an important role; in particular, if the composition of each compound has high amount of sodium. For this reason, the Na-Sn system was investigated; in fact, as reported by Sangster and Bale [12] (Figure 5.1), at temperatures lower than 100 °C, many

biphasic regions with compounds having large amount of sodium (from NaSn6 to Na15Sn4) are present.

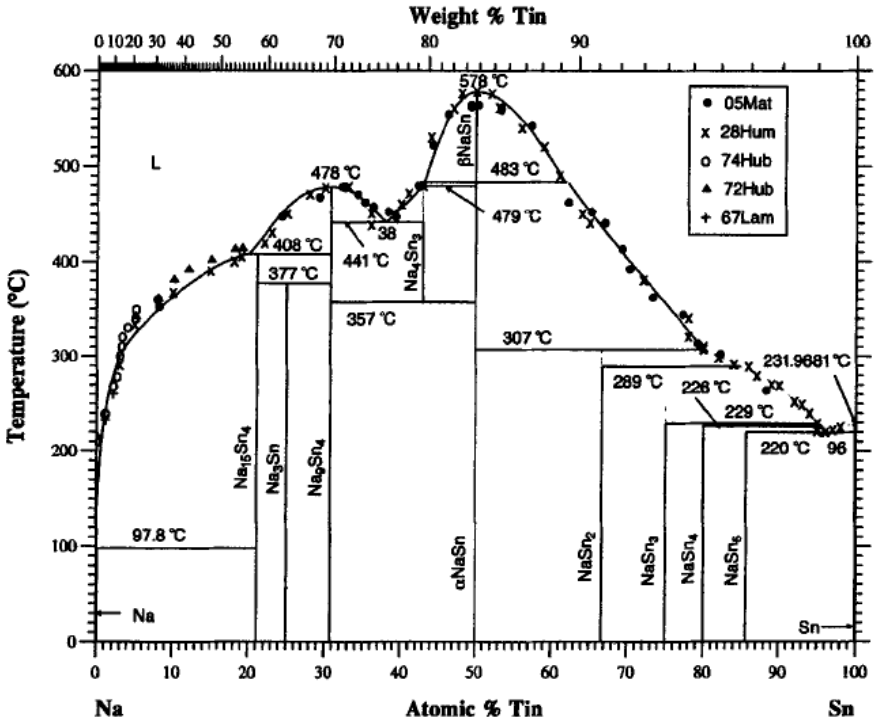

Figure 5.1. Phase diagram of Na-Sn [12].

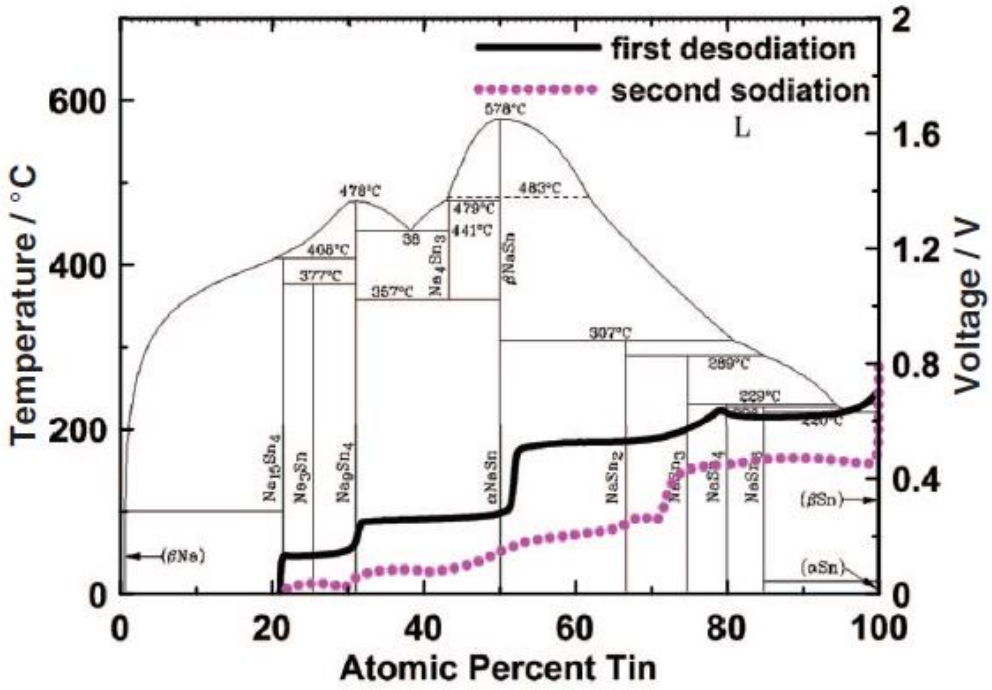

Figure 5.2. Voltage curves of the first desodiation and sodiation half cycle of sputtered tin superimposed on the Na-Sn binary phase diagram[13].

Figure 5.2 shows the voltage profile versus atomic percent of Sn superimposed on phase diagram of Na-Sn . As it shows, many of two phases indicated in the equilibrium phase diagram are absent, and it is not possible to achieve electrochemically. However, the last three plateaus of voltage profile are presented and which are corresponding to NaSn, Na_9Sn_4, $Na_{15}Sn_{14}$ [13].

In such conditions, invariant and high chemical potentials of Na have to be present and electrodes with theoretical capacity of about 850 mAh/g might be realized. However, these capacity values are generally observed for a very few cycles in conventional composite electrodes. Looking at the wide knowledge coming from the investigation of such class of materials in lithium ion batteries, the first source of electrode failure is the decrepitation due to the large volume expansion and contraction during the alloying/dealloying process, respectively. In fact, the commercial available binders are not able to accept the stress induced by the strain coming from the reaction with the consequent electrode pulverization. A good way to avoid using binder is to produce Sn layer directly onto proper current collectors. This can be made by several methods, among them electro-deposition is one of the most convenient procedures for preparing Sn in different morphologies. In addition, this technique is very low cost with respect to the others, and it does not need any advanced facility.

5.2 Films Preparation and characterization

Tin films have been deposited electrochemically on copper substrates from a chloride bath, using

SnCl2·2H2O and tri-ammonium citrate [14]. Deposition bath was made of 50 g/L tin chloride(II)

and 50 g/L tri-ammonium citrate, dissolved in distilled water. Platinum net, copper foil (1 cm2) and SCE (standard calomelan electrode) were used as counter, working and reference electrodes, respectively. Before electro-deposition, copper substrates were degreased in acetone by applying ultrasonic waves. Depositions have been done while solution was stirring, and current density was 24 mA/cm2 for all depositions.

Microstructure and chemical composition of Sn metal films have been characterized by SEM (scanning electron microscopy) (Vega TS5136 XM Tescan) equipped with an EDX (energy dispersive x-ray) detector, in high vacuum configuration. X-ray diffraction measurement was carried out by Bruker D8

advance XRD (X-ray diffraction) equipped with secondary beam monochromator, copper source (kα radiation), and operating at 0.02 deg/step, and 3 sec/step.

Electrochemical characterizations were carried out using three electrodes T-shaped Swagelok cells equipped with stainless steel current collectors. Sn films, deposited on Cu substrates, were sandwiched between stainless steel and Na metal disc, the latter pasted on the top of current collector. Metallic Na was used as both counter and reference electrodes, and trilayer polypolprylene membranes were used as separators. Separators were wetted by the solution of 1 M NaClO4 in propylene carbonate, which was used as electrolyte. In order to remove all the aqueous remains present in the Sn films, all the electro-deposited samples were dried in vacuum chamber over-night, after drying at 130 °C for 2 h. All potentials are reported vs. Na/Na+ electrode value, and the electrochemical characterizations were performed using Biologic VMP3 multi-channel battery tester, at room temperature. Typical Sn load was 2.5 mg/cm2.

5.3. Results and Discussion

5.3.1Crystal Structure and Morphology

Figure 5.3 shows the SEM images of electrodeposited Sn film. Fig.5.3a shows the landscape image of electrodeposited Sn on copper current collector while Fig.5.3.b shows higher magnifications in order to see crystalline particles clearly. Landscape image and cross section view (Fig. 5.3.c) show very good coverage of Sn on Cu substrate. The Sn tetragonal morphology can be easily observed at higher magnification. Film thickness is around 38 µm , which could vary with electro-deposition time.

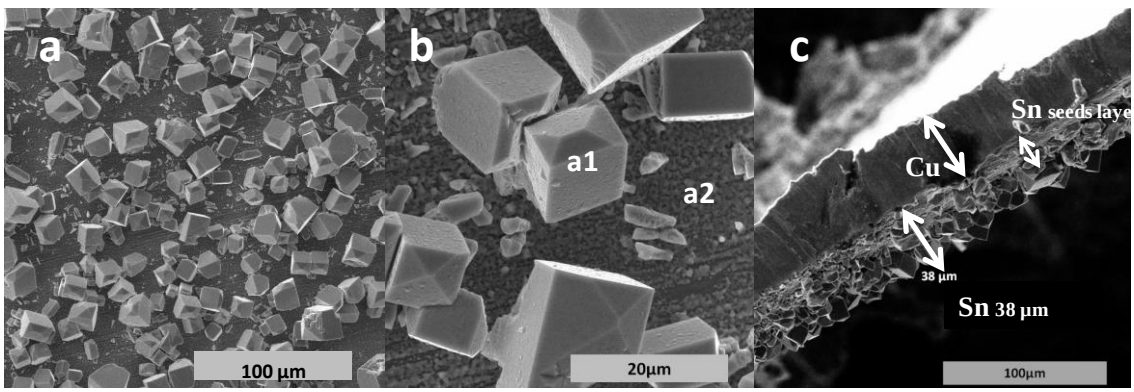

Figure 5.3. SEM images of Sn film deposited at 24 mA/cm^2 a) landscape image top view b) higher magnification of top view, and c) cross section image.

Figure 5.4 shows the EDX spectra corresponding to the points a1 and a2 in Fig 5.3b. It shows the presence of only elemental tin at both points. In our hypothesis, at the solution/current collector interface a Sn film of few µm is firstly formed acting as seeds layer for the growth of highly ordered tetragonal structures. The total film thickness is about 38 µm. It has been proved that such rough morphology shows better cyclic properties with respect to smooth one [15].

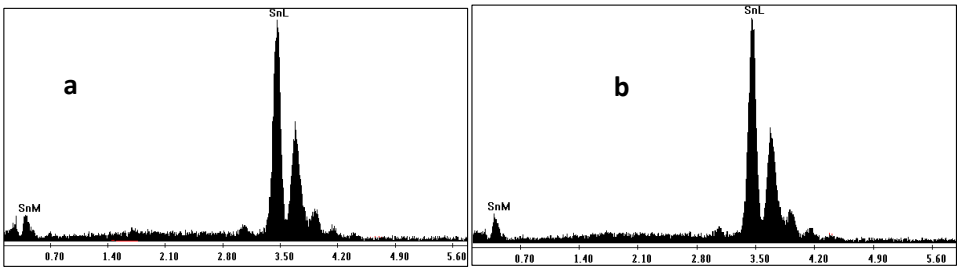

Figure 5.4. EDX spectra for points a) a_1 and b) a_2 shown in figure 5.3.b.

Figure 5.5 shows the XRD pattern of deposited tin film on copper. There are eight peaks: Six of them can be indexed to tetragonal tin [16], with a lattice parameter of a = 0.58329(8) nm and c = 0.31826(7) nm; the other two peaks can be indexed to the copper current collector.

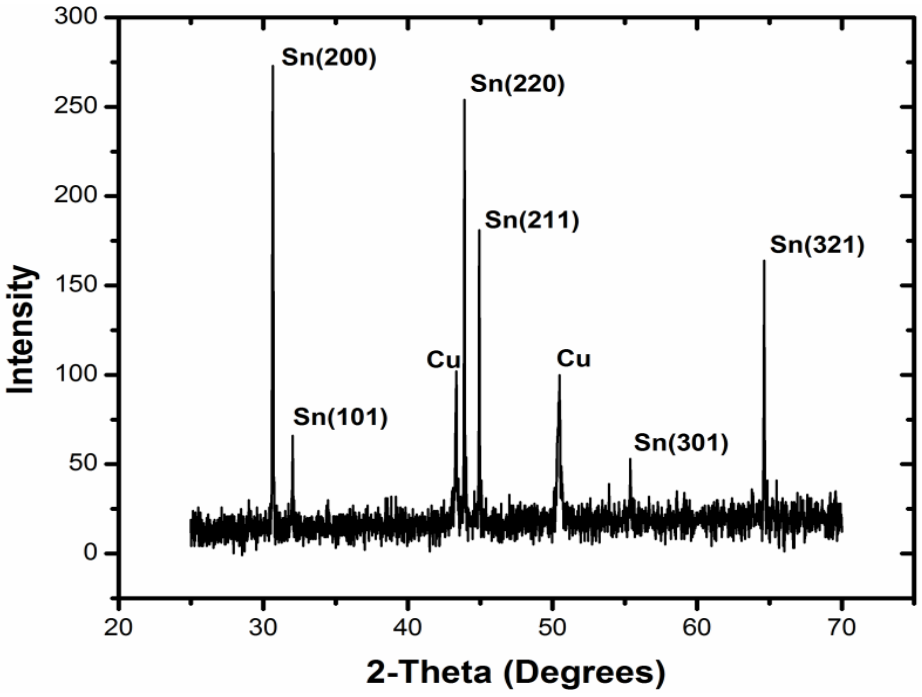

Figure 5.5. XRD pattern of Sn film electrodeposited on Cu substrate.

5.3.2 Electrochemical Analysis

The Sn film electrodes were assembled into half-cells with Na metal as counter and reference electrodes. No binders or conducting carbon were used. The half-cells were studied using EPS (electrochemical potential spectroscopy) [17], and galvanostatic charge/discharge cycling. In EPS measurement, a series of constant potential steps were applied to the electrochemical cell. On each step, the cell was permitted to attain quasi equilibrium conditions by letting the current decay to a small but finite value (C/50, typically ~ 17 mA/g in our measurements). When small voltage steps (V = 3 mV in our study) are applied, the charge accumulated on each step can be integrated from the measured current to yield an accurate derivative of the voltage-charge relation. This derivative relationship is a very useful tool to define the evolution of the phase equilibrium inside electrode materials. In fact, under thermodynamic equilibrium condition the potential/composition profile obeys Gibbs phase rule.

So, the first derivative of quasi equilibrium charge/voltage curve can show sharp peaks for two-phase regions or bell-like peaks for single-phase regions, revealing whether a phase transformation occurs. Figure 5.5 presents potential profiles obtained by EPS for first two cycles of Na-Sn alloying/dealloying between 0.01 V to 1.00 V.

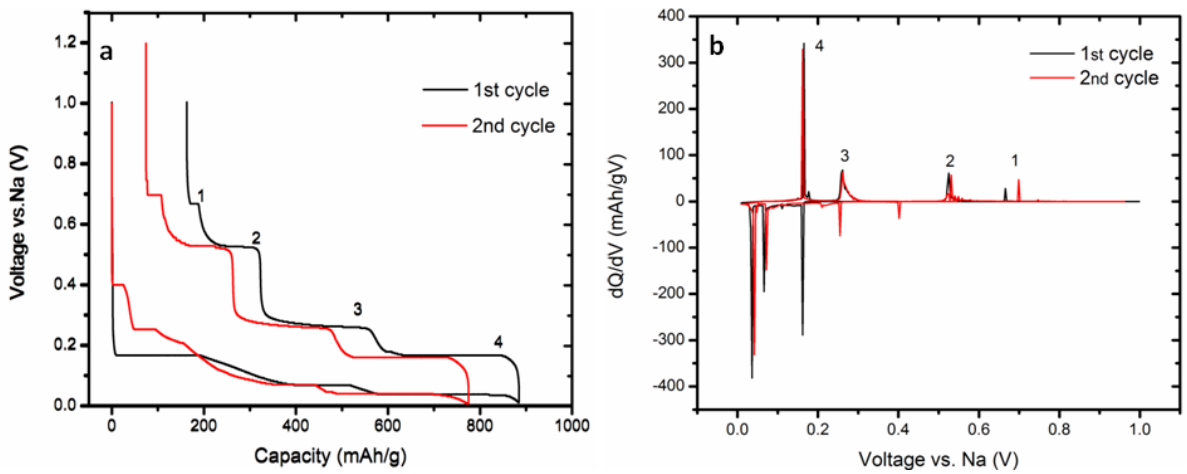

Figure 5.5. a) galvanostatic sodiation and desodiation curves for the first two cycles, b) same experiment reported as incremental capacity v.s. potential.

It is obvious that alloying/dealloying reaction is not completely reversible as charge-discharge tails are not fit to each others, but a significant amount of capacity (82% and 90% during first and second cycle, respectively) has been recovered. During the first alloying reaction, the capacity was 885 mAh/g, which shows achieving final composition of Na15Sn4 (theoretical capacity 847 mAh/g).

The larger observed capacity compared to the expected one may be attribute to the formation of

passivating layer on the Sn surface. The first alloying reaction shows a potential profiles, which is different from the others. In fact, three plateaux are observed at 0.160 V, 0.065 V and 0.040 V, which correspond to three very sharp peaks in the differential capacity curve (Fig. 2b). According to the equilibrium phase diagram, it can be assumed that this three peaks correspond to the formation of the NaSn2, NaSn and Na15Sn4 phases. This behavior was already observed in Sn micrometric particles [18], showing successive strong irreversible de-alloyings. On the contrary, four different plateaux (labeled 1-4 in Fig. 5.5) are present in our profiles during de-alloying reaction in both first and the second cycle. These plateaux can be related to the different biphasic regions present in Na-Sn phase diagram [12]. In reference 13, Ellis et al reported in situ X-ray measurement for Sn sodiation, and demonstrated the existence of three crystalline and one amorphous phases, corresponding to the four plateaux in the voltage profile, close to this one reported

in this work. Accordingly, the equilibrium between Sn/NaSn3, NaSn3/NaSn, NaSn/Na9Sn4 and Na9Sn4/Na14Sn5 correspond to plateaux 1, 2, 3 and 4, respectively.

Figure 5.6 shows cycling performance of electroplated tin film at 3 different C-rates.

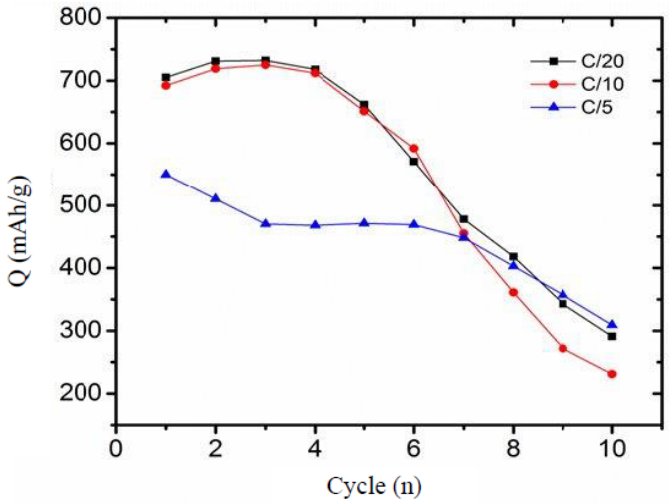

Figure 5.6. Discharge capacity versus cycle number at C/20 (black squares), C/10 (red circles), and C/5 (blue triangles) as indicated in the figure.

In the lower rates (C/20 and C/10, corresponding to 42.5 and 85 mA/g, respectively) range, discharge capacity little increases after the first cycle, most likely owing due to improvement of ions diffusion in the solid state. After the 4th cycle, we have seen decrease in discharge capacity, probably due to active material fading. At higher rate (C/5), the average discharge capacity for the first 6 cycles is 475 mAh/g, which is much less than that at lower rates and highlight that sodiation/desodiation takes place partially. In addition, it seems that C-rate affects directly on the stresses induced by volume expansion/shrinkage taking place during the alloying/dealloying process.

It appears that electro-deposition parameters have high impact on Sn film morphology. For instance, Figure 5.7 presents some films deposited at different current density which show quite different morphology. It might be useful to look at electrochemical properties of these films. However , in this work we have presented only electrochemical properties of the films electrodeposited at 24mA/cm^2 that its morphology is shown at figure 5.3.

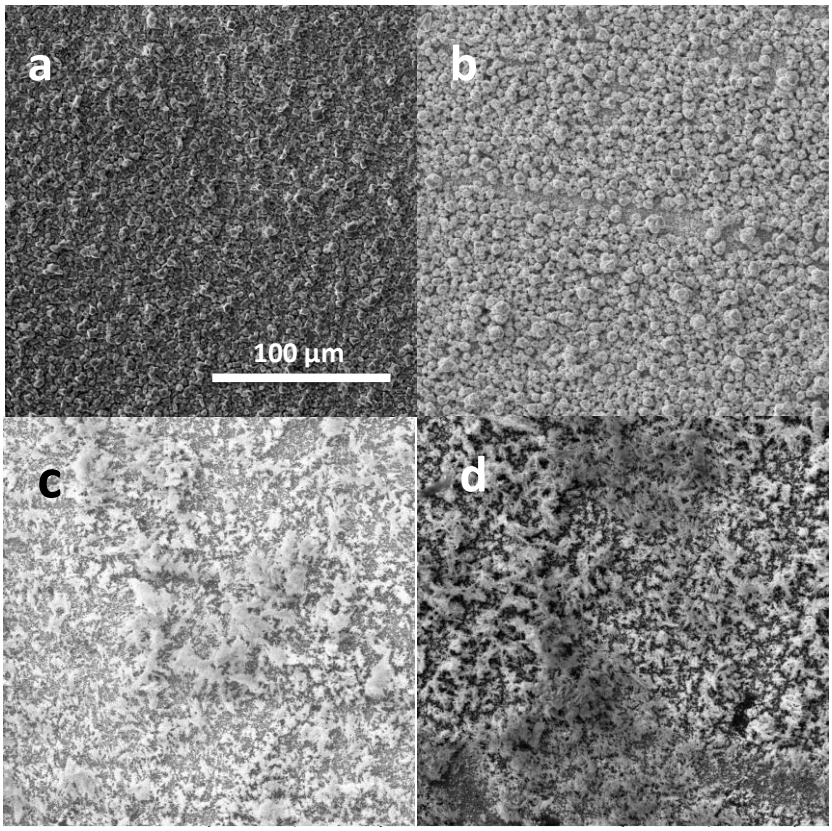

Figure 5.7. SEM images of Sn film electrodeposited at a) 5 mA/Cm^2, b) 10 mA/Cm^2, c) 30 mA/Cm^2 and d) 50 mA/Cm^2 . Magnefication is same for all the sections as presented in section "a".

Since electrodeposition is very low cost technique, and it could be practically used for producing electrode materials for batteries it would be useful to investigate other parameters affecting film morphology. For instance, other parameters like temperature, substrate morphology, type of solution and additives, PH, etc. These parameters could affect the film morphology and it would be very useful to study their effect on electrochemical properties of Sn, in order to prolong the cycling behavior of Sn versus sodium.

References:

1. Tarascon, J. M.; Hull, G. W. Sodium Intercalation into the Layer Oxides NaxMo2O4. Solid State Ionic 1986, 22,85-96.
2. West, K.; Zachau, C. B.; Jacobsen, T.; Skaarup, S. Sodium Insertion in Vanadium Oxides. Solid State Ionics 1988, 28, 1128-1131.
3. Shacklette, L. W.; Jow, T. R.; Townsend, L. Rechargeable Electrodes from Sodium Cobalt Bronzes. J. Electrochem Soc. 1988, 135, 2669-2674.
4. Stevens, D. A.; Dahn, J. R. High Capacity Anode Materials for Rechargeable Sodium-Ion Batteries. J. Electrochem Soc. 2000, 147, 1271-1273.
5. Mortemard, B. B.; Carlier, D.; Guignard, M.; Delmas, C. Structural and Electrochemical Characterizations of P2 and New O3-NaxMn1-yFeyO2 Phases Prepared by Auto-Combustion Synthesis for Na-Ion Batteries. J. Electrochem. Soc. 2013, 160, A569-A574.
6. Sauvage, F.; Laffont, L.; Tarascon, J. M.; Baudrin, E. Study of the Insertion/Deinsertion Mechanism of Sodium into Na0.44MnO2. Inorg. Chem. 2007, 46, 3289-3294.
7. Berthelot, R.; Carlier, D.; Delmas, C. Electrochemical Investigation of the P2-NaxCoO2 Phase Diagram. Nat. Mater. 2011, 10, 74.
8. Saravanan, K.; Mason, C.W.; Rudola, A.; Wong, K. H.; Balaya, P. The First Report on Excellent Cycling Stability and Superior Rate Capability of Na3V2(PO4)3 for Sodium Ion Batteries. Adv. Energy Mater 2013, 3(4), 444-450.
9. Ellis, B. L.; Makahnouk, W. R. M.; Makimura, Y. Toghill, K.; Nazar, L. F. A Multifunctional 3.5 V Iron-Based Phosphate Cathode for Rechargeable Batteries. Nat. Mater. 2007, 6, 749-753.
10. Barker, J.; Saidi, M. Y.; Swoyer, J. L. A Sodium-Ion Cell Based on the Fluorophosphate Compound NaVPO4F. Electrochem. Solid State Letters 2003, 6, A1-A4.
11. Slater, M. D.; Kim, D.; Lee, E.; Johnson, C. S. Sodium-Ion Batteries. Adv. Funct. Mater. 2012, 23, 947-958.
12. Sangster, J.; Bale, C. B. The Na-Sn (Sodium-Tin) System. J. Phase Equilib. 1998, 19, 76-81.
13. Ellis, L. D.; Hatchard, T. D.; Obrovac, M. N. Reversible Insertion of Sodium in Tin. J. Electrochem. Soc. 2012, 159, A1801-1805.

14. He, A.; Liu, Q.; Ivey, D. G. Electrodeposition of Tin: A Simple Approach. J Mater. Sci. Mater. Electron. 2008, 19, 553-562.
15. Shin, N. R.; Kang, Y. M.; Song, M. S.; Kim, D. Y.; Kwon, H. S. Effects of Cu Substrate Morphology and Phase Control on Electrochemical Performance of Sn-Ni Alloys for Li-Ion Battery. J. Power. Source. 2009, 186, 201-205.
16. Swanson, T. Natl. Bur. Stand. 1953, 539, 24.
17. Thompson, A. H. Electrochemical Potential Spectroscopy: A New Electrochemical Measurement. J. Electrochem. Soc. 1979, 126, 608.
18. Datta, M. K.; Epur, R.; Saha, P.; Kadakia, K.; Park, S. K.; Kumta, P. N. Tin and Graphite Based Nanocomposites: Potential Anode for Sodium Ion Batteries. J. Power Sources 2013, 225, 316 322.

CHAPTER 6

$Na_{0.44}MnO_2$ a promising cathode for use in Na-ion batteries

6.1 Introduction

As it has been discussed in previous chapter, with the increase in the commercialization of hybrid electrical vehicles and electrical vehicles powered by lithium ion batteries, the demand of lithium raw material might become astronomical in the near future [1]. This aspect will imply also geopolitical issues as lithium is becoming a strategic material [2]. A possible solution is the development of different battery systems. In this framework, there is growing interest in the sodium based secondary batteries, which were already investigated at the early stage of lithium ion technology but after the commercialization of the first rocking chair battery they were almost abandoned. In fact, there has been an exponential growth in scientific interest about the development of electrode materials for sodium-ion batteries in the last five years. At present, the most promising sodium systems use a transition metal oxide and hard carbon as positive and negative electrode, respectively. In this configuration, considering the material specific capacity and the discharge profiles, the battery could be reason-ably able to display an energy density of about 70–80% of lithium analogous with unexplored power density. However, several poly-crystalline compounds show a lower diffusivity barrier for Na+ compared to Li+ homologous structures [3]. Among the oxide materials, different phases have been proposed like NaCrO2 [4], NaxCoO2 [5–7], NaxMnO2 [8–13], and NaxMn0.5Fe0.5O2 [14] showing capacity about 100–150 mAh/g in the potential range from 2.0 to 4.0 V vs. metallic sodium with good kinetics. In particular, Na0.44MnO2 (NMO) has received significant attention due to the presence of the relative inexpensive and environmental friendly Mn in the structure. In addition, NMO can be prepared via facile synthetic methods such as hydrothermal[9,10], solid-state [8], sol–gel [11], polymer–pyrolysis [12], and combustion processes [11]. However, up to now the poor rate capability of NMO restricts its practical applications in room temperature sodium systems. In fact, Sauvage et al. [8] showed that NMO based electrodes cycled at current higher than C/20 rate displayed a sharp decrease in the delivered capacity. More recently, Cao et al. [12] and Hosono et al. [13] reported improved rate capability using NMO nano-wires, which provided a shorter diffusion path for sodium insertion/deinsertion. Nevertheless, the improved rate-capability is still lower respect to morphology optimized lithium systems. In addition, the sodium intercalation in NMO involves multi-transition steps, which indicates complex structural behavior [15]. Therefore, detailed analysis of the kinetic behavior of NMO based electrodes is needed to exploit its successful use in sodium ion

batteries. A useful tool to study the electrochemical kinetic behavior of electrode material is impedance spectroscopy (IS). In the case of lithium-ion battery components, this approach has been widely used; detailed models exist to take into account the different physical, chemical, and electrochemical contributions to the total electrode impedance of the cell or of one single element (positive electrode, negative electrode, or electrolyte). This approach has been extensively discussed by Barsoukov [16].

6.2 Preparation and characterization of NMO

$Na_{0.44}MnO_2$ particles were prepared by a modified Pechini method starting from sodium carbonate and manganese acetate precursors, which were dissolved in DI water and then mixed with citric acid. The transparent solution was then gently heated to allow solvent evaporation and gel formation. The obtained gel was pre-heated to 300°C to burn the organic binders. Finally, a thermal treatment at 800◦C in air for 9 h was performed to promote the sample crystallization. The NMO crystal structure was characterized by X-ray diffractometer (Rigaku, Model D/MAX-RB, Japan). The morphology was confirmed by Field Emission Scanning Electron Microscope (ModelXL30SFEG, Philips, The Netherlands) and Transmission Electron Microscope (Tecnai G2 F30. 300 kV, Philips, The Netherlands).

6.3 Electrochemical characterization

The electrochemical characterization was carried out using three electrode T-shaped Swagelok cells equipped with stainless steel current collectors. Active material electrodes were fabricated by mixing NMO active material (70%), PVDF binder (15%) and conductive carbon black (15%, Super P MMM Carbon). The mixture was dispersed in n-methyl-pyrrolidone (NMP) to obtain dense slurry which was then cast directly on the stainless steel current col-lector of the Swagelok cell and finally dried at 90◦C for 2 h. Theactive material load was around 2.5 mg/cm2. Metallic sodium discswere pasted at the top of the two different current collectors, and they were used as reference and counter electrode, respectively.All the potentials are reported vs. the couple Na+/Na. The small gap among the electrodes (around 1 mm) was filled with the electrolyte which was a solution of 1 M $NaClO_4$ (ACS reagent, Sigma–Aldrich)in propylene carbonate (Selectipur, Merck). The electrolyte salt was purified by crystallization from dioxane–

water solution and the precipitate was then dried under vacuum at 150◦C. The pro-pylene carbonate solvent was used as received. All the chemicals were stored in Ar filled glove box. The cell arrangement, avoiding the use of a separator, minimizes the number of materials used in cell assembling; thus the result is directly relatable to the material performances. The electrochemical characterization was carried out at room temperature using Biologic VMP3 multi-channel battery tester equipped with the Electrochemical Impedance Spectroscopy (EIS)board. Typical EIS experiments were performed at open circuit volt-age (OCV) in the frequency range from 1×10^5 to 1×10^{-2}Hz undera DC stimulus of 10 mV after attaining the equilibrium conditions, i.e. until no variation of the OCV was observed.

6.4 NMO structure and morphology

The X-ray pattern of the NMO powders prepared by the Pechinimethod is reported in figure 6.1. The lattice structure is orthorhombic and belongs to the Pbam space group, which corresponds to JCPDS card #27-0750. The pattern indicates a good crystallinity of the powders obtained by the solution precipitation method using a relatively short thermal treatment, compared to longersolid state reactions. All the Mn(IV) and half of the Mn (III) ions are present in octahedral sites, whereas the remaining Mn(III)ions are present in square-pyramidal sites. They form three-dimensional S-shaped tunnels, which allow sodium ions to be reversibly extracted/inserted and also small pentagonal tunnels containing non-extractable sodium ions [17]. Taking into account the structural aspects, the corresponding theoretical capacity is121 mAh/g.

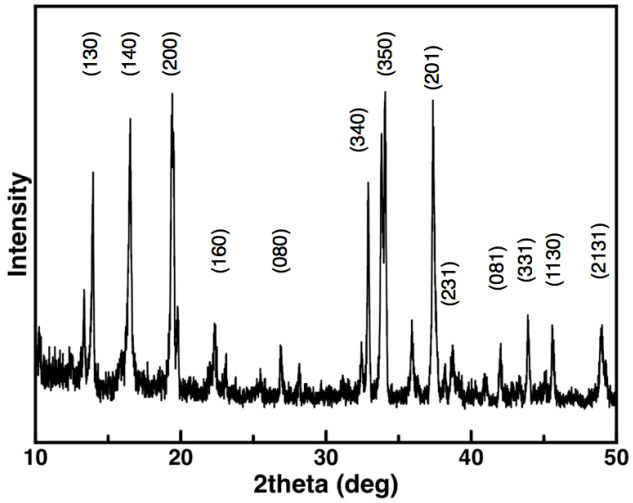

Figure 6.1 XRD pattern of the synthesized NMO particles.

The morphology of the synthesized NMO powder is shown in Figure 6.2. The use of a solution based preparation method allows toalso the control the powder morphology. These conditions lead to rod-shaped NMO micro particles with typical dimensions of a few µm in length, about 1µm in width and several hundred nm in thickness.

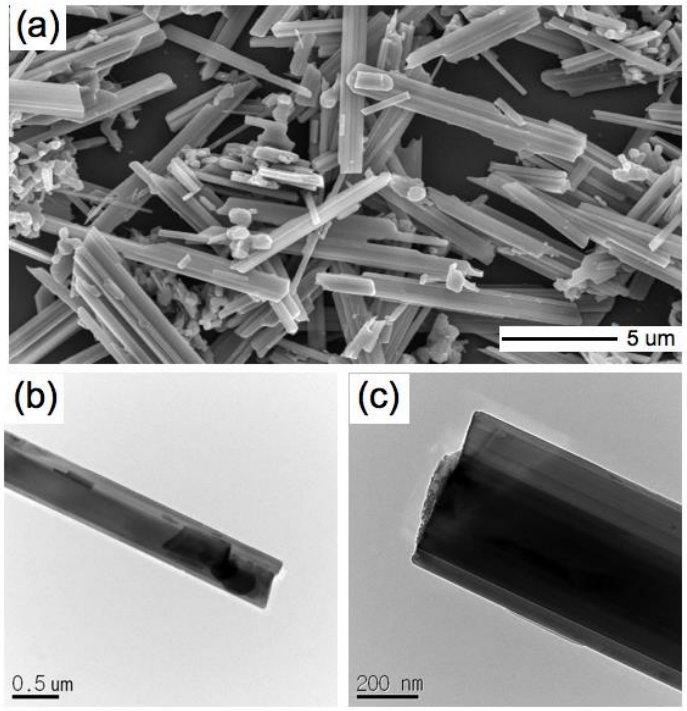

Figure 6.2 Microstructures of the synthesized NMO particles observed by (a) SEM and by (b), (c) TEM.

6.5 EIS data validation

In order to be sure that the measured impedance would be directly related to the NMO/electrolyte interface without parasitic contributes, the three electrode Swagelok cell arrangement was chosen and validated by using three different cell con-figurations, two of them with three electrodes and one with two electrodes. In the first arrangement, the impedances of the NMO/electrolyte interface (working electrode, WE) was measured vs. the Na/electrolyte interface (reference electrode, RE) and the other Na/electrolyte interface (counter electrode, CE) was used to collect the induced current. This configuration will be indicated as Z3el-WRin the following. In the second arrangement with three electrodes, the impedance between the two Na/electrolyte interfaces (RE and

CE) was measured using the NMO/electrolyte interface (WE) to collect the current, this configuration will be indicated as Z3el-CR. Finally, the impedance between the WE and the CE was measured without the use of a third electrode in a classical two electrodes measurement and it will be indicated asZ2el-WC. If the measurement is independent of the shape and position of the RE, the sum of the two three-electrode impedances(Z3el-WR+ Z3el-CR) has to be similar to the two-electrode configuration Z2el-WC[18–20].

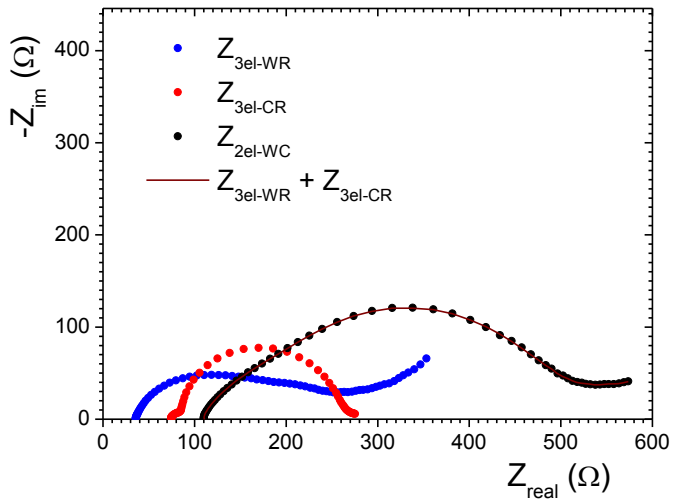

Figure 6.3 Nyquist plots of the different cell arrangements. $Z_{3el\text{-}WR}$: impedance measured between the NMO/electrolyte and the Na/electrolyte interfaces using the other Na/electrolyte as counter electrode, $Z_{3el\text{-}CR}$: impedance measured between the two Na/electrolyte interfaces using the NMO/electrolyte as counter electrode, $Z_{2el\text{-}WC}$: impedance measured between the NMO/electrolyte and the Na/electrolyte in the classical two electrodes arrangement, $Z_{3el\text{-}WR}+Z_{3el\text{-}CR}$: algebraic sum of the impedances obtained in the three electrodes configurations.

The impedance answers of all the three different configurations (Z3el-WR, Z3el-CR, and Z2el-WC) are reported in Figure 6.3 in terms of Nyquist plots. From the comparison it is clear that the impedance at the Na/electrolyte interfaces (Z3el-CR) is not negligible, so the two electrode measurements (Z2el-WC) cannot be used as representative of the working electrode impedance. Moreover, the Z3el-WR+ Z3el-CRsum differs from the Z2el-WCby less than 1% in the 1 × 104–1 × 10−2Hz frequency range pointing out the validity of the chosen configuration. Stable and reproducible spectra were obtained in Swagelock cells with different samples.

6.6 EIS measurement of first cycle

EIS measurements were used to monitor the electrode impedance change as a function of the first cycle depth of discharge(DOD) and of the second cycle state of charge (SOC). To change the electrode charge we used galvanostatic pulses (11 mA/g, C/25) in the potential range between 3.5 and 2.0 V, after a charging step at the same current rate. The first charge/discharge profile is reported in Figure 6.4 and shows a series of potential drops due to complex compositional behavior of the Na_xMnO_2 material. In fact, it was already pointed out that the electrochemical insertion/deinsertion of sodium in the phase does not proceed through a single solid solution mechanism, but through several multiphase reactions [8]. In particular, four main reactions are present in the investigated compositional range, corresponding to potential drops at 3.2, 2.9, 2.6,and 2.4 V. Below this last potential, the potential profile appears to be related to the intercalation of Na^+ only in a single phase domain.

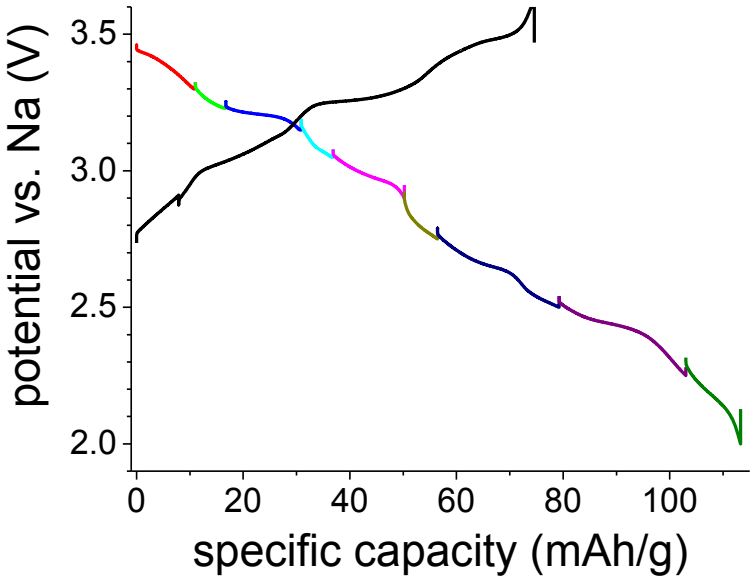

Figure 6.4 Charge (black) and discharge step profile at 11 mA/g.

Typical Nyquist plots obtained at different DOD and SOC are reported in Figure 6.5. At high frequencies (above 5 × 104Hz), the spectrum is dominated by the sum of the contributions of the external cell connections, the electronic conduction between the substrate and the active material, and the ionic conduction through the electrolyte. Since the highest experimental frequency is too low to see inductance distortions in the spectra, these contributions appear as a pure resistive behavior (Zimclose to 0) and are dominated by the ionic conductivity of the electrolyte, which can be determined by the high

frequency intercept of the real axis. No significant changes were observed in all the experiments. As the frequency decreases, a first arc appears in the spectrum followed by a second semi-circle and a portion of straight line at the lowest frequencies. In this frequency range, the impedance of lithium ion battery electrode is due to the complex electrochemical reactions taking place at the interfaces. This kind of answer can usually be attributed to three different reasons: the formation of a passive layer (often called Solid Electrolyte Interface, SEI) on the active particle surface, the charge transfer process coupled with the double layercapacitance and the solid state diffusion in the active particle. Several equivalent circuits can be used to describe the situation, from the simple Randles type circuit to more complex systems built by several sub-circuits. This ambiguous situation is also complicated by the fact that several equivalent circuits have the same mathematic representation. In any case, the impedance of lithium-ion battery electrodes is usually modeled by considering all the chemical–physical processes in series, each of them represented by a sub-circuit element [16].

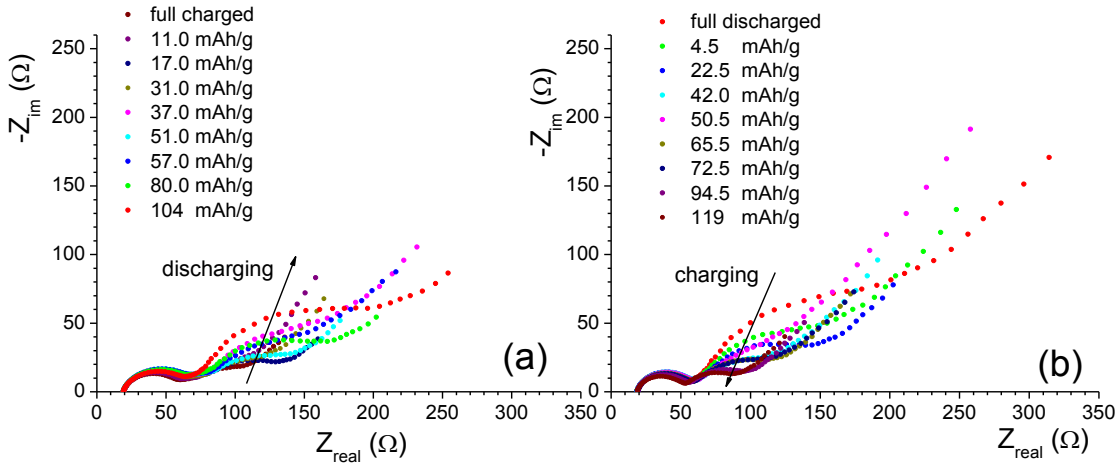

Figure 6.5 Nyquist plots of the NMO electrode at different DOD (a) and SOC (b).

In this case, the electric equivalent circuit (see onset of Fig. 6.6) was built by the combination of three elements: one serial resistance (Rser), one parallel RC circuit taking into account the sodium ionic conductivity in the SEI layer (RSEI,CSEI), and one Randels type circuit describing the charge trans-fer process (Rct), the double layer capacity (Cdl) and the diffusion element into the particles bulk (ZD). Due to the electrode roughness, the ideal capacitance elements have been replaced by the frequency depended Constant Phase Elements (CPE), whose frequency dependent parameter (ωn) is in all the

cases >0.75 (n = 1 for an ideal capacity). By the use of this equivalent circuit it was possible to fit the experimental spectra with reasonable agreement.

The change of both the SEI and the charge transfer resistances is reported in Figure 6.6 as a function of the DOD and the SOC. The presence of SEI layer on the surface of cathode materials for sodium ion batteries has been suggested recently [21], moreover a large irreversibility of the first cycle process in generally observed on oxides [6]. As it is possible to observe, the SEI resistance slightly changes with the electrode capacity, and it may be considered as constant during the material charge and discharge; the particle surface forms a stable layer, which does not change its electrical properties with the potential or the phase composition. Such observation is also confirmed by the capacitance value, which is constant (about 1 × 10−6F/cm2) for all the measurements.

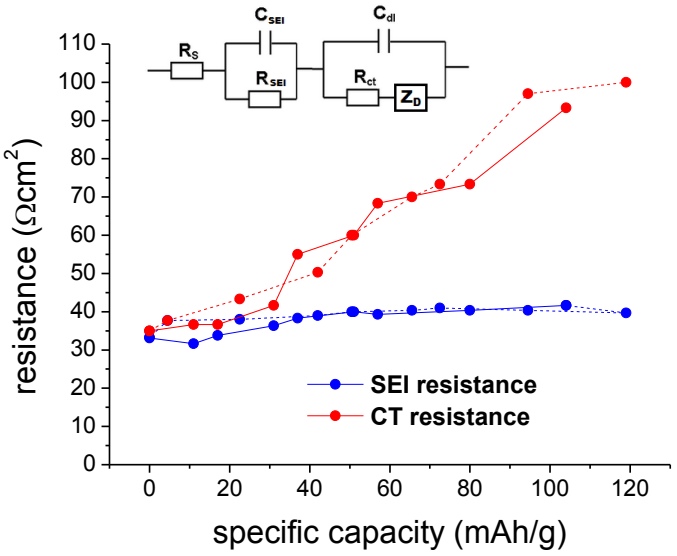

Figure 6.6 Charge transfer and SEI resistances as a function of the specific capacity.

On the contrary, the charge transfer resistance increases with the sodium amount in the phase. In particular, the major changes are in proximity of new phase formations, at potential between 2.9 and 2.6 V and below 2.4 V, where the resistance value becomes almost double the initial one. Since the structural differences among the phases are almost negligible [8], the increase of the charge transfer resistance during discharging may be attributed to the increased sodium amount in the phase. The double layer capacitances at the interface particle/SEI are in the range of 1 × 10−4F/cm2. At the lowest frequencies

(below 1 Hz), the contribution of the solid-state diffusion is present (ZD in the equivalent circuit of Fig. 6.6), i.e. Na ions moving into the bulk of active particle material.

In this case, the presence of the metallic current collector blocks the dif-fusion of ions at the inner interface (the stainless steel current collector does not alloy with Na). The diffusion process should be represented by the semi-infinite diffusion line, which corresponds to the tangent-hyperbolic function (T), widely discussed in the literature [22–24]. The representation of T in the Nyquist plot is usually a diffusive Warburg segment at 45°, followed by the vertical capacitive line at the lowest frequencies. However, the explored frequency range may not be enough to appreciate the whole element, and only the Warburg part of T can be seen in all the spectra as in the case of Fig. 6.5, where the lowest frequency limit (1 × 10−2Hz)is too high to see the capacitive limit. These spectra can be successfully fitted by using the Warburg element as diffusive element(ZD= W). To confirm the presence of the semi-infinite diffusion line, we have also obtained one spectrum (at DOD = 104 mAh/g) until1 × 10−4Hz (Fig. 6.7).

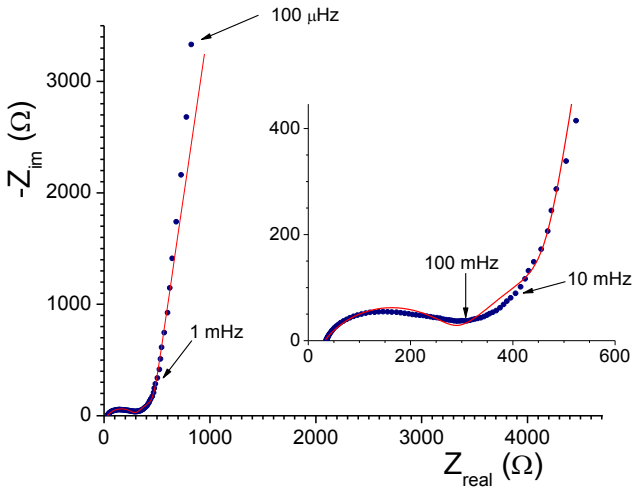

Figure 6.7. Nyquist plot at 104 mAh/g in the frequency range $1x10^{5}$-$1x10^{-4}$ Hz.

In this case, the measurement requires several hours and the external cell conditions have to be carefully con-trolled (constant temperature). As expected, at a frequency below1 × 10−2Hz the straight line bends out toward a vertical line, even if the limiting capacity behavior does not ever appear. For this reason, the spectrum was modeled by the usual equivalent circuit in which the Modified Restricted Diffusion Element was used as ZD. This element is very similar to the T, but includes a dispersion parameter to take into account a more complex frequency dependence, as in the case of the difference between

the ideal capacitance and the CPE [25]. The result of the fit is reported in Fig. 6.7 as a red line and, in this case, the resistance associated with the diffusion process is around 500, while those of SEI layer and charge transfer resistance are120 and 170, respectively.

The sodium ion solid-state diffusion process can be better characterized if the diffusion coefficient (DNa^+) is calculated. Due to the hard experimental conditions to obtain stable and reproducible low frequency data and the complex modeling, we have calculated the sodium ion diffusion coefficient using the Warburg elements obtained from the spectra in Fig. 6.5. In fact, Ho et al. [23] demonstrated that the Warburg impedance arising from the chemical diffusion in solid state is expressed by the following equations:

$$Zw = ZD\omega 1/2ZD = Vm(dE/dx)/(zFD1/2A)$$

Where ZD is the pre-exponential factor of the Warburg impedance, ω is the a.c. frequency, Vm is the molar volume, F is the Faraday constant, A is the electrode area, and (dE/dx) is the slope of equilibrium electrode potential vs. composition. The ZD expression canbe used to calculate D once all the other parameters are known [26,27]. In the present case, Vm= 22.85 cm3/mol, A = 2.45 m2/g as determined using BET method, ZD is obtained from EIS data in the frequency range above $1 \times 10{-}2$Hz, and (dE/dx) was measured at the end of each charging/discharging step after waiting for equilibrium conditions. The reported D is thus the average value in the corresponding composition range. Moreover, diffusion coefficients were calculated based on the assumption that the whole surface area of the active material is wet by the electrolyte in spite of the presence of binder and carbon additive materials. Also, the molar volume of the active material is assumed to be constant through-out the intercalation/extraction process despite the changes in the Na ion composition within the active material during these processes. Hence, the diffusion coefficient values presented in this work are apparent values whose relative errors have been estimated as ±10%. The obtained D Na^+ values are reported in Figure 6.8 and they change with the voltage/composition of the electrode.

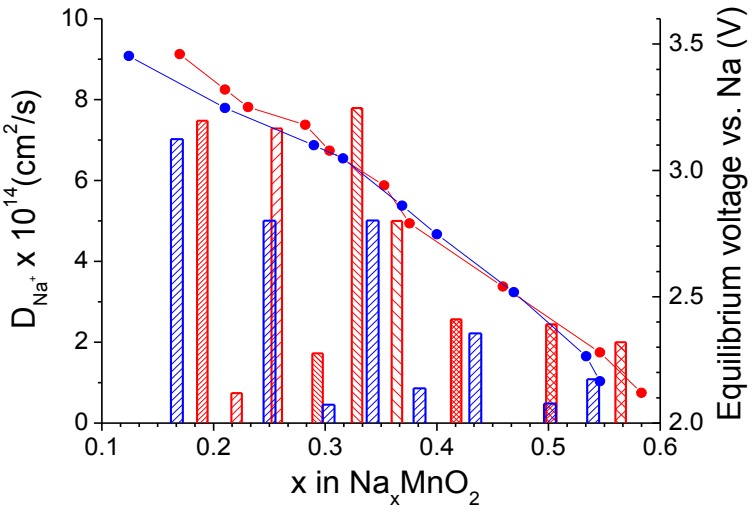

Figure 6.8. Average sodium diffusion coefficients during discharge (red bars) and charge (blue bar) as a function of the Na^+ composition. Equilibrium potentials are also reported on the right axis.

Good agreement has been observed for the charge and discharge pro-cess. In particular, the composition range can be divided into two domains for x higher or lower than 0.35 in NaxMnO2. The highest values for the diffusion coefficient are in the sodium poor composition range (x < 0.35), where DNa+ shows also sudden drops of one order of magnitude during phase transformations (0.21 < x < 0.23and 0.28 < x < 0.30). On the contrary, the sodium rich portion of the graph is characterized by lower DNa^+ values, which decrease with the increase of the sodium amount. Thus, both the structural rearrangements and the sodium composition control the diffusion kinetic in the phase.

6.7 Evolution of impedance with temperature

To better identify the different processes involved, impedance measurements were also performed in the temperature range10–70◦C. Two points of the potential/capacity profile were explored at equilibrium values of 3.20 V (corresponding to67 mAh/g) and 2.43 V (93 mAh/g) to get activation energies at both low and high sodium concentration, respectively. Fig. 9 reports the spectra evolution as a function of the temperature at the two potentials.

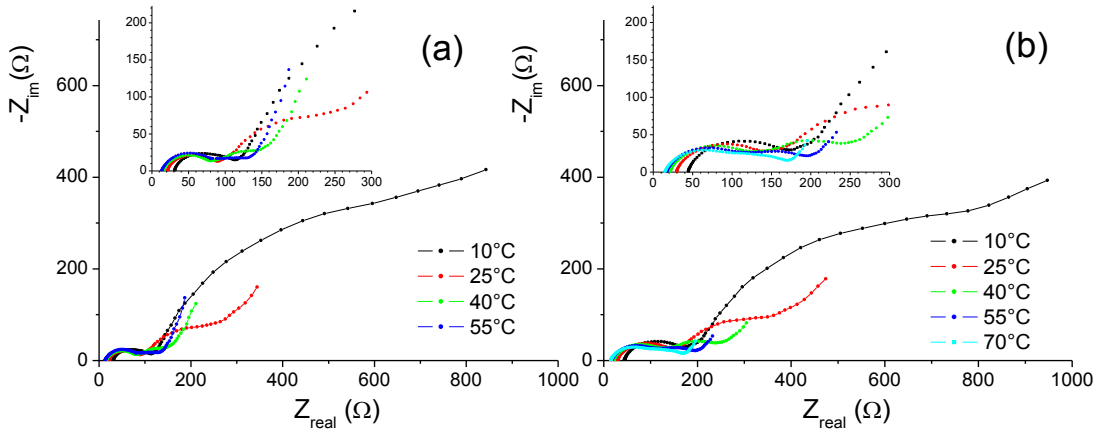

Figure 6.9. Nyquist plots at different temperature measured at equilibrium potential of 3.20 V (a) and 2.43 V (b).

The Arrhenius plots corresponding to the different kind of processes (Fig. 6.10) were calculated from the resistances and the Warburg element of the electrical circuit reported in Fig. 6. In particular, the exchange current density (i0) of the electrochemical reaction was calculated from the charge transfer resistance and the BET surface area.

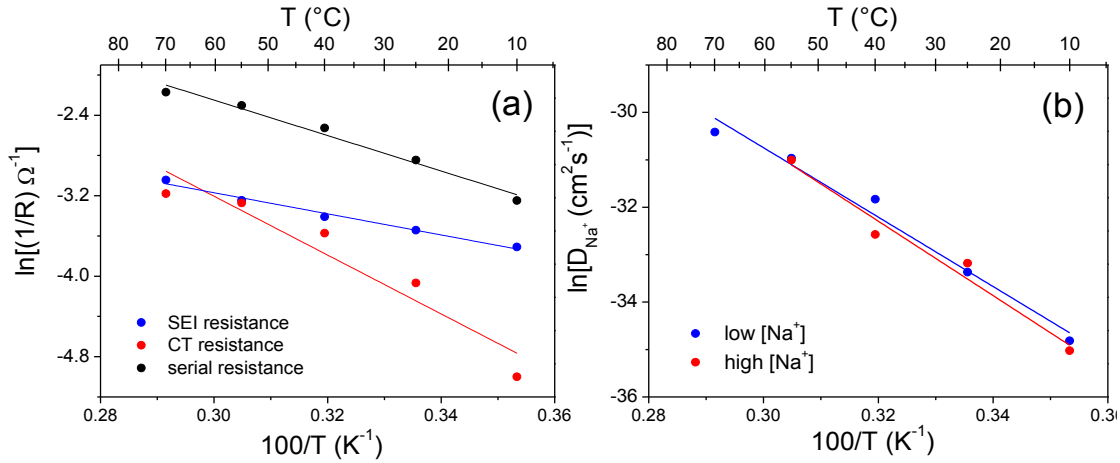

Figure 6.10 Arrhenius plots obtained from the serial, the charge transfer (CT) and the SEI resistance at 2.43 V (a) and for the diffusion process (b)

The i0values range from 1 to 10 A/cm2atlow and high temperature, respectively, with activation energies of 0.28 ± 0.04 eV (low [Na+]) 0.30 ± 0.07 eV (high [Na+], Fig. 10a).These values are slightly higher than the corresponding activation energies in lithium metal oxides [28] and are comparable to those of lithium metal phosphate [29]. The resistances attributed to the SEI process show a slight steep slope and low activation energies (0.09 ± 0.01 eV and 0.05 ± 0.005 eV at low and high [Na+], respectively, see

Fig. 10b). To our knowledge do not exist other data to compare with, however this behavior may be attribute to diffusion in the polymeric film formed on the particle surface. The ionic conductivity of the electrolyte) was obtained from the serial resistance. The values at 25◦C (around 6 mS/cm) are in very good agreement with that reported from Ponrouch et al. [30] and the activation energies are also independent on the DOD (0.17 ± 0.2 eV)and in agreement with that of the ionic conductivity of similar lithium ion electrolytes [31]. Thus, the serial resistance is mainly related to the ionic conductivity of the electrolyte. Finally, the activation energy for the diffusion process in NMO has the same value(0.63 ± 0.05 eV) at the two sodium ion concentration and it is similar to those reported by Kim et al. [3] for diffusion barrier in sodium metal oxides.

6.8 Cycling properties

Figure 6.11 shows the cycling behavior of NMO. The results of the impedance analysis clearly show that at elevated DOD or low SOC the charge transfer resistance increases, while at the same time the diffusion coefficient decreases. Both these aspects contribute to slowing down the kinetic of the electrode reaction and may affect the electrode behavior upon cycling. To better clarify this aspect, we have cycled the NMO electrode for 30 times at low current (11 mA/g) between 2.0 and 3.5 V and measured the electrode impedance at the end of some selected cycles (1, 2, 5, 10, 20, and 30). At this rate, the NMO electrode was initially able to supply most of the expected capacity value (121 mAh/g) considering all the mobile Na^+ ions; then the charge decreases upon cycling and stabilizes after 20 cycles at 105 mAh/g (see Fig. 6.11).

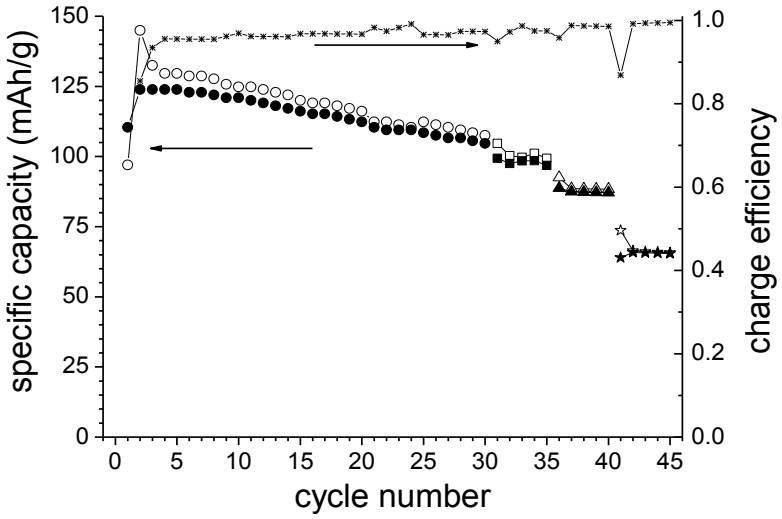

Figure 6.11 Charge (empty symbol) and discharge (full symbol) capacity and Coulomb efficiency of NMO electrode cycled at different current densities: 11.0 mA/g (circles), 27.5 mA/g (squares), 55 mA/g (triangles), and 275 mA/g (stars).

The corresponding Coulomb efficiency is in the range of 95/97%. This behavior can be better understood looking at the change in the surface resistance values vs. the number of the cycles. As reported in Figure 6.12, the SEI resistance is basically unchanged upon cycling, while the charge transfer resistance increases after 20 cycles at a value which is almost double that of the initial one.

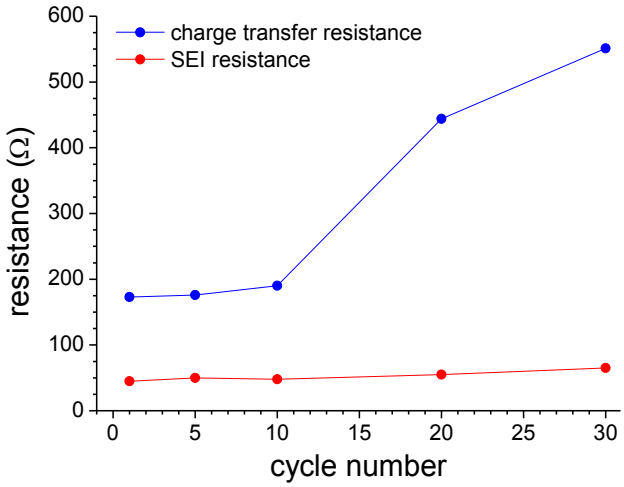

Figure 6.12 Evolution of the charge transfer and SEI resistances (end of discharge) with the cycling.

To understand the kinetic limits of the system, after the first 30 cycles at low current, we progressively increased the current every 5 cycles to27.5 mA/g, 55.0 mA/g, and 275 mA/g. At intermediate currents (27.5and 55.0 mA/g) the electrode is still able to supply a good discharge capacity (100 and 90 mAh/g, respectively), while at the highest ratea lower capacity value was observed (65 mAh/g) (Figs. 6.11 and 6.13). In the measurements performed at a higher rate the charge efficiency increases, indicating the presence of one side reaction during theanodic process: the less the time the system remains at oxidative potentials, the higher the efficiency.

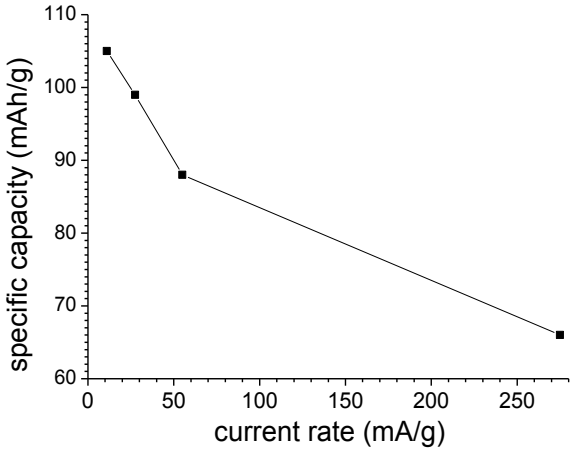

Figure 6.13 Specific discharge capacity as a function of the current rate.

References

[1] 1 J.M. Tarascon, Nature Chem., 10 (2010) 510

[2] O. Ebgue, Missouri University of Science and Technology. Study outlines supply chain challenges for lithium future. ScienceDaily. Retrieved October 24, 2012, from http://www.sciencedaily.com- /releases/2012/09/120921140112.htm

[3] S. Kim, X. Ma, S. Ping Ong, G. Ceder, Phys. Chem. Chem. Phys. 14 (2012) 15571

[4] S. Komaba, C. Takei, T. Nakayama, A. Ogata and N. Yabuuchi, Electrochem. Commun., 12(3) (2010) 355

[5] C. Delmas, J.-J. Braconnier, C. Fouassier and P. Hagenmuller, Solid State Ionics, 3 (1981) 165

[6] R. Berthelot, D. Carlier and C. Delmas, Nat. Mater., 10 (2011) 74

[7] M. D'Arienzo, R. Ruffo, R. Scotti, F. Morazzoni, C. M. Mari, Phys. Chem. Chem. Phys., 14 (2012) 5945

[8] F. Sauvage, L. Laffont, J.M. Tarascon, E. Baudrin, Inorg. Chem., 46 (2007) 3289.

[9] Y. Li, Y. Wu, Nano Res., 2 (2009) 54

[10] E. Hosono, H. Matsuda, I. Honma, S. Fujihara, M. Ichihara, H. Zhou, J. Power Sources, 182 (2008) 349

[11] M.M. Doeff, T.J. Richardson, J. Hollingsworth, C.-W. Yuan, M. Gonzales, J. Power Sources, 112 (2002) 294

[12] Y. Cao, L. Xiao, W. Wang, D. Choi, Z. Nie, J. Yu, L.V. Saraf, Z. Yang, J. Liu, Adv. Mater., 23 (2011) 3155

[13] N. Yabuuchi, M. Kajiyama, J. Iwatate, H. Nishikawa, S. Hitomi, R. Okuyama, R. Usui, Y. Yamada, S. Komaba, Nat.ure Materials, 11 (2012) 512

[14] H. Kim, D.J. Kim, D.-H. Seo, M.S. Yeom, K. Kang, D.K. Kim, Y. Jung, Chem. Mater., 24 (2012) 1205

[15] E. Barsoukov. In Impedance Spectroscopy: Theory, Experiment, and Applications; Barsoukov, E., Macdonald, J. R., Eds.; John Wiley and Sons, Inc.: Hoboken, NJ, 2005; pp 444-457 and 462

[16] I. Kruk, P. Zajdel, W. van Beek, I. Bakaimi, A. Lappas, C. Stock, M.A. Green, J. Am. Chem. Soc., 133 (2011) 13950

[17] S. Leroy, F. Blanchard, R. Dedryvere, H. Martinez, B. Carre, B, D. Lemordant, D. Gonbeau, Surf. Interface Anal. 37 (2005) 773

[18] E. Barsoukov, J.H. Kim, C.O. Yoon, H. Lee, Solid State Ionics 116 (1999) 249

[19] R. Ruffo, S. S. Hong, C. K. Chan, R. A. Huggins, Y. Cui, J. Phys. Chem. C 113 (2009) 11390

[20] K-H. Ha, S. H. Woo, D. Mok, N.-S. Choi, Y. Park, S. M. Oh, Y. Kim, J. Kim, J. Lee, L. F. Nazar, K. T. Lee, Adv. Energy Mat. (2013) DOI: 10.1002/aenm.201200825

[21] M. Dollé, F. Orsini, A.S. Gozdz, J.M. Tarascon, J. Electrochem. Soc. 148(8) (2001) A851.

[22] C. Ho, I.D. Raistrick, R.A. Huggins, J. Electrochem. Soc. 127(2) (1980) 343–350.

[23] C.J. Wen, C. Ho, B.A. Boukamp, I.D. Raistrick, W. Weppner, R.A. Huggins, Int. Mater. Rev. 5 (1980) 253

[24] Handbook of Electrochemical Impedance Spectroscopy, http://www.bio-logic.info/potentiostat/notesheis.html

[25] O. Yamada, M. Ishikawa, M. Morita, Electrochim. Acta, 45 (2000) 2197

[26] K.M. Shaju, G.V. Subba Rao, B.V.R. Chowdari, Electrochim. Acta, 48 (2003) 2691

[27] R. Ruffo, F. La Mantia, C. Wessells, R. A. Huggins, Y. Cui, Solid State Ionics, 192(1) (2011), 289-292

[28] C.M. Julien, Mat. Sci. & Eng., R40 (2003) 47-102

[29] M. Takahashi, S. Tobishima, K. Takei, Y. Sakurai, Solid State Ionics 148 (2002) 283–289

CHAPTER 7

Conclusion

The work was devoted to the improvement of rechargeable alkaline batteries. Two different strategies were applied: i) the investigation of new electrode materials to increase the electrode performances, and ii) the studies on failure mechanism of commercial rechargeable batteries in order to change the battery structure or chemistry to overcome the issue and increase the calendar/cycle life. Both lithium and sodium systems were explored. In the former case, carbon based materials were investigated as high energy anodes (chapter 2), while the cell failure of commercial batteries (chapter 3) and $Li[Ni_{1/3}Mn_{1/3}Co_{1/3}]O_2$/graphite cells (chapter 4) were investigated by Ultra High Precision Coulometry (UHPC) and dQ/dV analysis. Moreover, sodium ion systems were also considered as promising alternative to solve the issue of lithium raw materials depletion and new compounds for anode and cathode application were investigated. Thick films of Sn, were structural and electrochemical characterized as negative electrode (chapter 5), while the promising $Na_{0.44}MnO_2$ cathode material was deeply investigated by advanced electrochemical techniques (chapter 6). A brief conclusion of the aforementioned chapters is here reported.

Carbon prepared by magnetron sputtering at low pressure has a density near 1.9 g/cm^3, virtually no impurities, a reversible specific capacity near 800 mAh/g and an irreversible capacity near 200 mAh/g. However, the average delithiation potential is near 1.0 V and the materials require sputtering for their creation, which will probably limit the usefulness of these materials. Upon heating to 900^{o}C, the average potential drops to about 0.75V, the reversible capacity shrinks to about 600 mAh/g and the irreversible capacity drops to about 100 mAh/g. If an economical synthesis could be found to duplicate the low-pressure sputtered carbons, then they might be worth a look in practical Li-ion cells. Synthesis techniques like high energy ball milling have been tried over the years [9], and such techniques yield materials similar to the high pressure sputtered carbons upon exposure to air. Sputtered carbon prepared at high pressure is porous and hence forms surface functional groups upon air exposure. These surface functional groups impact the voltage-capacity profile and cause charge-discharge hysteresis and a higher average delithiation potential (near 1.5V). Such materials have no utility in Li-ion batteries.The long term cycling of the low-pressure sputtered carbons has not been studied in this work. This is because the adhesion of the films to the copper foil was not excellent and the carbon films were easily detached from the copper foil when cells were opened. Long term cycling experiments would be better carried out on proper electrodes containing

binder and, perhaps, conducting diluent. This would require more material than can be conveniently prepared in our sputtering system. Finally, carbon surprises once again. Low-pressure sputtered carbon has a unique voltage-specific capacity behavior that needs to better understood with further experiments and with ab-initio theory. It appears to form a fourth class of carbonaceous materials that reversibly react with lithium to be added to the three classes described in reference 8 of chapter 2.

The study of Chapter 3 confirmed once again that high precision coulometry measurements, electrochemical impedance spectroscopy and differential voltage analysis are very powerful techniques to learn about parasitic reactions in Li-ion cells. A unique set of LCO/graphite cells having identical chemistry and ages from 0.3 to 12 years was studied using these methods. The capacity loss in the LCO/graphite cells studied here is not caused by loss of active material through electrical disconnect. By contrast, all capacity loss can be explained by loss of active lithium to the negative electrode SEI. With ageing, the loss of lithium to the SEI continually reduces, leading to more consistent performance with ageing; this is a highly favorable trend for a long-life application. However, electrolyte oxidation still occurs in these cells at a low but measurable rate. The aging of these LCO/graphite cells is strongly dependent on the upper cut-off voltage as well as the cycling conditions. The cells in groups G_1 to G_5, which show decade-long life time, were made 12 years ago, before some modern electrolyte additives have come available. One reason their lifetime is so long is that the upper cut-off potential was only 4.075 V. Researchers and manufacturers targeting cells for decades-long lifetime should always recognize the impressive lifetime gains that can be had by limiting the upper cut-off potential. For those that want **both** higher energy and longer lifetime it is essential to improve electrolyte performance at high voltage in order to achieve longer battery lifetime. This requires more studies on electrolyte additives which can decrease electrolyte oxidation and therefore charge endpoint capacity slippage. Given that most of the battery community does not have equipment that can reliably measure charge endpoint capacity slippage, this represents a major issue.

Main aim of chapter 4 was to probe conditions that may accelerate active material loss through particle fracturing. Therefore eight pouch cells discharged at different rates were studied by dV/dQ analysis, EIS measurement, and SEM images. dV/dQ analysis confirms that capacity loss due to the mass loss is negligible, and fade of high discharge rate is mainly due to the consuming lithium atoms in negative SEI layer. According to EIS

measurements, it is clear that negative electrode slippage is decreasing with cycling and C-rate. SEM images also confirm the dVdQ results and EIS measurement since some holes and cracks have been seen in both 0.5C and 4C pouch cells. Cracks are noticeably bigger and more in 4C pouch cell with respect to 0.5C pouch cell. This suggest that by high-rate de-intercalation of lithium at graphite, SEI layer and most likely graphite particles get damage and expose new surface are to the electrolyte, which decrease the impedance and increase the slippage due to the consumed lithium in making new SEI. According to this study, electrolyte additives, which make SEI layer more stable could increase the lifetime of these types of cells, that experience high rate cycling, and also decrease their capacity loss during their operating life time.

In addition to studies related to Li-ion batteries, it is very critical to investigate electrode materials for Na-ion batteries which potentially is very promising alternative for Li-ion batteries. Therefore we dedicate chapter 5 and 6 to studies related to Na-ion batteries.

For the negative electrode, we explored the possibility to use tetragonal tin layer, obtained by very cheap method, as electrode in Na_ion rechargeable batteries. The films show very good crystallinity after deposition without any further heat treatments. Alloing/dealloying voltage profiles show similar behavior to that previously reported: Four different bi-phasic regions in the voltage range between 0.01 V and 1.00 V. At low current rates, the specific capacities are in good agreement with the theoretical value of 847 mAh/g, but their values drop after 4 cycles, probably due to active material fading. At current rate of 170 mA/g (C/5), the specific capacity decreases to 551 mAh/g, but remain more stable for at least 10 cycles. As for similar alloying/dealloing processes (Si-Li System), metal nanostructure thick film could be used to improve cyclability. Unfortunately this material shows poor cycleability and it need to be improved in order to meet industrial requirements and be practically useful.

In addition to negative electrode we studies $Na_{0.44}MnO_2$ (NMO) as a promising cathode for Na-ion batteries. The NMO phase prepared by the modified Pechini method exhibits a discharge capacity of about 110 mAh/g at low cur-rent rate (11 mA/g), which decreases to 65 mAh/g at high rate(275 mA/g). From the electrochemical impedance analysis (EIS),an elegant method to analyze the kinetic behavior of electrode materials, it is clear that both the surface resistance and the ion diffusion in the solid phase play a role in limiting the material performances, while the contribute of the electrolyte conductivity is

negligible. EIS measurements performed at different temperatures allowed the determination of the activation energies whose values confirmed the interpretation of the various processes. There are two chemical/physics processes, which contribute to the overall surface resistance: the well known charge transfer resistance and the presence of a passive layer (SEI) on the particle surface. Only the former (charge transfer resistance) depends on both the electrode charge state and the cycling process, while the latter (SEI contribute) remains almost the same. In the end it is necessary to emphasize that only the measurements carried out at a very low frequency are able to display the tangent-hyperbolic behavior of the semi-infinite diffusion impedance, which is characterized by a resistance value (500), similar to those observed for the electrode surface (300).

Publications list

1. **R. Fathi,** J.C. Burns, D.A. Stevens, Hui Ye, Chao Hu, Gaurav Jain, Erik Scott, Craig Schmidt, and J.R. Dahn *"Ultra High-Precision Studies of the Degradation Mechanisms in Aged $LiCoO_2$/Graphite Li-Ion Cells"* J. Electrochem. Soc., 161, A1572-A1579 (2014).
2. D.Stevens, R.Y.Ying, **R.Fathi**, J.N. Reimers, J.Harlow, and J.R. Dahn. "*Using High Precision Coulometry Measurements to Compare the Degradation Mechanisms of NMC/LMO and NMC-Only Automotive Scale Pouch Cells*"J. Electrochem. Soc., 161 (9) A1364-A1370 (2014).
3. **R.Fathi**, R. Sanderson, L.Lucas, and J.R. Dahn. "*The electrochemical reaction of lithium with high-capacity dense sputtered carbon*."Carbon, 74 , 249 (2014).
4. **R.Fathi**, R. Ruffo, C.M. Mari, "*Electrochemical Behavior of Electrodeposited Sn Films: Possible Negative Electrode for Na Rechargeable Batteries*" J. Chem. Chem. Eng. 8, 358 (2014).
5. R.Ruffo, **R. Fathi**, D.J. Kim, Y.H. Jung, C. Mari, D.K.Kim "*Impedance analysis of $Na_{0.44}MnO_2$ positive electrode for reversible sodium batteries in organic electrolyte"*Electrochem. Acta, 108, 575 (2013) .
6. D.J.Kim, R.Ponraj, A. Kannan, H.Lee, **R.Fathi**, R.Ruffo, C.Mari, and DK. Kim." *Diffusion behaviour of Sodium ions in Na 0.44 MnO2 in aqueous and non-aqueous electrolytes*". J. power sources. 244, 758 (2013).